Modifications to Furniture Fire Model for HAZARD System

Mark A. Dietenberger

Modifications to Furniture Fire Model for HAZARD System

Mark A. Dietenberger
University of Dayton
Dayton, OH 45469

Notice

This report was prepared for the Building and Fire
Research Laboratory of the National Institute of
Standards and Technology under grant Number 60NANB0D1051.
The statements and conclusions contained in this report
are those of the authors and do not necessarily reflect
the views of the National Institute of Standards and
Technology or the Building and Fire Research Laboratory.

UDR-TR-91-126

MODIFICATIONS TO FURNITURE FIRE MODEL FOR HAZARD SYSTEM

Mark A. Dietenberger

University of Dayton
Research Institute
Dayton, OH 45469

OCTOBER 1991

Final Report For Fiscal Year 1990-91
Grant No. 60NANBOD1051

Center for Fire Research
National Institute of Standards and Technology
Gaithersburg, Maryland

Table of Contents

List of Illustrations

List of Illustrations (Continued)

List of Illustrations (Continued)

List of Illustrations (Concluded)

List of Tables

Foreword

This final technical report describes the work accomplished during the period from 30 July 1990 through 31 July 1991 by the University of Dayton Research Institute (UDRI) under Grant No. 60NANBOD1051 for the National Institute of Standards and Technology. Dr. Walter Jones of the Fire Hazard Analysis Group, Center for Fire Research was the technical monitor.

The efforts reported here were performed by the principal investigator, Mark A. Dietenberger, who is a full-time member of the Structural Integrity Division of UDRI. Dr. A. M. Rajendran, head of the Analysis and Computation Group, provided project direction, and Dr. Joseph P. Gallagher, head of the Structural Integrity Division, served as the program manager.

Section 1

Introduction

Modifications to the furniture fire model (FFM) for inclusion in the HAZARD system required three major tasks: (1) comparison of the FAST/FFM predictions with several full-scale burns measured in the furniture calorimeter, (2) development of an algorithm for personal computers to calibrate ignition and flame spread parameter, and (3) conversion of FFM to a Flame Spread Model (FSM) for a single panel. The code was implemented on the PC for use with CFAST. The application problems are compartmentation, structural fire resistance, ignitibility of a secondary combustible item, and room flashover.

Section 2

Predictions of Furniture Calorimeter Tests for Upholstered Mockups

The FAST/FFM (Version 3) predictions were compared with data from full-scale fire tests listed in NBS Monograph 173, "Fire Behavior of Upholstered Furniture," by Babrauskas and Krasny. The full-scale database contained the furniture calorimeter measurements of heat and mass release rates, the soot extinction areas versus time, and the VCR recordings of flame spreading on each cushion panel versus time. The corresponding bench-scale database from the cone calorimeter and the flame spread apparatus at various irradiance levels of very similar materials was available. These existing bench-scale and full-scale fire databases were acquired and tabulated. In particular, six different fabric/foam combinations were chosen, and the model scaling constants were calibrated for each one.

The scaling constants associated with the heat and mass release rates were calibrated on similar materials tested with three or four different values of the cone heater radiances. This calibration was a two step procedure. The first step was to calibrate a constant surface heat flux, which adjusts the calculated net surface heat flux. This adjustment enables one to rescale the heat and mass release data from the cone calorimeter for different radiances onto a single curve as a function of burn history. Further details are given in the "Technical Reference and User's Guide for FAST/FFM," [Ref. 1]. The second step was to adjust the burn history parameters. This adjustment allows conversion from a 50 mm thick foam used in the cone calorimeter to a 100 mm thick foam used in the upholstered furniture.

The soot parameters of maximum absorption coefficient and specific extinction area corresponded to the polyurethane foam. Using the conventional approach, the surface ignition temperature and the thermal thickness were derived from the piloted time to ignition data versus irradiance. In all furniture fire tests, since the piloted ignition was located on the seat middle and 100 mm from the back rest, the constant for the flame spread rate was calibrated to obtain agreement with the observed burn area fraction of the seat during early growth. When these data

were not available, the flame spreading constant was calibrated to match the timing of the rapid rise in the heat release rate.

The excellent comparisons of the cushions burn area fraction between FFM and the data demonstrate the model's ability to accelerate the flame spread rate as a result of the fire's rising thermal radiation. The heat release rate predictions for five different furniture geometries for a given cushion type compared well with the data; thus, demonstrated the capability for fire scaling. The results also demonstrated that, due to the increased plume radiation, the rapid flame spread up the back rest accentuates the flame spreading on the seat. Shortly after the rapid flame spreading, the peak heat release rate shows its dependence on the total burning area as well as on the magnitude of the thermal radiative heat fluxes from the fire plume. Further results are reported in the journal article submitted to the Fire Safety Journal (see Appendix A).

Section 3

Calibration of the Scaling Constants on a Personal Computer

The LIFTFIT code was developed to assist in calibrating the ignition and flame spread constants using a personal computer. The calibration of the ignition and flame spread parameters in opposed flow involve: (1) a scheme to determine material constants, such as ignition temperature, thermal inertia, and thermal thickness from the piloted ignition measurements, and (2) a scheme to obtain the flame spread constants from the LIFT and from a horizontal flame spread apparatus. It is assumed that these apparatus are designed such that there is negligible thermal radiation from the fire plume to the flame front. This design allows a direct evaluation of the flame spread constants without the indirect use of FFM. As a result, the algebraic formulations of ignition and flame spread rate could be used in the curve-fitting algorithms developed and coded for use on the PC.

In order to understand the effects of the flame spread directions on the flame spread constants, it was necessary to extend the classical deRis formulae to account for the effects of surface thermal radiation, changing gas properties, the Damkohler's number, and the buoyant air flow. The algorithms for these types of flame spread predictions were developed for Dietenberger's Ph.D. Thesis [Ref. B-10]. The model constants were calibrated to predict the published flame spread data for the paper/card and thick PMMA in various environments. The flame spreading algorithm developed for the thesis work was incorporated into LIFTFIT to correspond with the data for the PMMA tested on the LIFT and on a horizontal flame spread apparatus. The two model constants recalibrated were the oxygen-to-fuel ratio and the coefficient of buoyant velocity. For a given environmental condition, the flame temperature and buoyant velocity are calculated, which are, in turn, used to calculate the flame front heat flux and the flame thermal length. The conclusion was that the model constants do not change with the flame spread directions in opposed flow. Further results are given in detail in the second journal article submitted to the Fire Safety Journal (see Appendix B).

UDRI has developed a preliminary computer program to calibrate the scaling constants for the heat and mass release rate data from the cone calorimeter for use on the PC. This procedure involved converting the FFMDAT subroutine to a PC based program for generating the scaled FFM data. For post-processing the data, we used the commercial graphic package program, GRAPHER, to create the figures. Manual calibration of scaling constants was achieved by modifying the values of the constants until the data points in the figures collapsed to a single curve. As an exercise, Figures 3-6 in the "Technical Reference and User's Guide for FAST/FFM Version 3," were redrawn. These figures are shown in Appendix C.

Section 4

Development of the Flame Spread Model (FSM)

The FFM was simplified and made user friendly by downsizing to a Flame Spread Model (FSM) for a single panel. The computer memory requirements were significantly reduced, and the inputs to FSM were documented thoroughly. The several simulations of a wall fire spread have revealed certain anomalies, which were corrected by improving the flame spread logic and by restricting the panel geometry to avoid large errors in the view factor evaluations. The results with FSM are described in more detail in an upcoming NIST technical report.

Section 5

Summary

The successful completion of Task One, comparison of FFM to several furniture calorimeter tests, is summarized in Appendix A. Task Two, development and verification of the LIFTFIT program, did not follow the original plan due to difficulties in automating the calibration of the ignition and flame spread constants. However, these difficulties have been resolved by incorporating a generalized routine for the flame spread rate, which involved superior model constants based on variation of environmental conditions. Task Three, the development of FSM, was brought to a successful conclusion and will be published as a separate NIST report.

Section 6

References

1.   Dietenberger, M.A."Technical Reference and User's Guide For FAST/FFM Version 3," NIST-GCR-91-589, 1991.

A-1.   Bukowski, R.W., "Evaluation of Furniture-Fire Hazard Using a Hazard Assessment Computer Model," *Fire and Materials*, **9**, 4 (1985), pp. 159-166.

A-2.   Dietenberger, M.A., "Technical Reference and User's Guide for FAST/FFM (Version 3)," NIST-GCR-91-589, 1991.

A-3.   Dietenberger, M.A., "Chapter 14, Upholstered Furniture: Detailed Model," *Heat Release in Fires*, Elsevier Science, London, 1991.

A-4.   Jones,W.W. and Peacock, R.D., "Technical Reference Guide for FAST Version 18," NIST-TN-1262, May 1989.

A-5.   Atreya, A., "Pyrolysis, Ignition, and Fire Spread on Horizontal Surfaces of Wood," Ph.D. Thesis, Harvard University, Cambridge, MA, 1983.

A-6.   Delichatsios, M.M., Mathews, M.K., and Delichatsios, M.A., "Upward Fire Spread Simulation Code: Version I - Noncharring Fuels," FMRC J.I. OROJ2.BU, November 1990.

A-7.   Mitler, H.E., "Predicting the Spread Rates of Fires on Vertical Surfaces," Presented at the 23rd Int. Sym. on Combustion, Orleans, France, July 1990.

A-8.   Kim, C.I. and Kulkarni, A.K., "Upward Flame Spread Simulation," Submitted to Fire Safety Science, 1990.

A-9.   Smith, E.E. and Satija, S., "Release Rate Model for Developing Fires," *Trans. ASME J. of Heat Transfer*, **105** (1983), pp. 281-287.

A-10.   Blomqvist, J. and Andersson, B., "Modelling of Furniture Experiments with Zone Models," *Fire and Materials*, **9**, 2 (1985), pp. 81-87.

A-11. Dietenberger, M.A., "Mathematical Modeling of Furniture Fires," NBS-GCR-86-506, February 1986.

A-12. Ray, S.R., Fernandez-Pello, A.C., and Glassman, I., "A Study of the Heat Transfer Mechanisms in Horizontal Flame Propagation," *Trans. ASME J. of Heat Transfer*, **102** (1980), pp. 357-363.

A-13. Quintiere, J., "A Simplified Theory for Generalizing Results from a Radiant Panel Rate of Flame Spread Apparatus," *Fire and Materials*, **5**, 2 (1981), pp. 52-60.

A-14. Atreya, A., Carpentier, C., and Harkleroad, M., "Effect of Sample Orientation on Piloted Ignition and Flame Spread," *Fire Safety Science - Proceedings of the 1st Int. Sym.*, Eds. C. Grant and P. Pagni, (Hemisphere, Washington), pp. 97-109.

A-15. Dietenberger, M.A., "First and Second Quarterly Reports," prepared for NBS Grant #60NANB5D0556 for FY 86-87.

A-16. Dietenberger, M.A., "A Validated Furniture Fire Model with FAST," NIST-GCR-89-564, 1989.

A-17. Krasny, J.F. and Babrauskas, V., "Burning Behavior of Upholstered Furniture Mockups," *Journal of Fire Sciences*, **2** (1984), pp. 205-235.

A-18. Babrauskas, V. and Krasny, J.F., "Fire Behavior of Upholstered Furniture," NBS Monograph 173, November 1985.

A-19. Babrauskas, V., "Bench-Scale Methods for Prediction of Full-Scale Fire Behavior of Furnishing and Wall Linings," SFPE-TR-84-10, 1984.

A-20. Dietenberger, M.A., "Formulae to Predict Piloted Ignition and Flame Spread on Composite Solid Fuels in Extreme Environments and Their Validation with Experiments," Ph.D. Thesis in Mechanical Engineering, University of Dayton, 1991.

A-21. Bard, S. and Pagni, P.M., "Spatial Variation of Soot Volume Fractions in Pool Fire Diffusion Flames," *Fire Safety Science - Proceedings of the 1st Int. Sym.*, Eds. C. Grant and P. Pagni, (Hemisphere, Washington), pp. 361-369.

B-1. deRis, J. N., "Spread of a Laminar Diffusion Flame," 12th Int. Sym. on Combustion, The Combustion Institute, 1969, pp. 241-252.

B-2. Fernandez-Pello, A.C., Ray, S.R., and Glassman, I., "Flame Spread in an Opposed Flow: The Effect of Ambient Oxygen Concentration," 18th Int. Sym. on Combustion, The Combustion Institute, 1981, pp. 579-589.

B-3.   Altenkirch, R.A., Eichhorn, R., and Shang, P.C., "Buoyancy Effects on Flames Spreading Down Thermally Thin Fuels," <u>Combustion and Flame</u>, Vol. 37, (1980), pp. 71-83.

B-4.   Kashiwagi, T. and Newman, D.L., "Flame Spread Over an Inclined Thin Fuel Surface," <u>Combustion and Flame</u>, Vol. 26, (1976), pp. 163-177.

B-5.   Fernandez-Pello, A.C., "Downward Flame Spread Under the Influence of Externally Applied Thermal Radiation," <u>Combustion Science and Technology</u>, Vol. 17, (1977), pp. 1-9.

B-6.   Olson, S.L., "The Effect of Microgravity on Flame Spread Over a Thin Fuel," NASA Technical Memorandum 100195, December 1987.

B-7.   West, J., Bhattacharjee, S. and Altenkirch, R.A., "Flame Temperature and Radiative Effects on Flame Spread over Thermally Thick Fuels," *Chemical and Physical Processes in Combustion*, 1990 Fall Technical Meeting, Eastern Section of the Combustion Institute, Paper 53.

B-8.   Bhattacharjee, S. and Altenkirch, R.A., "Radiation-Controlled Opposed-Flow Flame Spread in a Microgravity Environment," 23rd Int. Sym. on Combustion, 1990.

B-9.   Frey, A.E. and T'ien, J.S., "A Theory of Flame Spread over a Solid Fuel Including Finite-Rate Chemical Kinetics," *Combustion and Flame*, Vol. 36, (1979), pp. 263-289.

B-10.   Dietenberger, M.A., "Formulae to Predict Piloted Ignition and Flame Spread on Composite Solid Fuels in Extreme Environments and Their Validation with Experiments," Ph.D. Thesis in Mechanical Engineering, University of Dayton, 1991.

B-11.   Mao, C.P., Kodama, H., and Fernandez-Pello, A.C., "Convective Structure of a Diffusion Flame over a Flat Combustible Surface," *Combustion and Flame*, Vol. 57, (1984), pp. 209-236.

B-12.   Sibulkin, M., and Gale, T., "Effects of External Radiation on Solid-Fuel Diffusion Flames," *Journal of Fire Science*, Vol. 2, (Jan/Feb 1984), pp. 70-81.

B-13.   Hirano, T. and Sato, K., "Effects of Radiation and Convection on Gas Velocity and Temperature Profiles of Flames Spreading over Paper," 15th Int. Sym. on Combustion, Tokyo, Japan, August 25-31, 1974.

B-14.   Olson, S.L., "Mechanisms of Micogravity Flame Spread over a Thin Solid Fuel: Oxygen and Opposed Flow Effects," *Combustion Science and Technology*, Vol. 76, (1991), pp. 233-249.

B-15.   <u>Handbook of Heat Transfer</u>, W.M Rohsenow and J.P. Hartnett (Eds.), New York: McGraw-Hill, Inc. (1973).

B-16.   Harkleroad, M., Quintiere, J., and Walton, W., "Radiative Ignition and Opposed Flow Flame Spread Measurements on Materials," DOT/FAA/CT 83/28, August 1983.

B-17.   Babrauskas, V. and Parker, W.J., "Ignitability Measurements with the Cone Calorimeter," NBSIR-86-3445, September, 1986.

B-18.   Ito, A. and Kashiwagi, T., "Characterization of Flame Spread over PMMA Using Holographic Interferometry Sample Orientation Effects," *Combustion and Flame*, Vol. 71, No. 2, (February 1988), pp. 189-202.

B-19.   Dipert, R.A., "Application of Flame Spread Modeling to Flame Spread on Horizontal Samples," M.S. Thesis in Fire Protection Engineering, Worcester Polytechnic Institute, July 1984.

B-20.   Orloff, L., deRis, J., and Tewarson, A., "Thermal Properties of PMMA at Elevated Temperatures," FMRC, Tech. Rept. 2235-2 (1974).

B-21.   Fernandez-Pello, A. and Williams, F.A., "Laminar Flame Spread Over PMMA Surfaces," *Fire and Explosion Research*, (1975), pp. 217-231.

B-22.   Altenkirch, R.A., Eichhorn, R., and Rizvi, A.R., "Correlating Downward Flame Spread Rates for Thick Fuel Beds," *Combustion Science and Technology*, Vol. 32, (1983), pp. 49-66.

B-23.   Dietenberger, M.A., "Technical Reference and User's Guide for FAST/FFM (Version 3)," NIST-GCR-91-589, 1991.

B-24.   "Standard Test Method for Determining Material Ignition and Flame Spread Properties," ASTM Designation E 1321-90.

B-25.   Sibulkin, M., Kulkarni, A.K., and Annamalai, K., "Effects of Radiation on the Burning of Vertical Fuel Surfaces," 18th Int. Sym. on Combustion, (1981), pp. 611-617.

Appendix A

Furniture Fire Model Predictions of Furniture Calorimeter Burn Tests

The following pages represent the first journal article that was submitted in September 1991 to Dr. V. Babrauskas at the National Institute of Standards and Technology for publication in the Fire Safety Journal.

FURNITURE FIRE MODEL (FFM) PREDICTIONS OF FURNITURE CALORIMETER BURN TESTS

By Mark A. Dietenberger
University of Dayton Research Institute
Dayton Ohio 45469

Abstract

This paper reports on the development of the furniture fire model (FFM). The model simulations are compared with the furniture calorimeter burn tests for different upholstered furnitures. The model constants are calibrated substantially with the bench-scale data. Data were provided from tests of the fabric/foam cushions in the cone calorimeter and the ignition/flame spread apparatus. Using the FFM, several configurations of the upholstered furnitures were considered: (1) the four-cushion chair for each of the six cushion types, (2) five mockup shapes for the cushion with the fire retarded foam/olefin fabric, and (3) four mockup shapes for the cushion with the non-fire retarded foam/olefin fabric. The FFM successfully predicted the transient heat and mass release rates measured by the furniture calorimeter, particularly their peak values and burn durations.

I. INTRODUCTION

Residential fires account for the vast majority of all civilian fire deaths, injuries, and property losses. Statistics for the United States show that upholstered furniture is most often the first item ignited. The hazards to the building occupants from the furniture fire are most sensitive to the rate of fire growth[1]. The main objective for the Furniture Fire Model (FFM)[2,3] is to predict full-scale fire development using data from the bench-scale fire testings. The model must also provide a practical and fundamental description of all relevant fire processes. To

model the spread of fire, smoke, and toxic gases for determining the hazard of fire scenarios, the FFM is structured as a sub-unit of the advanced room fire model (FAST[4]) which can be implemented on a personal computer (PC). The combined models of FAST and FFM have the potential to reduce the number of costly full-scale tests. They also provide the fire protection community with improved predictive capability for fire hazard, particularly when evaluating newer materials in different environments.

There are fire spread models for specialized fire scenarios that have some similar features to FFM. Atreya[5] developed a horizontal fire spread model over wood. Since the flame spread is concentric around a point ignition source, he used small increments of surface distances to resolve conductive and radiative flame heat fluxes on the virgin wood. The flame front was advanced whenever a surface ring element reached the ignition state. The flame radiative heat flux was calculated from knowing the flame structure, which in turn was related to the burn rate of the ignited regions. The formulae developed by Atreya are specialized to a concentric pool fire over a horizontal slab. These formulae are not extendable to a more general geometry, but they demonstrated the effectiveness of his model.

Recently, Delichatsios et al.[6] documented an upward fire spread code. Their geometry consisted of narrow long strips which ignited when heated by the wall fire plume. Small increments of the vertical surface distance were not needed because of the large heating lengths of the fire plume. The future development of their model is to consider charring solids and the downward/lateral flame spread process. Currently, two more upward fire spread models are also at about the same stage of development. Mitler's[7] approach is most similar to Delichatsios et

al., although there are significant differences in modeling the material transient heating and pyrolysis. Kim and Kulkarni[8] chose to integrate the upward flame spread rate.

Smith and Satija[9] described a detailed wall-fire spread model that predated all the models referenced above. They solved the material heat-up problem with the finite difference technique and the fire plume issue by using the detailed incremental volume approach. However, the analysis for the thermal radiation fluxes and the ignition criteria were based on very simplified models. The upward flame spread involved a sequence of ignited narrow long strips, while the lateral flame spread was solved by integrating the creeping flame spread rate. Each widening burning narrow strip utilized a heat release rate as a function of time and irradiance. Several model constants needed calibration, but were not fully tabulated or explained.

Modeling furniture fire growth involves unique considerations. While piloted ignition can occur anywhere on any cushion, the resulting fire can develop into multiple pool and wall flames on generally shaped furniture. The empirical approach to defining the burn-rate profile[10] can lead to poor results when extended to different furniture fire scenarios. The three-dimensional requirement led to a practical, 3-D, and gray thermal radiation analysis, which was developed in our earliest FFM work[11]. Another consideration was the goal to use only the bench-scale fire data in a practical and accurate scheme to calculate the furniture fire. The experimental results on flame spread[12,13,14] suggested using the long-range radiative heat flux to preheat the solid fuel, and the flame conductive heat flux to calculate the rate of flame spread over the preheated surface. Thus it was recognized early[11] that flame irradiance can ignite secondary burning regions on adjacent cushions. Concurrently, the flame front must be calculated as the time

integration of the flame spread rate. This allowed the use of arbitrarily sized surface elements, which significantly reduced the computationally intensive calculations of the thermal radiation field. The cone calorimeter data was next processed and scaled[15] in a successful scheme to calculate the heat and mass release flux from an element as a function of burn history, irradiance, and flame size. Limited validation of FFM was achieved[16] and a full documentation of FAST/FFM was later provided[2].

The FAST/FFM has some generalizing features as compared to the previously mentioned models. Instead of the horizontal burning circles used in the Atreya model and the vertical burning rectangles used in the wall fire models, the FFM uses the generalized burning polygons on arbitrarily orientated panels. Rather than analytically evaluating viewfactors between definitely shaped objects, the FFM uses viewfactors evaluated numerically for arbitrarily shaped flames, furniture, and room. To save on computation time, the FFM uses the accurate formulae for the material heating and for the size of the fire plume. These analytical equations can easily be upgraded to more advanced models without affecting the numerics or structure of the code. The coupling of FAST and FFM should permit calculations of different flashover types, such as (1) accelerative furnishing fire spread due to radiative heating from the upper gas layer, or (2) flaming ignition conditions within the upper gas layer due to the accelerative furnishing burn rate.

This paper compares FAST/FFM predictions and the full-scale burn test data from the furniture calorimeter[5,17,18]. The features of the FFM are first summarized in Section 2. Details of FFM can be found in References 2 and 3. Section 3 presents the furniture calorimeter data and the corresponding bench-scale data. The model constants described in the summary of FFM

are then calibrated and tabulated. The FFM predictions of the heat and fuel release rate as a function of time are compared with the full-scale data in Section 4. The conclusion follows in Section 5.

2. FURNITURE FIRE MODEL

Burning is a complex process consisting of three dissimilar types of reactions which usually develop concurrently: (1) the endothermic pyrolysis of the fuel, (2) the flaming combustion of some or all of the gaseous decomposition products, and (3) the oxidation of char (or smoldering combustion). Since pyrolysis is endothermic, the heat may originate from external radiant sources, the flame, or the oxidizing char. The combustion by-products of soot and the gaseous products of water and carbon dioxide emit thermal radiation at the flame temperature and attenuate external radiant sources. The buoyant air flow into the flame convectively cools the virgin surfaces and heats the burning surfaces. These physical processes occur on a small time scale and are treated as quasi-steady in FFM.

Additional physical processes considered for FFM that have relatively large time scales are (1) transient heating of the furniture material to the state of pyrolysis or ignition, (2) time-dependent flame spreading in any surface direction, (3) and transient burning history of the charring solid. The three-dimensional aspects of FAST/FFM include the furniture constructed of connected panels; several flames attached to pyrolyzing polygonal bases and sides; a radiation heat exchange between facets of walls, objects, flames, and gases; and the construction of multiple zones of gases in the rooms. To obtain accurate and practical calculations, FFM relies

on scaling the cone calorimeter and the flame spreading data instead of on detailed field solutions for the burning solid and its attached diffusion flame. The scaling procedures are explained as follows.

2.1 Ignition/Flame Spread Scaling

The upholstered furniture materials were shown to have a thermally thin behavior for ignition and flame spread[11] based on the bench-scale data[19]. The surface temperature prediction over a time step for a virgin fabric/foam cushion, in response to a irradiance load and cooled by a linearized radiant and convective heat loss, was formulated as[2],

$$T_s(t+\Delta t) = T_{eq} + (T_s(t) - T_{eq}) \exp\left(\frac{-(h_r + h_c) \Delta t}{\rho C_p \delta}\right) \qquad (1)$$

where:

$$h_c(T_{eq} - T_a) = \dot{Q}_r''(\infty) = \dot{Q}_r''(t) + h_r(T_s(t) - T_{eq}) \qquad (2)$$

$$h_r = \epsilon_s \sigma(T_s^2(t) + T_{eq}^2)(T_s(t) + T_{eq}) \approx 4\epsilon_s \sigma T_s^3(t) \qquad (3)$$

$$\dot{Q}_{ri}'' = \dot{Q}_r''(t) + \epsilon_s \sigma (T_s^4(t) - T_a^4) \qquad (4)$$

These variables are defined in Section 6, Nomenclature. If $T_s(0) = T_a$, $t = 0$, and $\Delta t = t_{ig}$, then a time to ignition versus irradiance data can be fitted with these equations to derive the thermal thickness and surface ignition temperature[11]. Since the irradiance changes somewhat with time and varies with the geometry in a furniture fire, Eq. (1) is used to predict surface element temperature. This temperature is described as the preheated temperature during flame spread over a surface element.

Before arrival of the flame, the surface element midpoint is at some distance from the flame front, which is moving at the flame spread rate. This means the total heat flux distribution between the flame front (ignition point) and the surface element midpoint is moving over the element at the flame spread rate. The time interval in which this process occurs is the preheated length over the flame spread rate (s_e/V_f). In the thermal response analysis, incremental time is replaced by incremental distance $(ds/V_f = dt)$ and the total heat flux distribution within the preheated length is divided into its components. Each of the total heat-flux components are modeled as follows. The radiant/convective heat exchange between the surface and the air is treated as a product of the linearized heat transfer coefficient and the temperature difference between the air and the surface. The irradiance from external sources is treated as constant over the distance s_e. The radiative heat flux from the adjacent fire plume is modeled as a decreasing exponential function of distance, s. Lastly, the conductive heat flux from the flame foot is assumed constant over the distance, l_f. Although the conductive heat flux is described better as a decreasing exponential function of s[20], the results are the same if $(h_r+h_c) l_f \ll \rho C_p \delta V_f$. Using the Laplace transform to analyze the thermal response, the analytical solution for the flame spread rate is,

$$
T_{ig} = T_s + \frac{\dot{Q}_f'' l_f + \dot{Q}_{re}'' s_e + \dot{Q}_{rf}'' s_e \exp(-s_e/l_p)}{\rho C_p \delta V_f} + \frac{\dot{Q}_{rf}'' l_p - \dot{Q}_{rf}'' (l_p + s_e) \exp(-s_e/l_p)}{(h_r + h_c) l_p + \rho C_p \delta V_f}
$$

(5)

This equation can be inverted algebraically to solve explicitly for the flame spread velocity, V_f. Thus, the flame spread rate is a minimum at the onset of piloted ignition because the flame and external irradiances are minuscule. This flame spread rate is also a function of some additional parameters: oxygen mass fraction, ambient pressure, ambient temperature, and surface

orientation[20]. These parameters remain constant during a fire scenario involving furniture in a large open room. In any case, the irradiances eventually dominate the flame spread after a period of time. Included in FFM is the possibility that the preheated temperature on a furniture surface element will reach ignition prior to the arrival of the flame front. The remaining features of the flame spreading procedure in FFM are the capability to (a) merge overlapping burning polygonal regions and (b) create new burning regions in the adjoining panels as a result of flame spreading, thermal ignitions, or even new piloted ignition.

2.2   Heat and Mass Release Scaling

In FFM, the burning regions are analyzed to determine the flame structures (pool or wall fires) attached to them, and their corresponding fuel and heat release rates. A multistep process is involved to arrive at the fuel and heat release rates of a furniture fire. The first step is to re-scale the cone calorimeter data so they are valid for varying irradiance levels and for any point in the burning history of an element. In the second step, FFM calculates the burn history as a function of burning time. The receding thickness of the burning element is assumed proportional to the scaled time, since the cone calorimeter does not have the thickness with time of the burning sample in its database. The scaled database supplies the stoichiometric heat of combustion and the effective heat of pyrolysis as a function of the burn history. In the last step, FFM solves for the coupled short-time processes in the multi flames over their respective burning areas, including the soot and combustion products formation (explained further in Section 2.3) and the thermal radiation/convective heat transfers between objects and gas layers within the room.

The net surface heat flux on the material sample is given by,

$$\dot{Q}_s'' = \dot{Q}_c'' + \dot{Q}_r'' + \dot{Q}_o'' \tag{6}$$

where the convective heat flux, $\dot{Q}_c''$, and the radiative heat fluxes, $\dot{Q}_r''$, from the flame, the attenuated cone heater, and the burning surfaces are considered. The last term, the scaled heat flux constant, $\dot{Q}_o''$, is calibrated to correct for systematic errors in the other heat flux terms and unaccounted physical processes. The heat release flux is scaled to be equivalent to the quasi-stoichiometric heat of combustion divided by the effective heat of pyrolysis. The mass release flux is scaled to be equivalent to the inverse of the effective heat of pyrolysis. The appropriate equations for the scaled heat and mass release flux are:

$$q^* = \dot{q}_{st}'' / \dot{Q}_s'' = [\dot{q}_{cone}'' + \dot{m}_f'' (F_{s_{exit}} H_c + F_{co} H_{co})] / \dot{Q}_s'' \tag{7}$$

and

$$m^* = \dot{m}_f'' / \dot{Q}_s''. \tag{8}$$

The burn history is best represented by an effective heat release per area as given by

$$t^*(t, G) = \int_o^t \dot{q}_{st}'' (1 + G) \, dt \tag{9}$$

where:

$$G = \frac{t_{ref}^*(t_{end}, 0) - t^*(t_{end}, 0)}{t^*(t_{end}, 0) - e\, t_{ref}^*(t_{end}, 0)} \tag{10}$$

for inside the domain,

$$\frac{ed}{1 + d} \leq \frac{t^*(t, 0)}{t_{ref}^*(t_{end}, 0)} \leq \frac{t^*(t_{end}, 0)}{t_{ref}^*(t_{end}, 0)} - \frac{e}{1 + d} \qquad (11)$$

and $G = 0$ for outside the domain. G is a time stretching parameter that ensures the scaled burnout time is identical for the similar materials. The referenced burn history, $t_{ref}^*(t_{end}, 0)$, is set to the minimum of all burn histories at the end time for similar materials. Setting $e = 0.5$ will cause half the total burn history to be affected by time stretching, and setting $d = 1$ will put the affected region directly in the middle of the total burn history. Other values of d and e can be tailored to represent composite materials. The objective of calibrating the scaling constants is to make the plots of q^* or m^* versus t^* for different cone heater radiances collapse to a single curve.

To apply the scaled data to FFM, a net surface heat flux of a burning surface element is calculated for a current real time. That is, the convective and radiative surface heat fluxes are calculated from the furniture fire geometry rather than from the cone calorimeter geometry. To utilize this net surface heat flux, Eq. (7) was substituted into Eq. (9) and the resulting equation was rearranged to obtain the increment in the burn history as a function of the increment in the real time as

$$\int_{t_i^*}^{t_{i+1}^*} \frac{dt^*}{q^*(t^*) \, [1 + G(t^*)]} = \int_{t_i}^{t_{i+1}} \dot{Q}_s''(t) \, dt. \qquad (12)$$

Since the values for the burn history, the flame spread region, and the net surface heat fluxes are now known, the fuel and heat release rates of the flame are by definition:

$$\dot{m}_{fuel} = \sum_i \dot{Q}''_{s_i}(t) \; m^*(t_i^*) \; A_i \qquad (13)$$

and

$$\dot{q} = \sum_i \dot{Q}''_{s_i}(t) \; [q^* - m^*(F_s H_c + F_{co} H_{co})]_{t_i^*} \; A_i. \qquad (14)$$

The heat release rate of the flame is the summation of the heat release flux from each element times the area of the burning elements. The heat release flux is defined as the quasi-stoichiometric heat release flux minus the heat release flux of the incomplete combustion products of soot and carbon monoxide. The mass fractions of fuel for soot and carbon monoxide are explained further in Section 2.3.

In the next step of FFM calculations, the fuel and heat release rates of the flame above its burning region are used as inputs into formulae to determine the flame size and the soot quantities in the flaming zones. This structure of the flames is input into the Hottel zonal, gray body thermal radiation model, which is described in more detail in References 2 and 3. The solution of the radiation field provides the values of the radiative surface heat fluxes. The approximate boundary layer analysis of the different flames provides the values of the convective heat fluxes. The inner computational loop for the short-time processes iterates back to Eq. (13) with the updated surface heat fluxes. The outer computational loop takes a time step before iterating back to Eq. (1) to calculate the surface temperature, the flame spread, and the burn history as a function of time. Thus the accelerative growth of the heat release rate is due to accelerative flame spreading and growth of the flame shape. When the surface elements begin to burn out, the heat release rate decreases. Further details on the FAST/FFM calculation system are given in Reference 2.

2.3   Soot and Combustion Products Scaling

The mass rate of the combustion products exiting from the flame is given by

$$\dot{m}_j = \sum_i \dot{Q}''_{s_i}(t) \; m^*(t_i^*) \; F_j(t_i^*) \; A_i. \tag{15}$$

The cone calorimeter data for the mass fraction of the combustion products, F_j, has been rescaled as a function of the burn history, t^*. The scaling for the soot production is different in that it is also affected by the size of the flame and the heat of combustion for the fire. This is given by the following equation[2]:

$$F_s = C(T_f, T_a) \frac{k_{s,flame}}{\sigma_s^\theta} \frac{\dot{q}}{\dot{m}_{fuel}} \tag{16}$$

where:

$$k_{s,flame} L = (1.5 \; k_{s,max} L)^{3/2} \quad for \quad k_{s,flame} L < 0.3 \tag{17}$$

and

$$k_{s,flame} = k_{s,max} \quad for \quad k_{s,flame} L \geq 0.3. \tag{18}$$

Equations (17) and (18) are the empirical relationships derived[21] for the production of soot within a pool-like diffusion flame. Equation (16) was derived by assuming the net production of soot ceases at the solid flame height and is not depleted when exiting the flame. The calculation of soot in different forms is very significant. In large fires, the soot dominates the thermal radiation, which in turn dominates the fuel pyrolysis and the consequential burning rate. The hot smoke leaving the fire is a major factor in hazard analysis.

3. CALIBRATION OF MODEL CONSTANTS

The full-scale burn tests of upholstered furniture were measured with the furniture calorimeter as reported by Babrauskas and Krasny in Reference 18. Thirteen of these full-scale burns were selected for comparison with FFM predictions and are summarized in Table 1. Three basic groups of full-scale burns were effective in validating the model.

The first group involved burning a four-cushioned chair. Six separate burns were performed using different foam/fabric combinations for each burn. Very few scaling constants were calibrated with this data. The remaining scaling constants were calibrated with the bench-scale data. The second group included burning fire retarded polyurethane foam with light olefin fabric (FR-PU/LO) using five different furniture constructions. The third group was similar, except the foam material was not fire retarded. These last two groups required no further refinement to the values of the scaling constants. These constants are listed in Table 2. The process of calibrating all the model constants are as follows.

The values for surface ignition temperature and the thermal thickness are obtained from fitting Eq. (1) to the ignition time versus irradiance data[19]. The foam/fabric cushion samples used in the bench-scale apparatus are similar to those used in the furniture[18]. The evaluation of the flame spread constant is more subtle.

The flame spread equation, Eq. (5), was developed specifically for FFM. The preheat temperature, T_s, includes the effect of all radiant sources (including that of the flame plume)

TABLE A-1

SELECTION AND ORGANIZATION OF FULL- AND BENCH-SCALE TESTS

Group No.	Mockup Configuration	Foam/Fabric (See Ref. 5)	Furniture Calorimeter Data (Refs. 5, 6, & 7)	Cone Calorimeter Data (Ref. 5)	Flame Spread Data	Thermal Ignition Data
A.1	4-Cushion Chair	NFR PU/LO	Test 12	Cone radiance is 25 kW/m^2. Scaling constants calibrated on similar materials having several cone radiance values (Ref.9).	Mockup fire growth on VCR. Bench scale data in Ref. 5 and processed in Ref. 8.	Similar to material in Ref. 5 and processed in Ref. 8.
A.2	4-Cushion Chair	FR PU/LO	Test 07			
A.3	4-Cushion Chair	FR PU/HO	Test 14			
A.4	4-Cushion Chair	FR PU/LC	Test 21			
A.5	4-Cushion Chair	NFR PU/HC	Test 20			
A.6	4-Cushion Chair	FR PU/HC	Test 17			
A.7	1-Cushion Seat	FR PU/LO	Test 03			
A.8	2-Cushion Seat/Back	FR PU/LO	Test 04			
A.9	3-Cushion Chair	FR PU/LO	Test 05			
A.10	6-Cushion Couch	FR PU/LO	Test 06			
A.11	1-Cushion Seat	NFR PU/LO	Test 01			
A.12	2-Cushion Seat/Back	NFR PU/LO	Test 02			
A.13	3-Cushion Chair	NFR PU/LO	Test 11			

TABLE A-2
SCALING CONSTANTS UTILIZED

Foam/Fabric (See Ref. 5)	Ignition/Flame Spread Constants			Burn Rate Constants*	Soot Production Constants	
	T_{ig} (°K)	$\rho c \delta$ (kJ/°Km^2)	$Q''_f \ell_f$ (kW/m)	Q''_0 (kW/m^2)	k_{max} (1/m)	σ^e_s (m^2/kg)
NFR PU/LO	623.3	0.80	0.59	30.0	1.342	5060.0
FR PU/LO	711.3	0.72	0.43	30.0	1.342	4740.0
FR PU/HO	711.3	0.72	0.27	30.0	1.342	5300.0
FR PU/LC	590.7	1.00	0.42	5.0	1.342	3150.0
NFR PU/HC	580.7	2.13	0.46	20.0	1.342	4690.0
FR PU/HC	590.7	2.13	0.27	10.0	1.342	3150.0

*Other burn rate constants for all materials are: $T_b = 700°K$, $e = 0.7$, $d = 100.0$, $\ell_e = 0.07m$

integrated up to the preheat time. This preheat time does not coincide with the flame front, unless the surface element is so small that s_θ approaches zero. The numerator that remains on the right side term of Eq. (5) is the flame spread constant (the product of the flame foot heat flux and the flame foot length). The value of this flame spread constant can be difficult to derive from a flame spread apparatus without using FFM.

The difficulty of deriving a value for the flame spread constant is demonstrated as follows. The imposed irradiance, $\dot{Q}''_{r\theta}$, in a flame spread apparatus and the time of exposure are usually known. Eq. (1) can be used to calculate a surface temperature at the time of exposure such that $\dot{Q}''_{r\theta}$ can be set to zero on the right side of Eq. (5). The real difficulty lies in evaluating the flame plume radiant effects on the flame spread. Without FFM or a similar model, many researchers would simply set s_θ to infinity and use the additional flame spread "constants" of $\dot{Q}''_{rf}$ and l_p. These parameters would be lumped with $\dot{Q}''_f$ and l_f to define an effective flame spread constant, which would change with time for a fire in general. Thus the flame spread apparatus that are most successfully evaluated are those that minimize the fire plume irradiance at the flame front in opposed flow.

Since real fire growths often involve significant fire plume irradiance, FFM uses Eqs. (1) and (5) to provide an essential link to full-scale fire analysis. Indeed, all the full-scale burns selected were ignited at the same seat location--in the middle, 10 cm from the back end. The initial spread from the ignition point results from the flame conductive heat flux distribution. The seat burn area fraction as a function of time in effect provide a bench-scale measurement for

calibrating the flame spread constant in Eq. (5). An example of model prediction versus data for the burn area fraction of the cushions is shown in Figure 1. Acceleration of the flame spread rate is the result of increasing irradiance. The time in which the seat is fully burning depends directly on the value of the flame spread constant and the history of irradiant fluxes. The values of the flame spread constant for each of the six cushion types are listed in Table 2.

A PC-based computer program was developed to assist in manually calibrating the scaling constants for the heat and mass release data from the cone calorimeter. The values of the constants are estimated until the data points of q^* versus t^*, m^* versus t^*, or both at different cone irradiances collapse to a single curve (see Figure 2). The constant surface heat flux, $\dot{Q}_o''$, in Eq. (6) was calibrated solely with the cone calorimeter data for similar materials at different cone radiant fluxes. However, the burn time stretching constants, l_e, d, and e were further refined to scale from a 50-mm thick cushion to a 100-mm thick cushion. In particular, all the ending burn histories, $t^*(t_{end}, 0)$, are adjusted by the ratio (l_e/50mm), where l_e is an effective thickness that scales the total heat release for the additional thickness of the foam. The calibrated constants for each of the six cushion types are listed in Table 2. Further examples of the heat and mass release scaling are given in References 2 and 3.

The maximum soot absorption coefficient corresponded to the polyurethane foam as measured by Bard and Pagni[11]. The specific soot absorption areas were measured in an early cone calorimeter design, which could explain why their values seemed too low. The values for the soot absorption parameters of the six cushions are listed in Table 2.
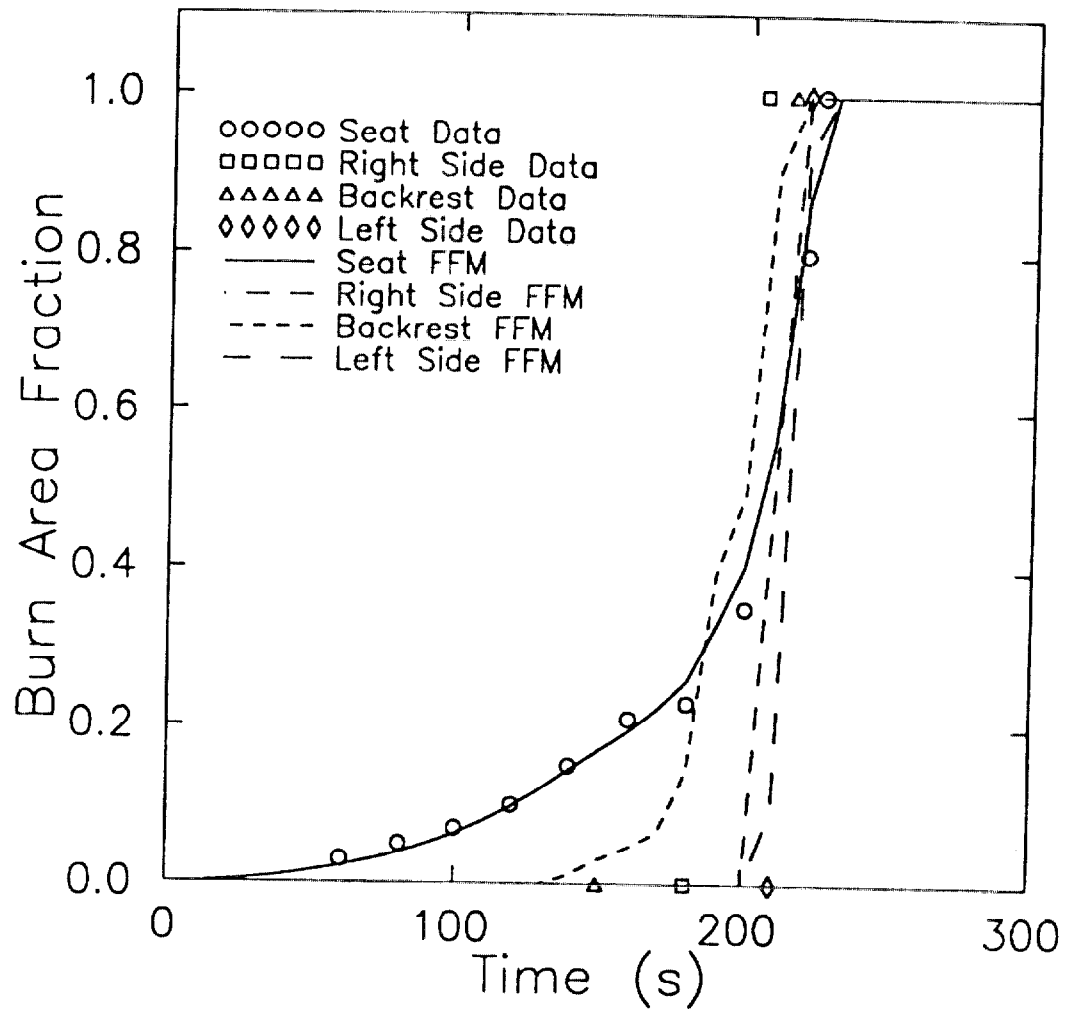
Figure A-1. FFM Prediction and Comparison with Data for FR Foam/HO Fabric, 4-Cushion Mockup.
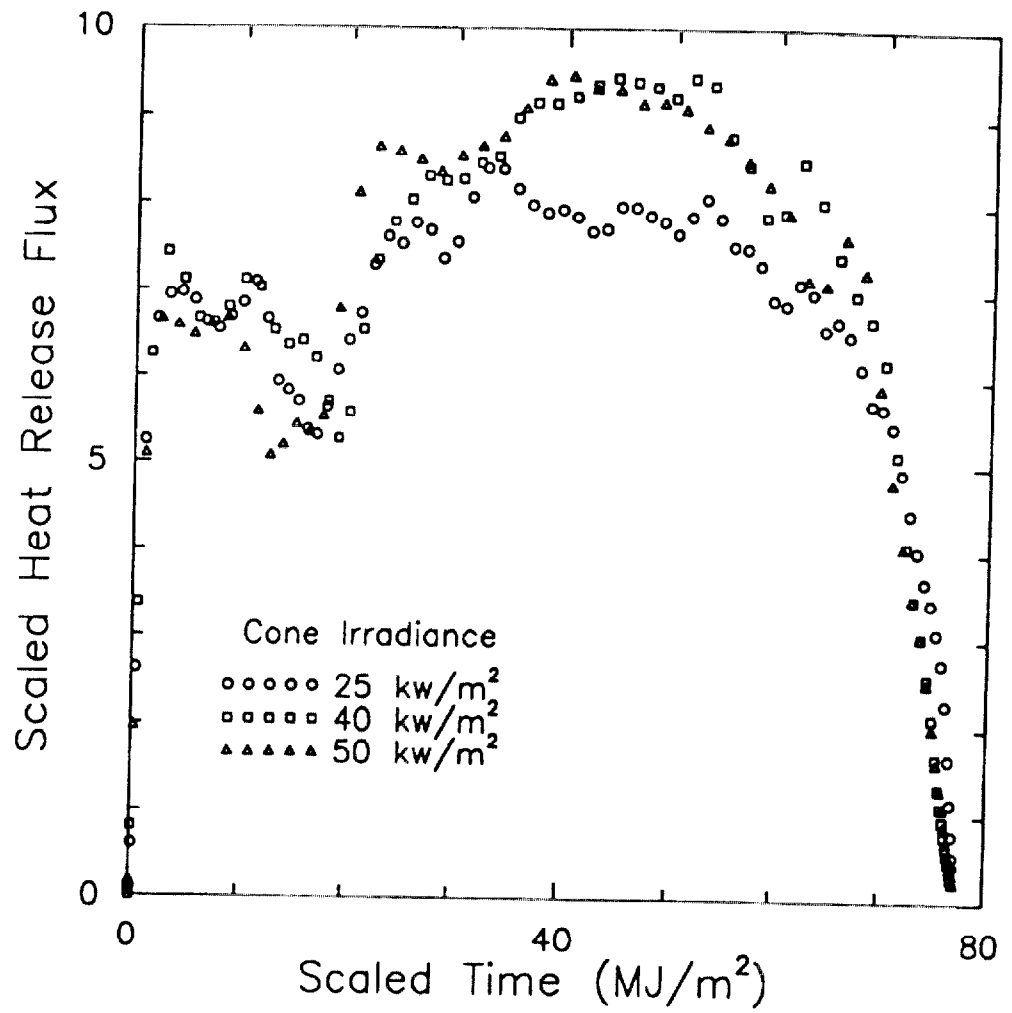
Figure A-2. Scaled Heat Release Flux Versus Scaled Time for LO Fabric/FR PU Foam Material.

Interestingly, the values in each category do not vary significantly from one cushion to the next. This is encouraging because all the scaling constants, except the flame spread constant, are derived from the bench-scale data for the fabric/foam cushions similar to those used in the furniture mockups. Ideally, the cushion samples for the bench-scale testing should be identical to those used in the furniture, and the modern cone calorimeter measurements should be used. Since this ideal situation does not exist for our database, the scaling constants in some instances were slightly changed for a better fit to the full-scale burn rates. Thus, the constants in Table 2 are not totally based on the bench-scale data, although in principle they could be.

4. HEAT AND FUEL RELEASE RATE COMPARISONS

The heat and fuel release rates are the most convenient parameters to measure in a full-scale burn. The availability of data for the burn area fraction of the cushions and for the soot extinction area is desirable, but not crucial, for validating FFM. In our earlier limited validations of FFM[16], the following observations were made. The good comparison with the burn area fraction data for the four-cushion mockups implied a good comparison in the timing of the rapid rise of the heat or fuel release rate. The agreement with the exiting soot extinction area using an independent experimental value for the maximum soot absorption coefficient merely verified the formulae for soot production. Agreement with the observed peak fuel and heat release rate verified the thermal radiation calculations for the flame and mockup geometries. Lastly, the burn-time duration of the heat (or mass) release rate verified the scaling from 50-mm to 100-mm thick cushions. This effect is demonstrated in Figure 3. Thus, when additional variations in the fabric/foam cushions on different mockup geometries are considered, comparison of FFM
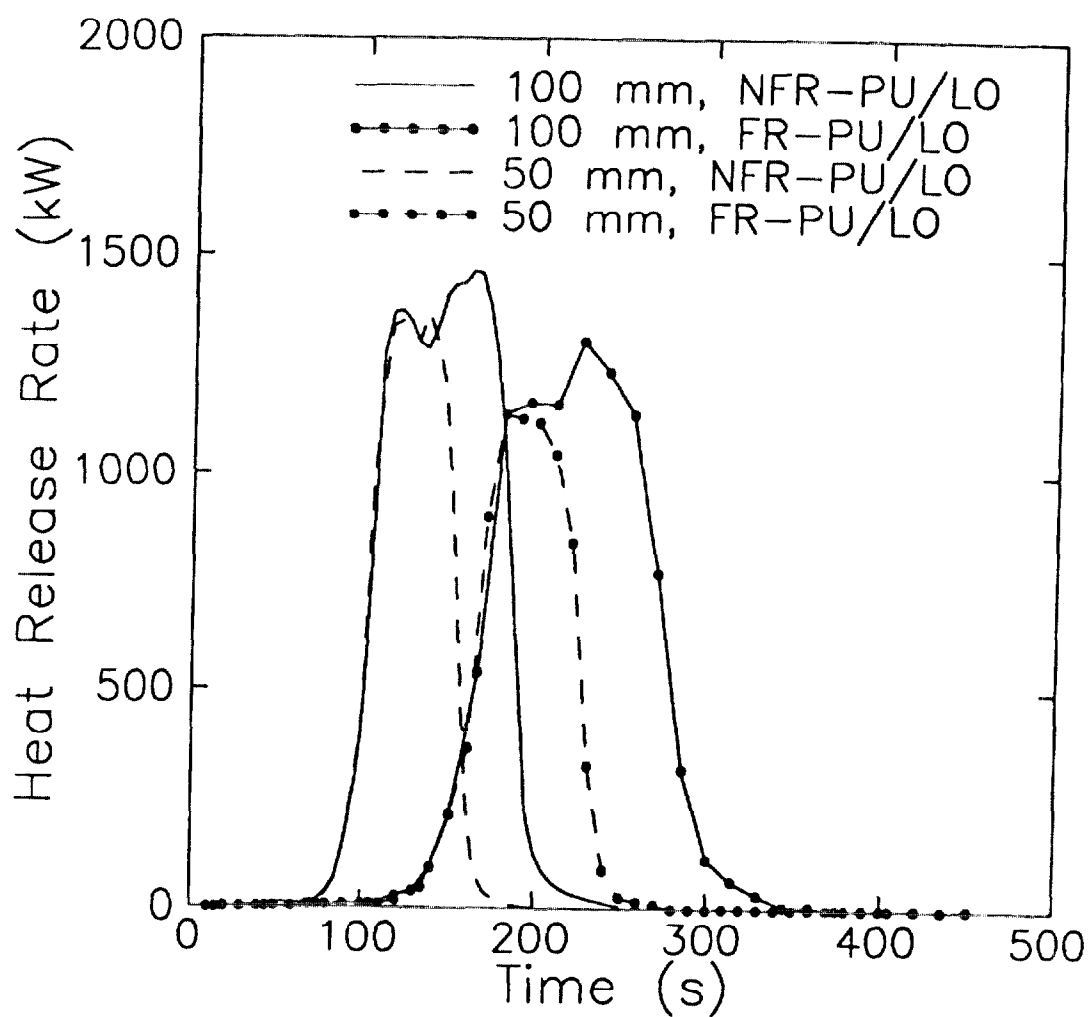
Figure A-3. Effect of Cushion Thickness and Foam Type with the Light Olefin Fabric on Heat Release Rate.

predictions with just the furniture calorimeter data seems sufficient to validate the model for a wide range of applications.

4.1   Four-Cushion Mockups With Six Fabric/Foam Cushion Variations

The first group corresponds to a four-cushion chair and includes six different fabric/foam cushions. The model constants used are listed in Table 2. The model predictions of the fuel and heat release rates and their comparisons with the furniture calorimeter data are shown in Figures 4 through 15. The order of the data plotted begins with the chair of the highest flame spread rate and ends with the chair with the lowest flame spread rate. The peak heat or mass release rates do not follow the same order. Some of the major features, however, are quantitatively predicted by FFM. The features include the timing and value of the peak heat and mass release rate and the peak width. Even when these features change by about an order of magnitude, the model does quite well. Notably, the double peak feature of the heat and mass release rates for the heavy cotton fabric is captured by FFM. Even better results might have been obtained if the cone calorimeter data was also available at lower and higher cone irradiances than that of the 25 kW/m^2 used in FFM predictions.

4.2   FR-PU/LO Cushion With Five Mock-up Variations

The second group included burning fire retarded polyurethane foam with light olefin fabric (FR-PU/LO) using five different furniture constructions. The comparison with the furniture calorimeter data for one-, two-, three-, four-, and six-cushioned mock-ups (see Figure 16) are

A-23

Figure A-4. FFM Mass Release Predictions and the Data for NFR PU/LO.

Figure A-5.   FFM Heat Release Predictions and the Data for NFR PU/LO.

Figure A-6.   FFM Mass Release Predictions and the Data for FR PU/LO.

Figure A-7.   FFM Heat Release Predictions and the Data for FR PU/LO.

Figure A-8. FFM Mass Release Predictions and the Data for FR PU/HO Cushions.

Figure A-9. FFM Heat Release Predictions and the Data for FR PU/HO Cushions.

Figure A-10. FFM Mass Release Predictions and the Data for FR PU/LC Cushions.

Figure A-11. FFM Heat Release Predictions and the Data for FR PU/LC Cushions.
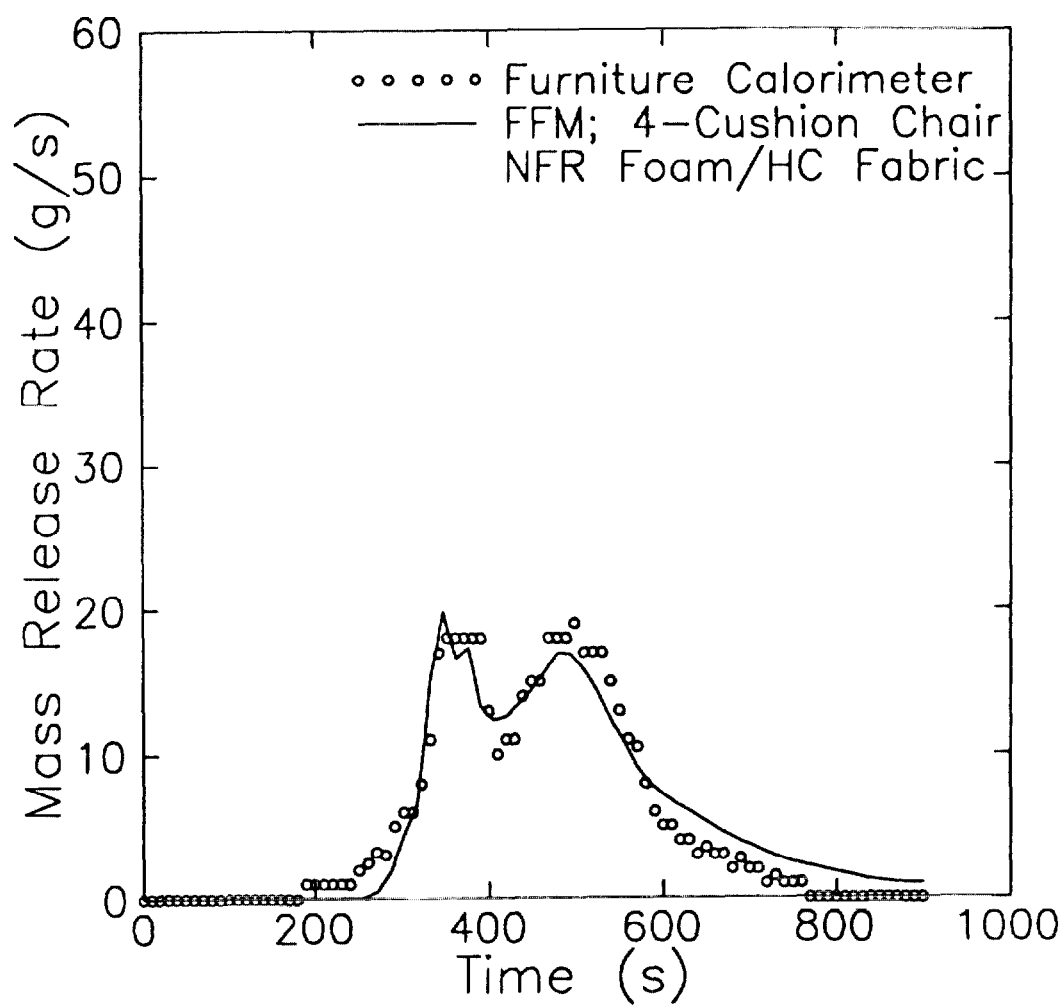
Figure A-12. FFM Mass Release Predictions and the Data for NFR PU/HC Cushions.
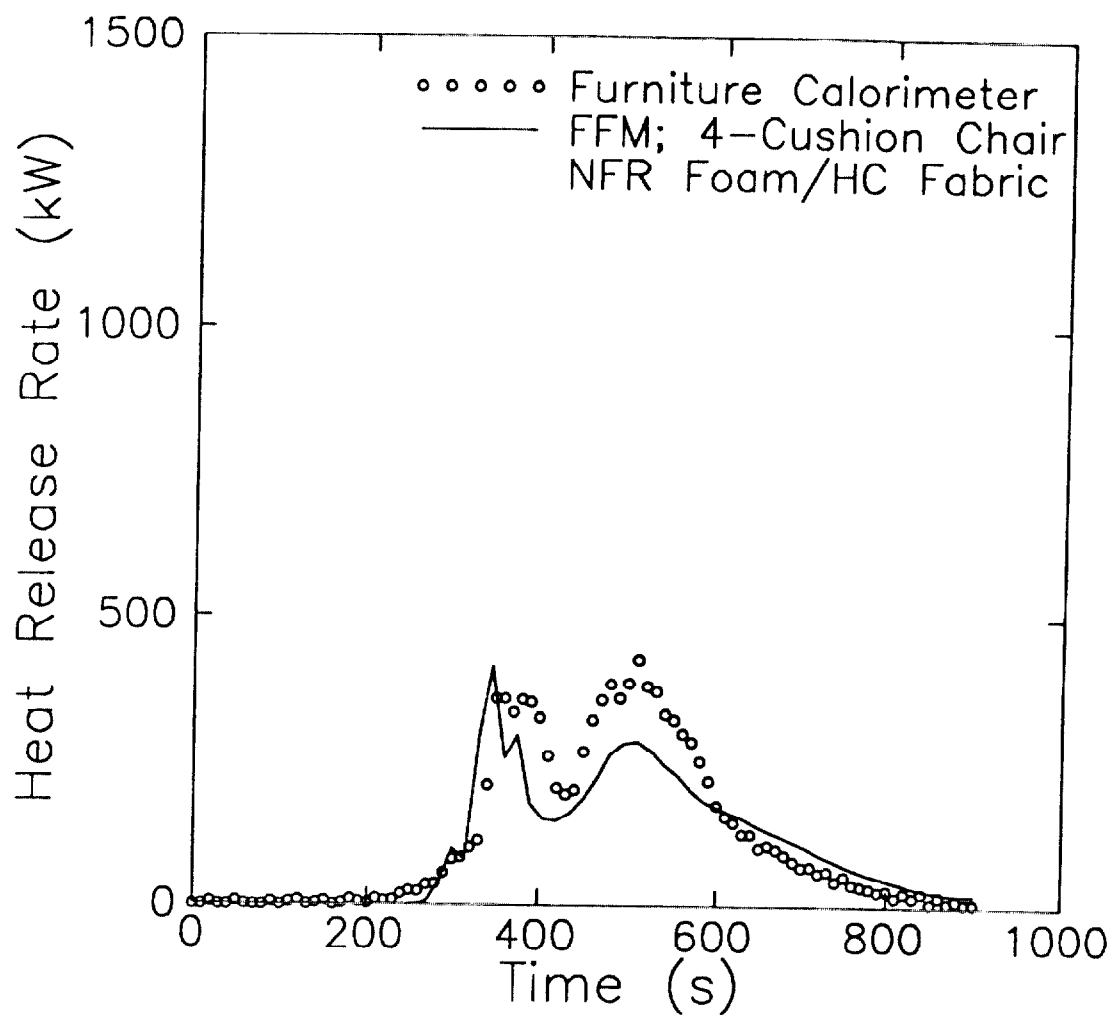
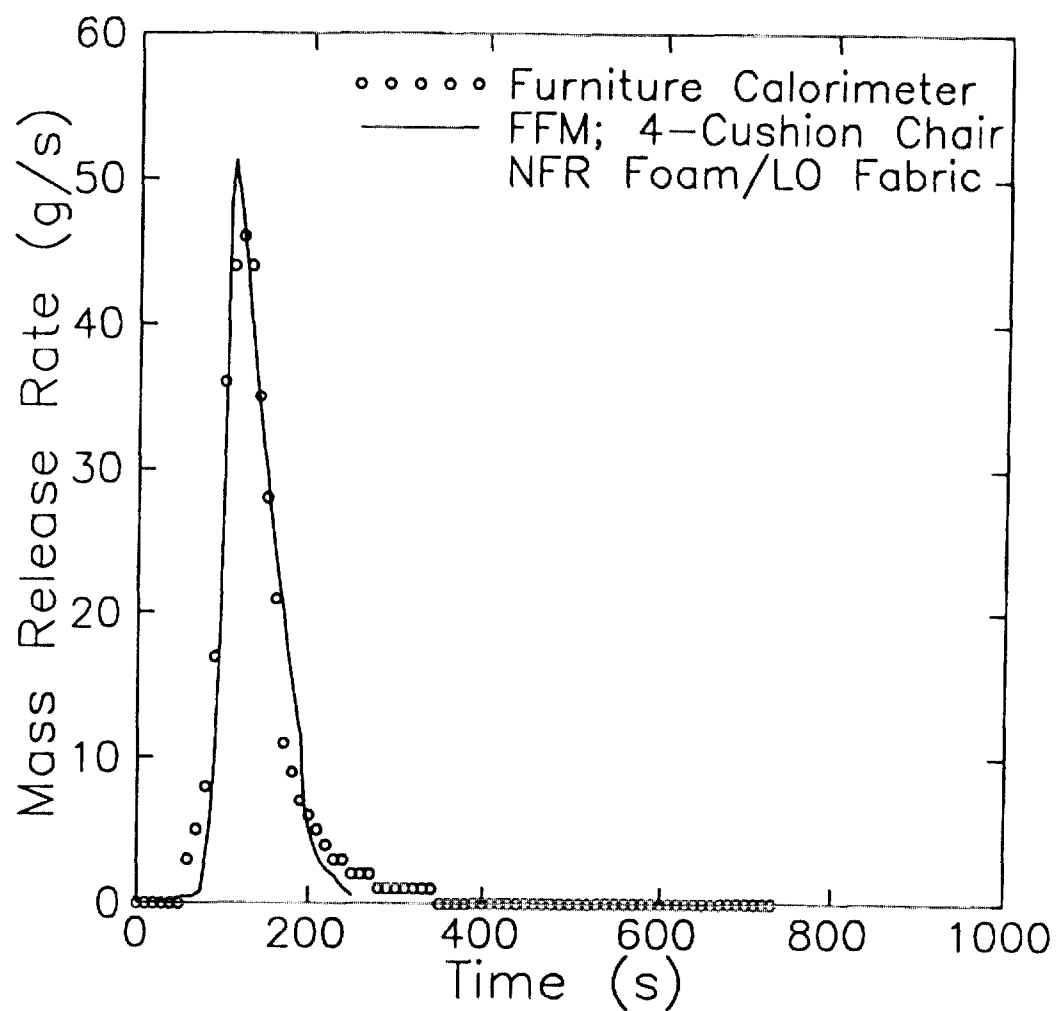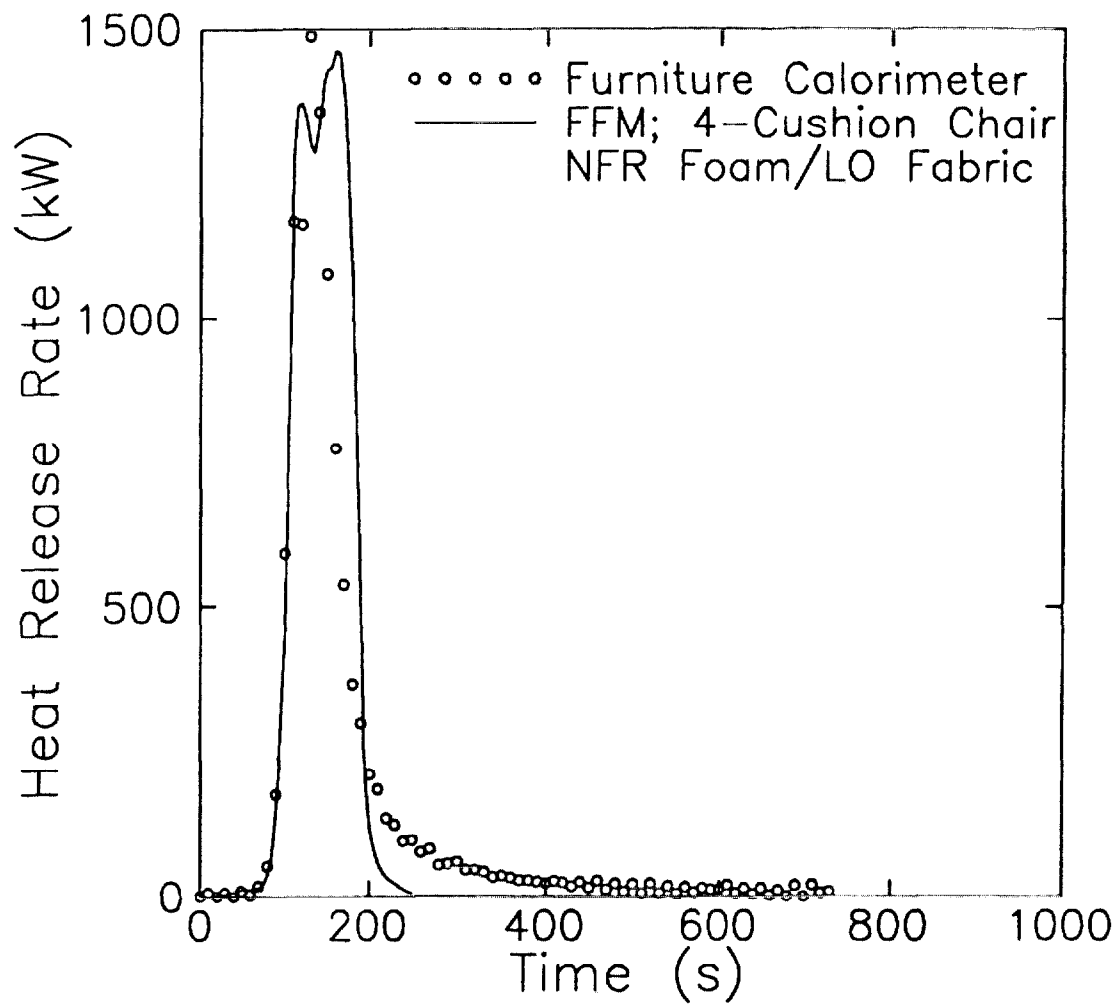Figure A-13. FFM Heat Release Predictions and the Data for NFR PU/HC Cushions.
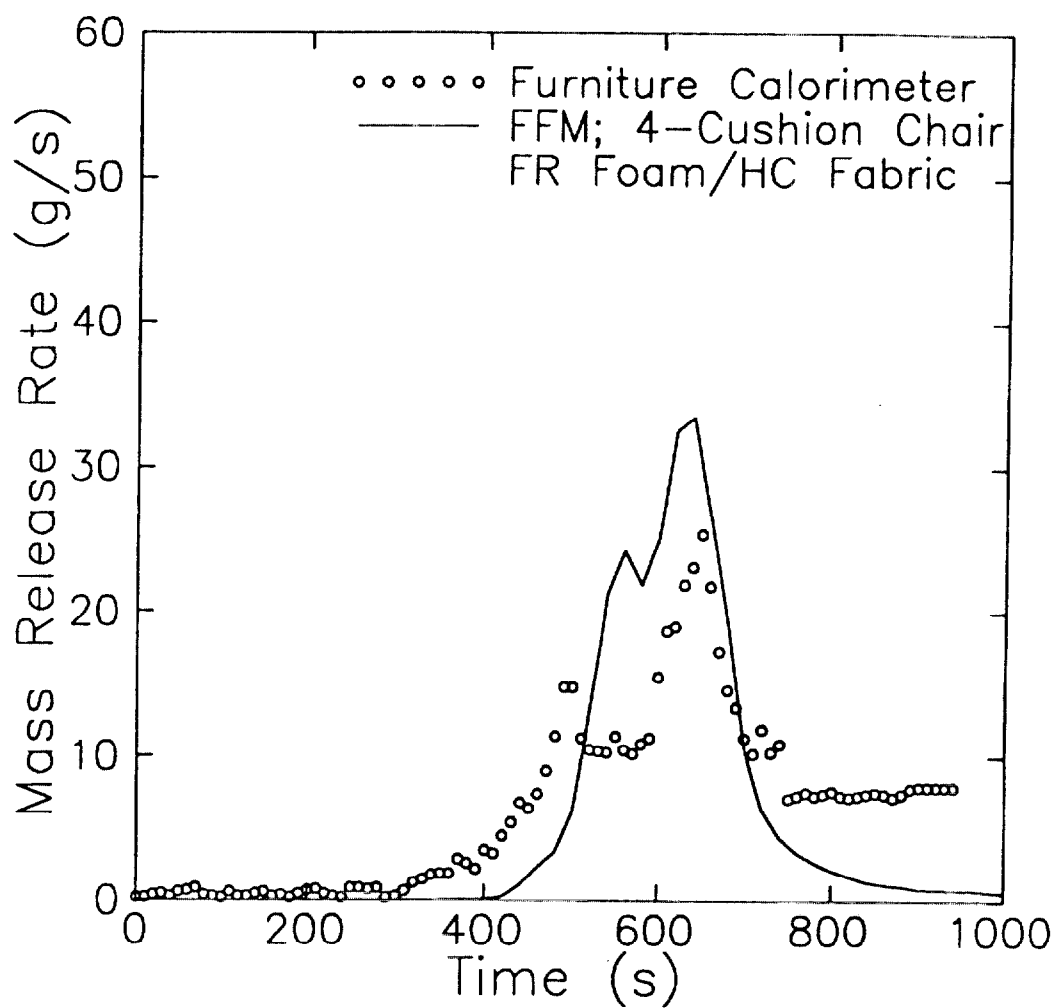
Figure A-14. FFM Mass Release Predictions and the Data for FR PU/HC Cushions.

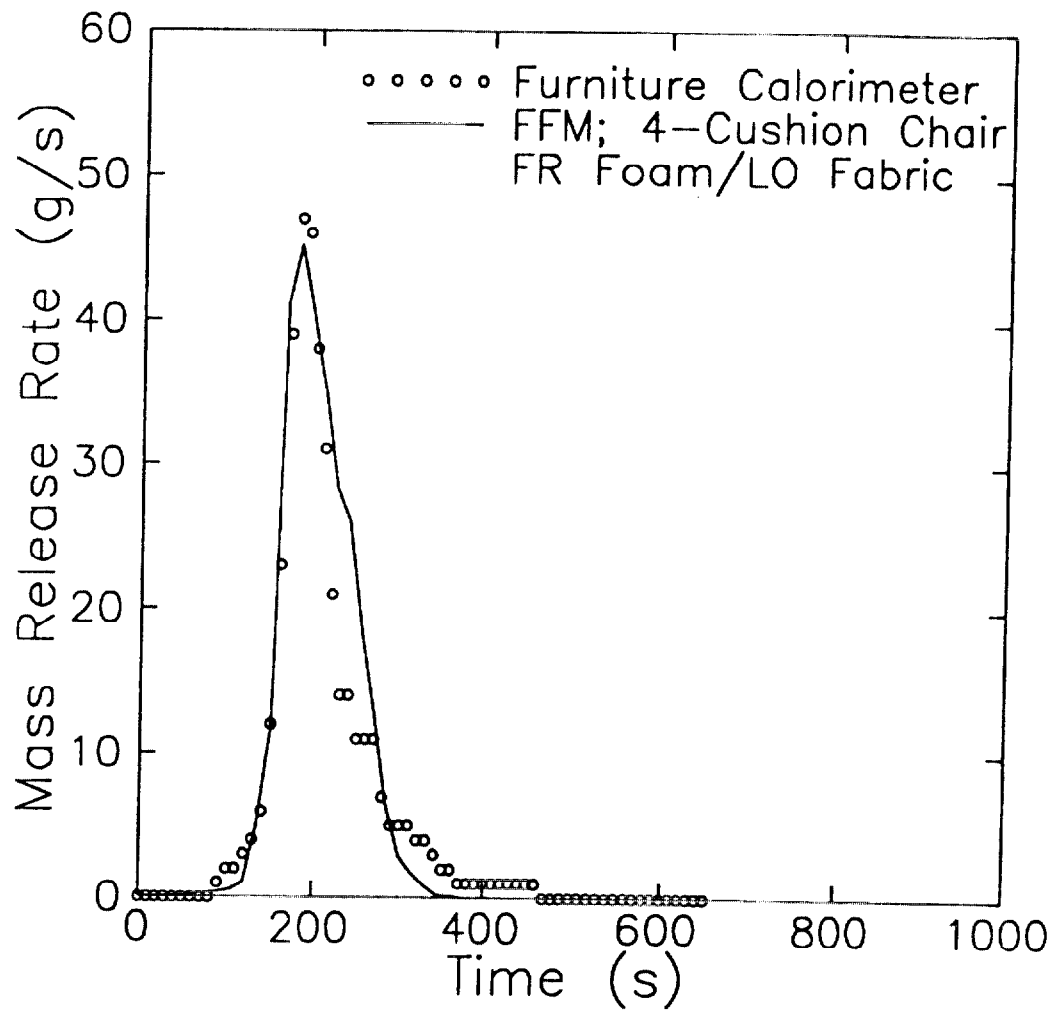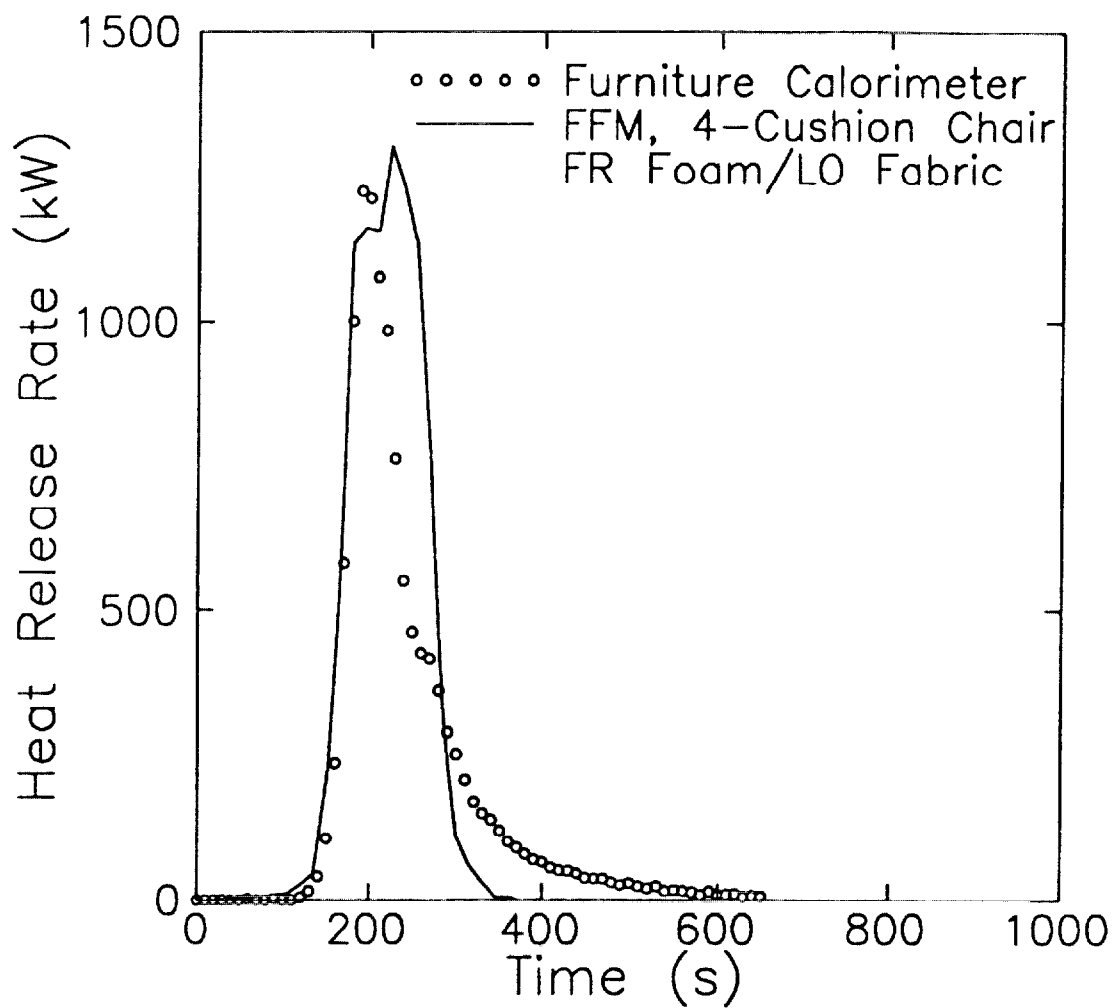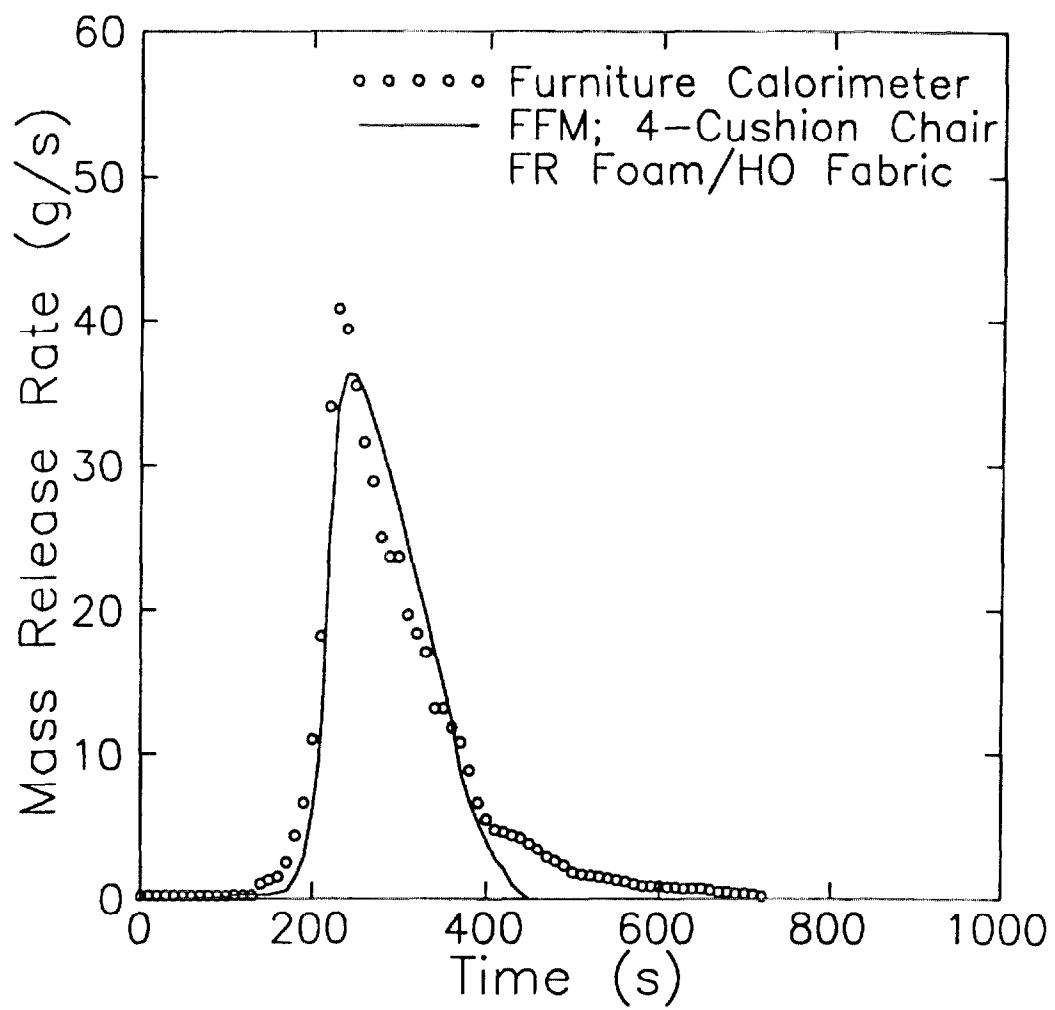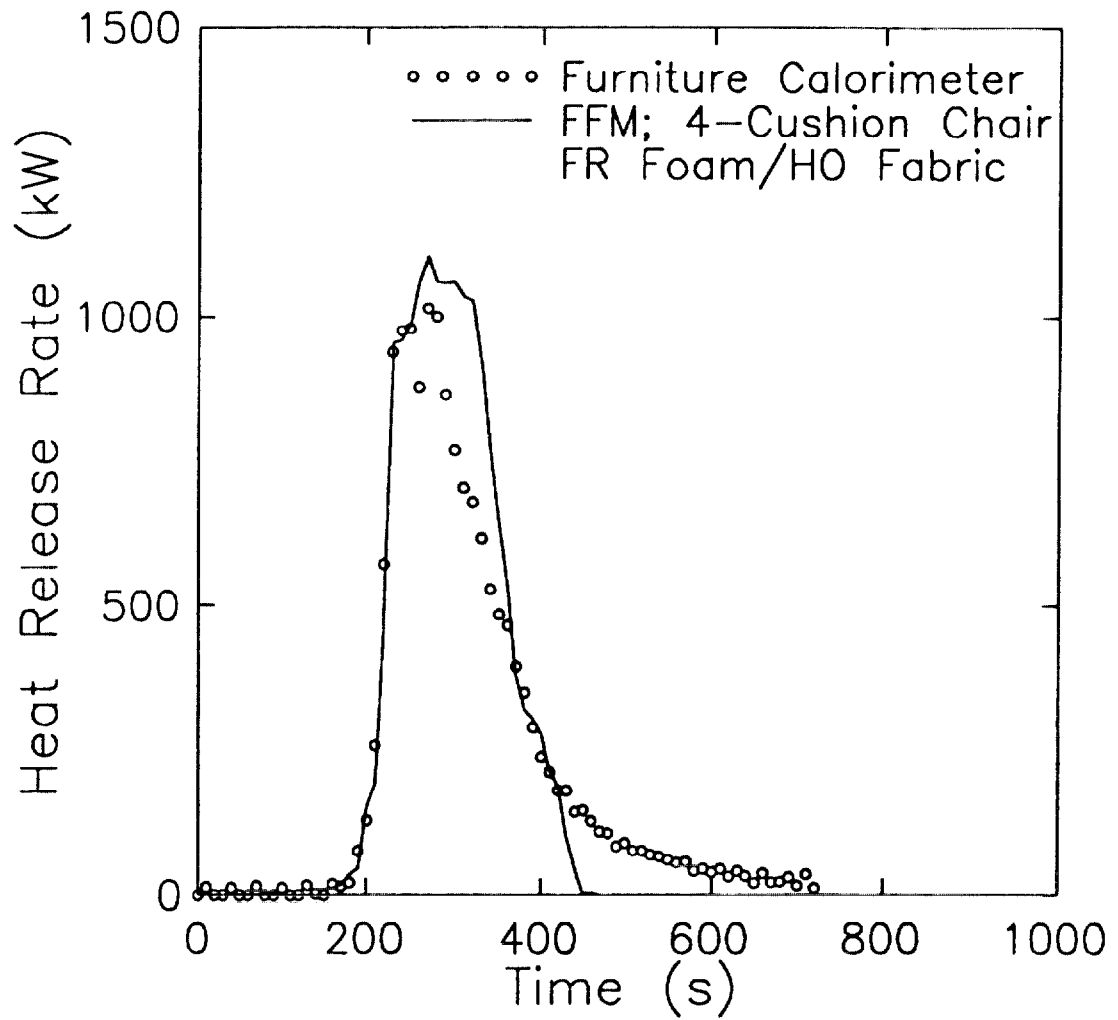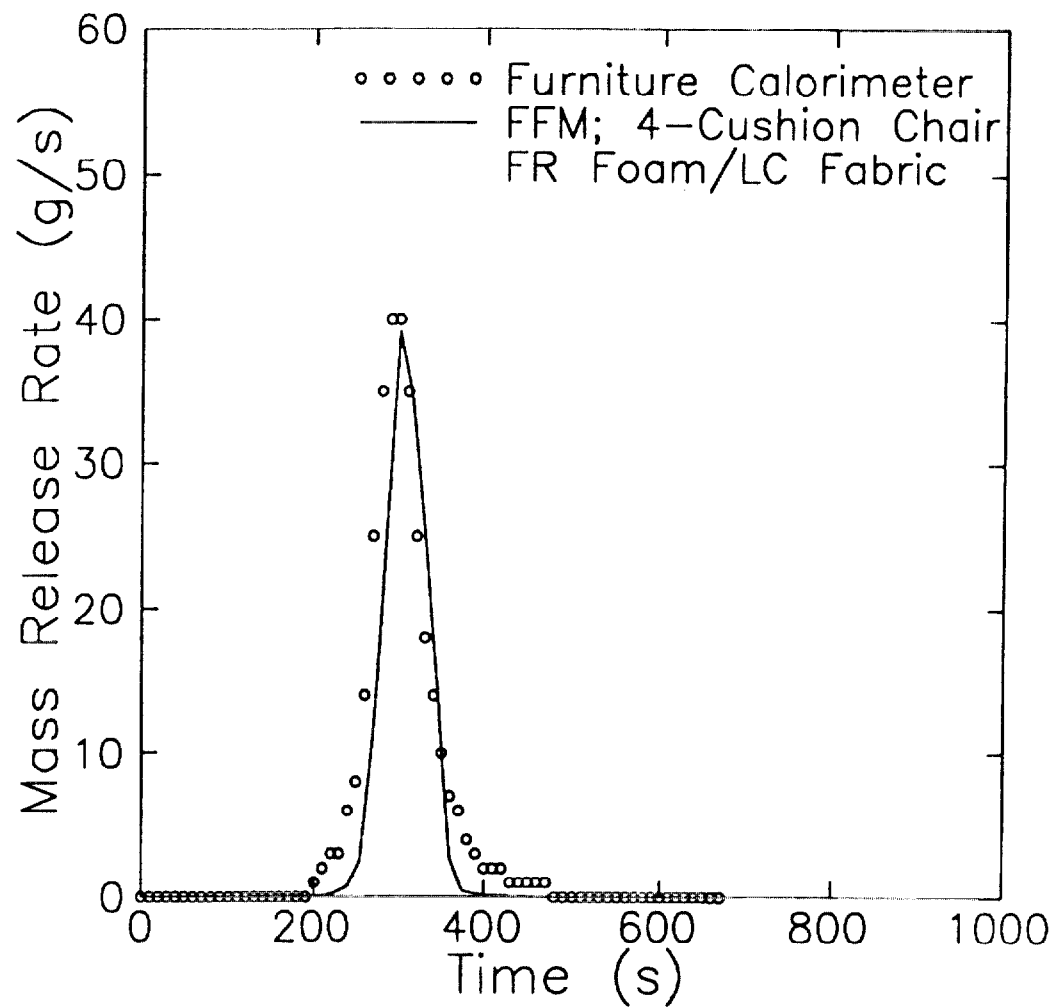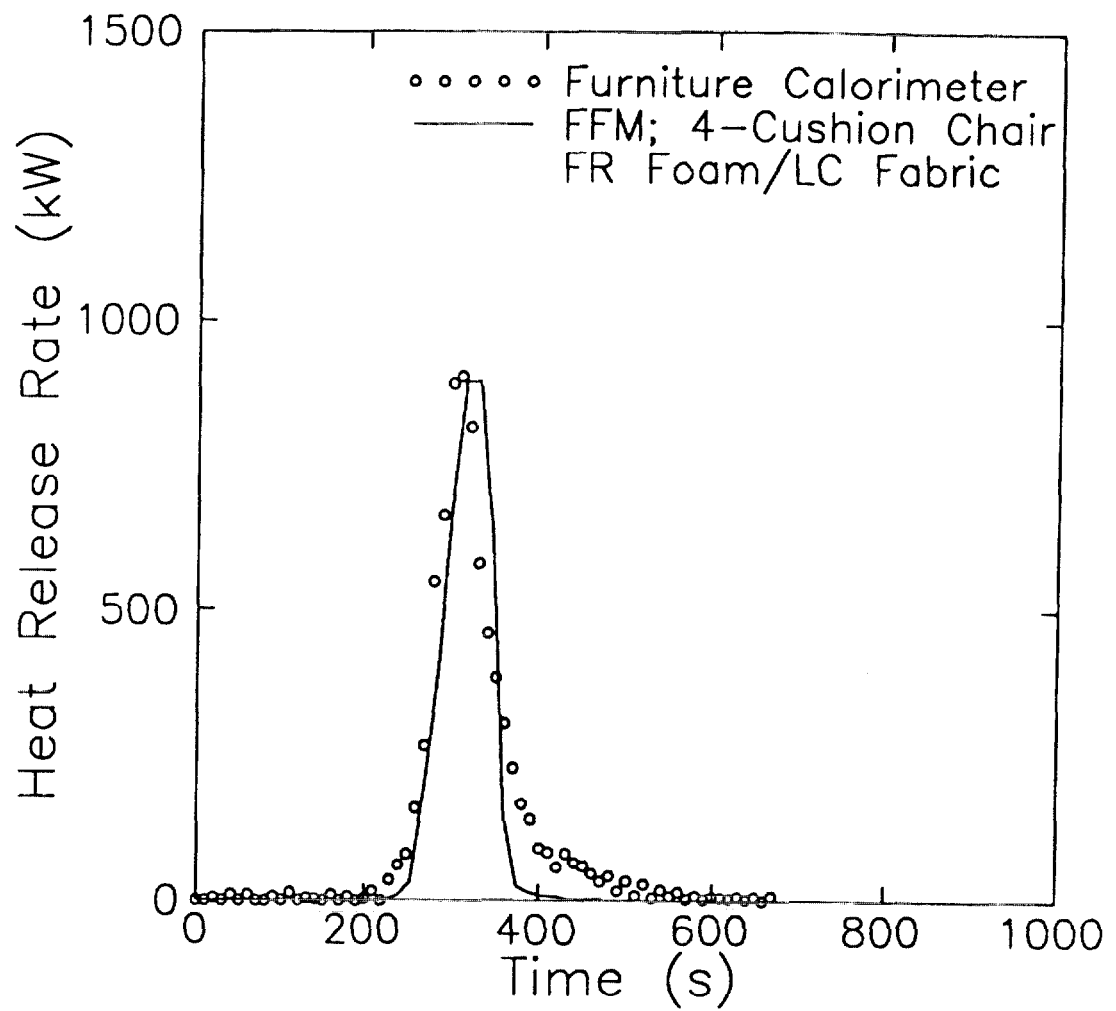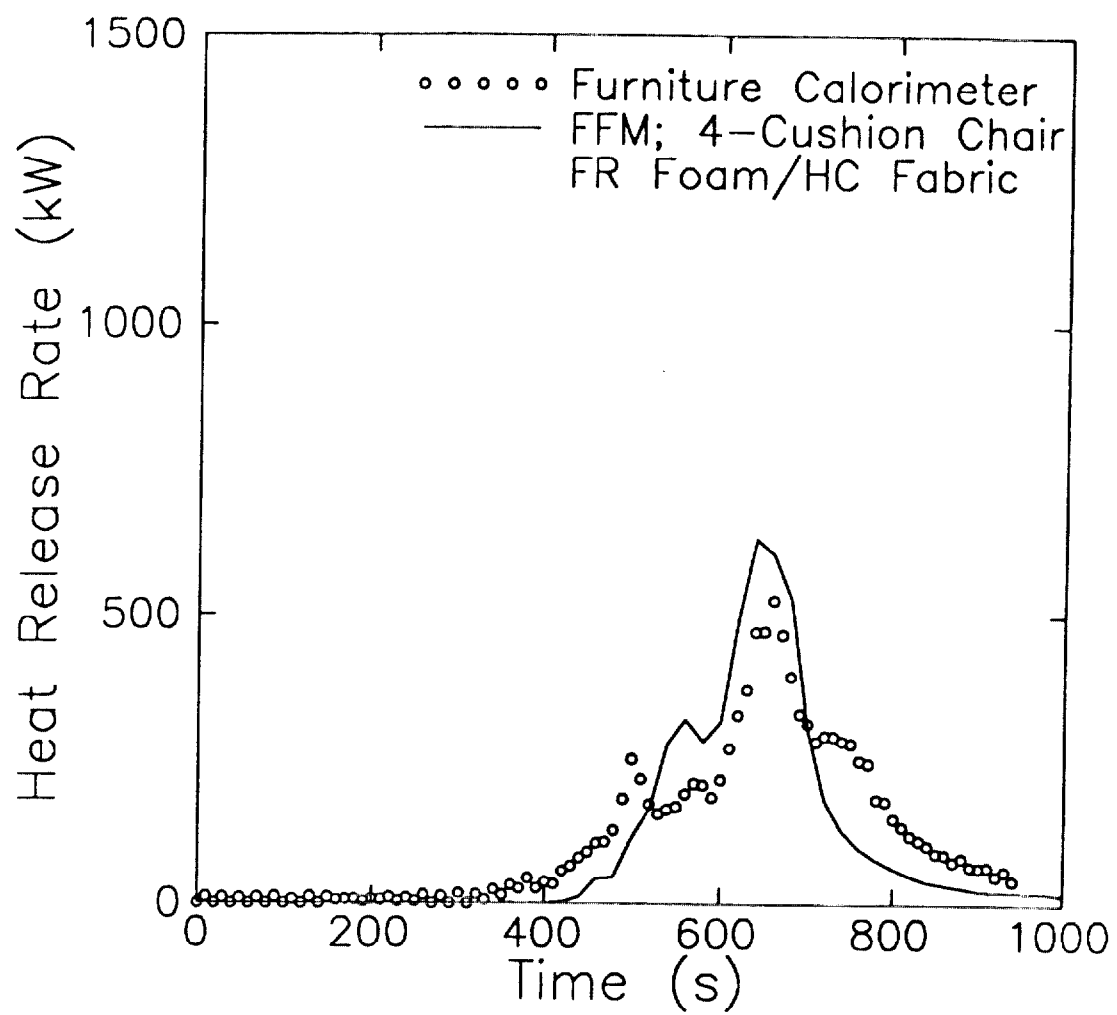Figure A-15. FFM Heat Release Predictions and the Data for FR PU/HC Cushions.
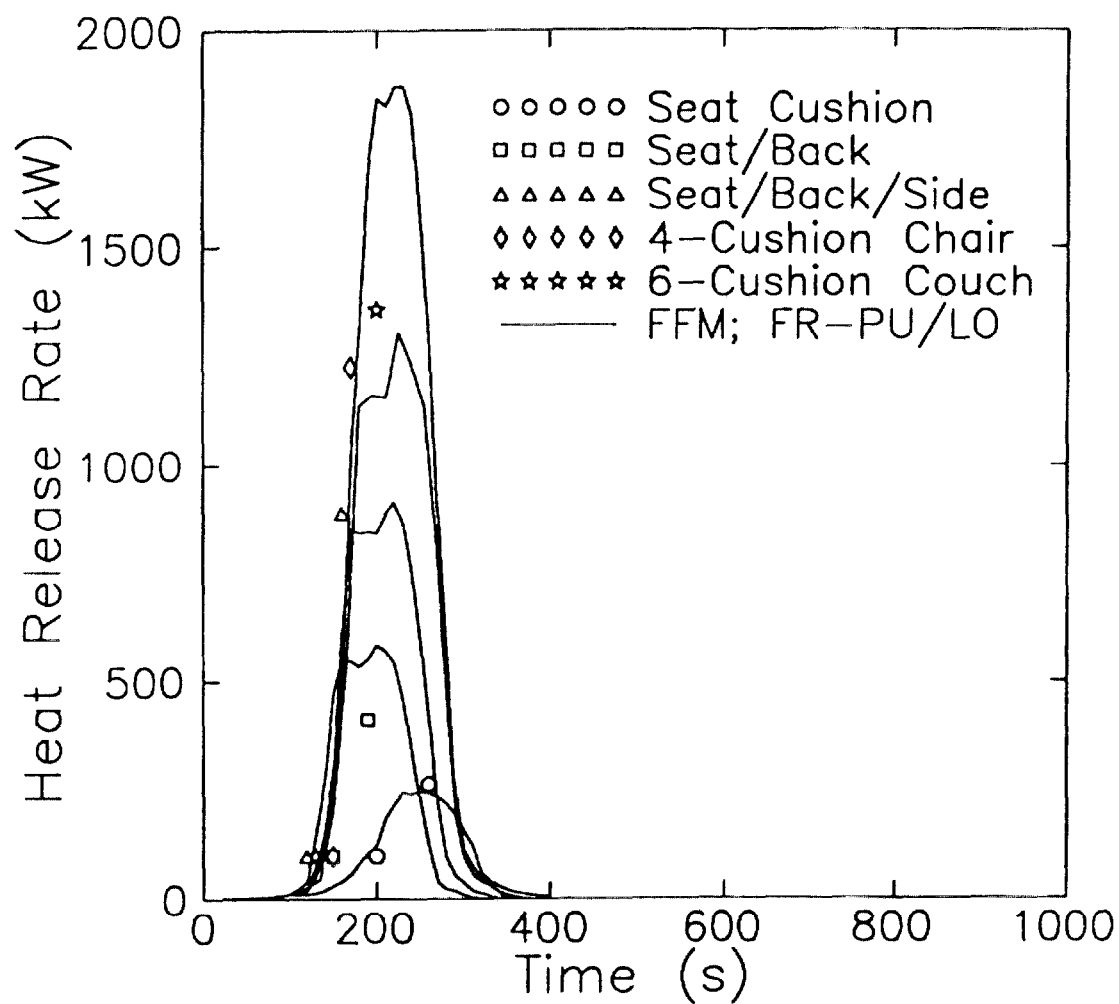
Figure A-16. Effect of Mockup Geometry for the 100 mm thick, FR Foam/LO Fabric Cushions and Comparisons with Data.

very good considering that only one set of scaling constants apply to all five burns. The model captures the inherent difference in the heat release rate growth on a horizontal cushion versus that of a mockup including a backrest. That is, after the horizontal flame spread reaches the back rest, the flame spreads rapidly upward in response to the nearby fire plume. This rapid increase in burn area and flame size will in turn accentuate the flame spreading on the seat because the preheating is enhanced by the flame plume irradiance. The model also captures the effect of the location and number of cushions on the heat release rate history. That is, the peak heat release rate is approximately proportional to the burning area. The burn time also increases with the number of cushions; this is a result of a finite flame spread rate in the first part of the fire growth.

4.3   NFR-PU/LO Cushion With Four Mock-up Variations

The third group of cushions has the same fabric as the second group, but the foam material is not fire retarded. The scaling constants for the NFR-PU/LO cushion in Table 2 were applied successfully to predict full-scale burns for the one-, two-, three-, and four-cushioned mock-ups in the third group. The results (shown in the Figure 17) are similar to those shown in Figure 16. Thus the observations noted for the second group also apply to the third group.

5. SUMMARY AND CONCLUSIONS

This paper describes the successful FFM validation of 13 furniture burn tests performed in the furniture calorimeter. The model validation was based on comparisons of the timing of
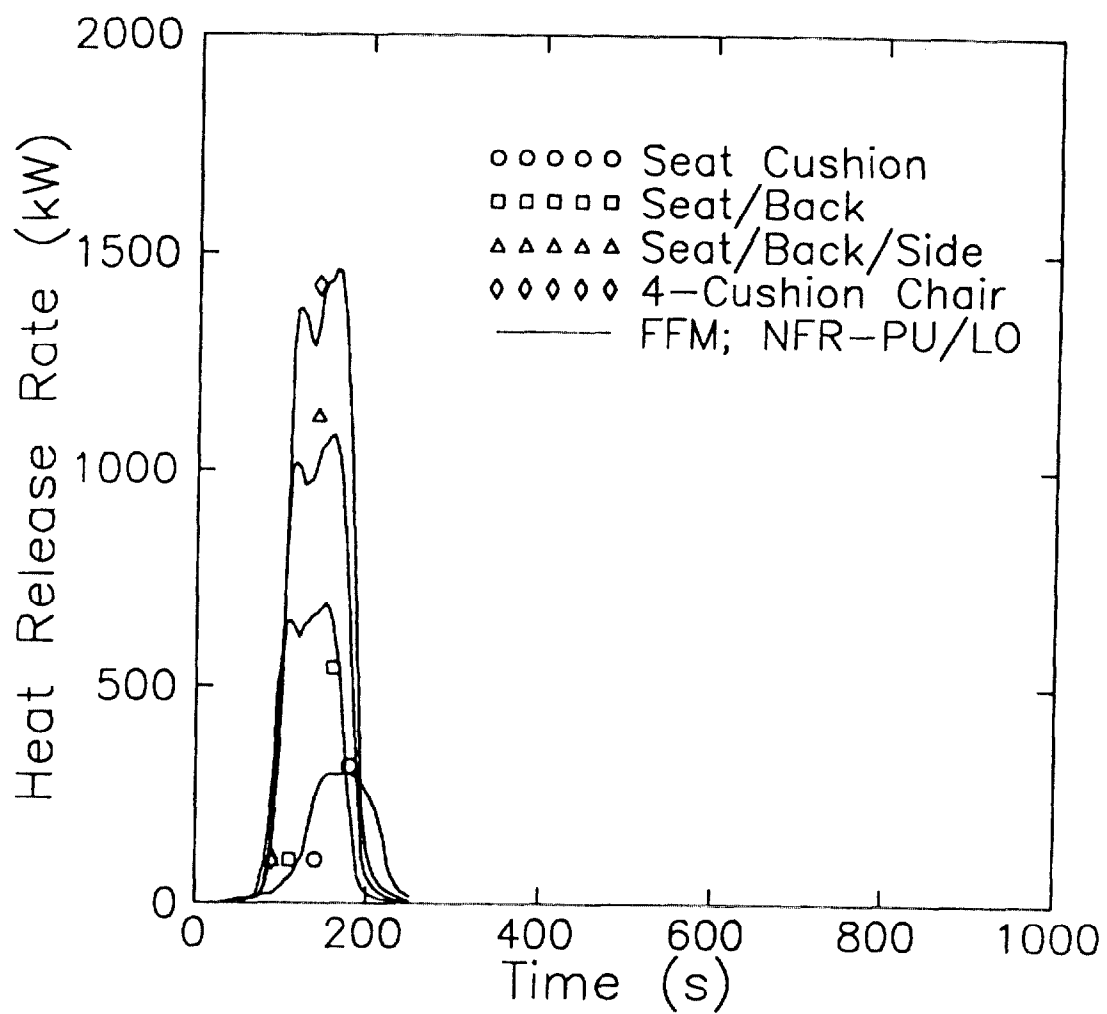
Figure A-17. Effect of Mockup Geometry for the 100 mm thick, NFR Foam/LO Fabric Cushions and Comparisons with Data.

rapid fire growth, peak heat and mass release rates, and upholstered furniture burn time. Additional comparisons of the cushion burn area fractions and the soot extinction areas were not examined in this paper, but can be found for three of the four-cushioned mockups in our earlier work[16]. Slight recalibration of the scaling constants reported in this paper resulted from minor improvements previously made to the FFM code. Thus, the model predictions of the furniture calorimeter data for the four-cushioned mockups for each of the six cushions were shown with good comparisons.

The model was able to capture the scale of the fire due to the changes in the mockup geometry without refining the scaling constants. In particular, the effect of upward flame spread on the backrest accelerates the furniture burn rate. Also, the peak burn rate increased systematically with the total burn area as the number of cushions increased.

Certain features of FFM were crucial in these predictions. The most significant of these features is the re-scaling of the cone calorimeter data for the heat and mass release flux as a function of time to adjust for changing burn history and irradiances. The second most important feature is the calculation of both the conductive and radiative heat flux contributions to ignition and flame spreading. Finally, the soot production was scaled so that thermal radiation from the soot within the diffusion buoyant flame eventually dominated the fire growth process.

Although the bench-scale data was based on similar, but not identical, cushions, the model performed well in predicting the major features of the full-scale burn tests. It was encouraging that the scaling constants did not vary much among the six different fabric/foam cushions

examined.

There are several other applications of the furniture fire model. In our earlier work[2,3], we described the formulations for thermally thick materials, such as PMMA and wood, which should be next candidates for predictions with the current FFM version. Recently, FFM was converted to a fire spread model (FSM) on a single horizontal or vertical panel. FSM could be used to simulate the LIFT apparatus to help resolve current controversy on the dominance of conductive versus radiative heat fluxes on the lateral flame spread rate. In principle, it seems the FSM can be used also to represent flame spreading on a sample in the cone calorimeter[20]. If this simulation is feasible, then the cone calorimeter would be the only bench-scale apparatus we would need to calibrate all scaling constants. If FFM can be proven valid for any scale of fire, it should be possible to consider effects of oxygen vitiation, air pressure, diluents, and air temperature on the flame spread[20]. Such considerations will be important for compartmentation analysis.

6. NOMENCLATURE

A_1 Surface element area (m^2)

C_p Solid fuel heat capacitance (kJ/kg^oK)

d First time stretching constant

e Second time stretching constant

F_{co} Carbon-monoxide mass fraction

F_j Mass fraction of combustion product, j

F_s Soot mass fraction

G Time stretching parameter

h_c Convective heat transfer coefficient ($kW/^oKm^2$)

h_r Radiative linearized heat transfer coefficient ($kW/^oKm^2$)

H_c Carbon heat of combustion (J/g)

H_{co} Carbon monoxide heat of combustion (J/g)

k_s Soot absorption coefficient (m^{-1})

l_f Flame foot length (m)

l_p Plume irradiant surface characteristic length (m)

L Mean beam length of flame volume (m)

m^* Scaled mass release flux (g/J)

$\dot{m}_f''$ Fuel mass release flux (kg/sm^2)

$\dot{m}_j$ Mass rate of combustion product, j (kg/s)

$\dot{q}$ Heat release rate of the flame (kW)

q^* Scaled heat release flux (-)

$\dot{q}''_{cone}$ Measured heat release flux (kW/m^2)

$\dot{q}''_{st}$ Quasi-stoichiometric heat release flux (kW/m^2)

$\dot{Q}''_c$ Convective heat flux (kW/m^2)

$\dot{Q}''_f$ Flame foot conductive heat flux (kW/m^2)

$\dot{Q}''_o$ Scaled heat flux constant (kW/m^2)

$\dot{Q}''_r$ Net surface radiative heat flux (kW/m^2)

$\dot{Q}''_{re}$ External surface radiative heat flux (kW/m^2)

$\dot{Q}''_{rf}$ Fire plume surface radiative heat flux (kW/m^2)

$\dot{Q}''_{ri}$ Imposed surface radiative heat flux (kW/m^2)

$\dot{Q}''_s$ Net surface heat flux (kW/m^2)

s_e Preheat surface length (m)

t Time (s)

t^* Burn history or scaled time (J/m^2)

t_{end} Burn out time for a cone calorimeter sample (s)

T_a Ambient temperature (°K)

T_{eq} Surface equilibrium temperature (°K)

T_{ig} Surface ignition temperature (°K)

T_s Surface preheat temperature (°K)

V_f Flame spread rate (m/s)

δ Solid fuel effective thickness (m)

e_s Surface emissivity

ρ Solid fuel density (kg/m^3)

σ Stefan-Boltzmann constant (kW/$^\circ$K^{4}m^2)

σ_s^e Soot specific extinction area (m^2/kg)

Appendix B

Opposed Flame Spread and Extinction Formulations for Thin and Thick Solid Fuels in Extreme Environments

The following pages represent the second journal article that was submitted in October 1991 to Dr. V. Babrauskas at the National Institute of Standards and Technology for publication in the Fire Safety Journal.

OPPOSED FLAME SPREAD AND EXTINCTION FORMULATIONS FOR THIN AND THICK SOLID FUELS IN EXTREME ENVIRONMENTS

M. A. Dietenberger and L. I. Boehman
Department of Mechanical and Aerospace Engineering
University of Dayton
Dayton, OH 45469

Abstract

This paper compares a recently developed flame spread theory to opposed flame spread rate over thin and thick solid fuels. In the model, the finite fuel slab responds thermally to the external irradiance and conductive heat flux from adjoining flame. Radiant and convective heat losses to the ambience delays the fuel response in reaching a critical surface temperature for ignition. The deRis theory for the spread of laminar diffusion flame is extended to include dependence on the Damköhler number, the lean combustion condition, the radiance of burning region, the elevated referenced air temperature, and the induced flow velocity. The experimental data, as compiled from several sources, represent a large range of environmental parameters such as oxygen mass fraction, opposed flow velocity, pressure, relative gravity, surface inclination, and spread direction. The fitted model parameters are found to remain approximately constant among various experimental configurations for a given fuel. A derived flammability curve is compared to the data for thin fuels.

1. INTRODUCTION

During the past two decades, numerous experiments of opposed flame spread over thin and thick solid fuels have demonstrated the limitations of simple flame spread formulae and detailed numerical models. Usually, the simple formulae, including power law formulations, would fail to correlate new data. Detailed models tend to have unresolved numerical problems or have many model constants that are difficult to obtain. As a result, researchers often resort to normalizing their experimental flame-

spread data and collapsing the results to a single curve.

Typical of such procedures is normalizing the flame spread rate by the deRis formula[1] and plotting it versus a Damköhler number, which is related to finite chemical kinetics[2,3]. This approach often results in empirical relationships that are difficult to extrapolate to other experiments or tend to obscure understanding of the physical processes. On the other hand, when the extreme conditions are examined, such as imposed irradiance[4,5] or flame quenching in microgravity[6], rescaling the data is problematic. Although the detailed numerical models are beginning to produce successful results[7,8], their usefulness is limited to gaining a fundamental understanding of the flame spread process. That is, they use large computer and analysis resources, which make them impractical for routine analysis of fire scenarios involving composite materials.

This paper describes a successful approach which generalizes the existing flame spread formulation to new physical processes, and uses empirical functions only to represent specific physical phenomena. With only a few model constants, the salient features of the experimental flame spread data is reproduced, even for extreme conditions. The resulting equations are fitted to the published data on the flame spread rate over paper and PMMA versus the wide varying environments. These variations include oxygen mass fractions, forced flow, gravity, pressure, and irradiance. The continuous decrease in the flame spread rate leading to blowoff is modeled by reducing the flame temperature with a decreasing Damköhler number. Flame quenching is likewise related to a less dominating flame conductive heat flux in comparison with the surface radiative heat loss. However, flame extinction occurs at a critical point in which flame spreading can cease discontinuously. Consequently, a flammability curve could be constructed and compared with the extinction data.

2.   MATHEMATICAL MODEL

The physical analysis of the ignition and flame spread follows a three-step process. The first step analyzes the fuel's thermal response to prescribed heating up to the firepoint. The second step analyzes the prescribed heating due to the attached diffusion flame by using the deRis formulation. In the third step, the properties and physics of the anchored flame are modified to account for additional physical phenomena.

The thermal properties of the fuel are surface thermal thickness, bulk thermal inertia, and surface ignition temperature. A detailed theory[9], which includes finite-rate chemical kinetics, demonstrated that the pyrolysis (or vaporization) temperature is constant during vigorous pyrolysis for many situations. With piloted ignition, the surface ignition temperature can be identified with the pyrolysis temperature. These basic properties are also a good approximation for composite materials because the thermal depth during flame spreading is probably no more than the first two layers.

Many ignition or flame spreading experiments impose a constant irradiance at a spot along with a convective/radiative surface cooling (which is linearized as a function of surface temperature). The conductive heat flux distribution from the attached flame is modeled as a rapidly decreasing exponential function of surface distance in a geometry moving at the flame spread rate, V_f. The details of transverse heat conduction from the flame through the gaseous and solid phases are assumed implicit in the heat flux distribution. In the present formulation, the fuel thermal response to the flame heat flux is decoupled (to a good approximation) from the response to imposed irradiance.

The analytic thermal response solution leading to piloted ignition (as derived in Reference 10) is:

$$T_{ig} = T_e + \cfrac{\dot{q}_{cf}}{h_{ig} + \sqrt{\dfrac{V_f}{\delta_f}\rho C_p \lambda + \dfrac{V_f}{\delta_f}\rho_o C_{p_o}\delta_o}} \qquad , \tag{1}$$

where the preheat temperature, T_e, is given by one of following options.

Option 1, no bulk layer, $\rho C_p \lambda = 0$:

$$T_e = T_a + \frac{\dot{q}_{re}}{h_{eq}}\left\{1 - \exp\left(\frac{-h_{eq}\,t_e}{\rho_o C_{p_o}\delta_o}\right)\right\} \qquad . \tag{2}$$

Option 2, no top thin layer, $\rho_o C_{p_o}\delta_o = 0$:

$$T_e = T_a + \frac{\dot{q}_{re}}{h_{eq}}\,G\!\left(\frac{h_{eq}\sqrt{t_e}}{\sqrt{\rho C_p \lambda}}\right) \qquad . \tag{3}$$

Option 3, both layers, $\rho C_p \lambda$ and $\rho_o C_{p_o}\delta_o > 0$:

$$T_e = T_a + \frac{\dot{q}_{re}}{h_{eq}}\left\{\frac{b^+\,G(b^-\sqrt{t_e}) - b^-\,G(b^+\sqrt{t_e})}{b^+ - b^-}\right\} \qquad . \tag{4}$$

The auxiliary relationships are:

$$G(x) = 1 - \exp(x^2)\,erfc(x) \tag{5}$$

$$b^{\pm} = \frac{\sqrt{\rho C_p \lambda} \pm \sqrt{\rho C_p \lambda - 4h_{eq}\,\rho_o C_{p_o}\delta_o}}{2\,\rho_o C_{p_o}\delta_o} \tag{6}$$

$$h_{ig} = h_c + \varepsilon_s \sigma \ (T_{ig}^4 - T_a^4) \ / \ (T_{ig} - T_e)$$ (7)

$$h_{eq} = h_{conv} + \varepsilon_s \sigma \ (T_{eq}^4 - T_a^4)/(T_{eq} - T_a)$$ (8)

Note the fuel preheat temperature, T_e, is the equilibrium temperature, T_{eq}, at infinite value of time. The preheat time, t_e, is also the time to ignition. Setting the flame-foot heat flux, $\dot{q}_{cf}$, in Eq. (1) to zero provides the above relationships for use with the piloted ignition data. Since Eq. (1) is exact (at least at infinite time), V_f can have any positive value. However, as will be shown later and contrary to expectations, flame extinction is not necessarily defined by setting V_f to zero in Eq. (1). We note that Eqs. (2) and (3) are merely special cases of Eq. (4), which in general is a complex valued function. This is because Eq. (6) can have complex values, particularly for materials with a heavy thin covering over a light thick cushion. This poses minimal difficulty for computer analysis since an accurate algorithm for Eq. (5) with complex variables was implemented on a personal computer[10]. A temperature increment due to irradiant flux from the advancing flame could have been added to the right side of Eq. (1) for unique opposed-flow geometries. (That, however, is the subject of another paper.) This paper focuses on developing relationships for the parameters in Eq. (1) associated with the attached diffusion flame and a premixed flame foot in opposed flow.

The analysis of a laminar diffusion flame spreading in opposed flow over thin or thick fuel begins with the classical infinite-kinetics, Oseen flow solution of deRis[1]. If the imposed irradiance and surface emissivity in the above equations are set to zero, then a correspondence with deRis formulae results in defining $\dot{q}_{cf}$, h_c, and the exponential decay (characteristic) length, δ_f, as

$$\dot{q}_{cf} = h_c \, (T_f - T_s) \qquad (9)$$

$$h_c = \sqrt{2} \; \lambda_a \, / \, \delta_f \qquad (10)$$

$$\delta_f = 2 \; \lambda_a \, / \, (\rho_a C_{pa} V_a) \qquad (11)$$

Although deRis did not analyze a composite fuel with both thin and thick layers, Eqs. (9) through (11) involve only parameters associated with the flame and its boundaries, and thus are extended here to composite fuels. The diffusion-flame parameters (T_f, λ_a, ρ_a, C_{pa}, and V_a) are further analyzed to account for lean combustion, finite kinetics, net radiative heat flux on the burning surface, variable gas properties, and induced buoyant flow. The phenomena of a lean, premixed flame foot and reactants leaking through the diffusional flame sheet (as observed in Refs. 2 and 3) are assumed to effectively reduce the adiabatic flame temperature

$$T_{f_{eff}} = T_{ig} + \cfrac{(T_a - T_{ig}) + \cfrac{Y_{ox_a}}{\phi \; C_{pa}}(\Delta H_c - \cfrac{L_{eff}}{Y_{fR}})}{1 + \cfrac{Y_{ox_a}}{\phi \; Y_{fR}}} \qquad (12)$$

$$T_f = T_{f_{eff}} - (C_o + \cfrac{C_1}{T_{f_{ad}} - T_{ig}}) \sqrt{\cfrac{C_{pa}V_a^2}{Y_{ox_a}\lambda_a}} \qquad (13)$$

where $T_{f_{ad}} = T_{f_{eff}}$ for $L_{eff} = L$. Eq. (12) is the classical expression for the diffusion-flame temperature under infinite kinetics and stoichiometric conditions[1]. The blowing and diffusion of the pyrolized fuel is included in Eq. (12) with the assumption that the Lewis number is unity. The conservation equations for specie mass and heat transfer considered by deRis explicitly include the nonlinear reaction kinetic terms. The Zeldovich transformation applied by deRis merely make the kinetic terms disappear, although the transformed conservation equations are valid for any chemical kinetic rates.

The assumption of infinite kinetics was invoked to be consistent with the heat and mass transfer boundary conditions applied to the interface of the solid fuel and gas.

We note that less restrictive assumptions can be made that would also satisfy the same boundary conditions to a good approximation. For example, one can propose the flame sheet near its foot burns at some lean flammable state with rapid kinetics[2]. With a detailed numerical model[9] that includes finite kinetics, a low-reactivity zone in the flame foot was observed, even with fast kinetics. There is then residual oxygen gas that can flow underneath the diffusion-flame sheet via the lean flame foot and not react with the much cooler zone of gaseous fuel. Indeed, there is a range of premixed oxygen/fuel ratios that will not spontaneously ignite at some range of temperatures higher than the vaporization state. Therefore, the residual oxygen can be treated as one of the inert gas components in the deRis model. In another example, a high flow rate can smear the flame sheet at distances far from the surface; however, a sharp flame front is maintained near the fuel surface because of the much lower flow velocity near the surface. Although the flame sheet is being smeared, it is still sharp enough to retain the laminar diffusion-flame features. A significant reduction in the adiabatic flame temperature can also be expected if the heat capacity within the flame zone can be as much as twice that in ambient air. These realistic structures of the flame sheet are approximated in this paper by an effective lean value for the oxygen-to-fuel-mass ratio.

The term within the square root of Eq. (13) is proportional to the inverse of the Damköhler number. This number is conveniently thought of as the ratio of flow time to chemical time in the flame[2,3,6]. The leaking of reactants through the flame sheet at high opposed flow velocities, clearly indicates relatively slow reaction rates at low Damköhler numbers. Also, the low reactivity zone in the flame foot becomes enlarged as extinction is approached[9]. Simultaneously, the diffusion flame front

was functionally related to the flame temperature. However, the flame structure actually consists of both diffused and premixed combustion regions. Therefore, the deRis solution is valid at a relatively high Damköhler number and the premixed flame-spread solution would be valid at relatively low Damköhler number. Note that in either limit the flame front remains attached to the vigorous pyrolysis zone. Our description of flame spread at the intermediate values of the Damköhler number is to retain the deRis formulation, but reduce the adiabatic flame temperature as a simple function of the Damköhler number, as in Eq. (13).

The effective heat of pyrolysis, L_{eff}, includes the effect of the net surface radiative flux of burning surfaces. It is expressed as

$$L_{eff} = \frac{L \ h_c(T_f - T_{ig})}{h_c(T_f - T_{ig}) - \varepsilon_s \sigma(T_{ig}^4 - T_a^4) + \dot{q}_{re}} \tag{14}$$

The flame-front gaseous zone is assumed to be optically thin in opposed flow so that the surface radiative fluxes are not attenuated in passage through the flame-foot zone. Thus, the surface radiative cooling effectively increases the heat of pyrolysis, which in turn decreases the flame temperature. Ultimately, the surface radiative cooling leads to quenching at some low opposing-flow speed, low oxygen level, low pressure, or low Damköhler number. On the other hand, the effect of imposed irradiance decreases L_{eff} and increases T_θ; thus widens the boundaries of flame quenching and increases the flame spread rate. If the surface radiative cooling of the burning surfaces were ignored, setting V_f to zero in Eq. (1) would define the flammability curve. However, Eq. (14) introduces additional constraints on the flame temperature that will not allow V_f to continuously reach zero at the extreme limits. This occurs because, at some small finite values of V_f, the partial derivative of V_f with respect to the opposed flow velocity, V_a, is infinite at both lower and upper limits (quenching and blowoff). Further discussion on this definition of the flammability curve is provided in Attachment 1.

As a result, the flame front moves erratically and slowly near its extinction limit because the random oscillations in the environmental conditions are amplified in the flame spread rate. The flame only becomes blown off when the heat of pyrolysis on the burning surface is no longer supported by heating from the flame.

The above description of flame extinction is strikingly similar to the numerical analysis[12] for the extinction of a buoyant laminar diffusion flame on a vertically thick PMMA slab. In this analysis, the gas is optically thin to both external and wall radiation, and gas phase radiation to the wall may be neglected. On the other hand, the heat losses due to fuel surface radiation are sufficient for extinction even in the limits of the infinite chemical reaction rate. The flame sheet temperature was lowered when considering incomplete combustion and finite chemical kinetics. As external irradiance was increased, (1) the boundary layer was thickened, (2) flame temperature was modestly increased, and (3) the temperature gradient at the surface still decreased. Thus, the boundaries of extinction were widened. Eqs. (13) and (14) provide the correct qualitative features that should be quantitatively verified.

The thermal properties of the flow will vary with the temperature and composition of the fluid, particularly in the vicinity of the flame front. The reference temperature used to evaluate C_{pa}, ρ_a, and λ_a is empirically modeled as

$$T_{ref} = \max(T_a \, , \, a + b \, T_{fad})\tag{15}$$

Since the oxygen and nitrogen gases have values of thermal properties within a few percent of each other, the corrections for the changing composition of the air would not necessarily improve model predictions. If the nitrogen gas component was replaced by other diluent gases (such as carbon dioxide, argon, neon, or helium), the compositional corrections to the flow thermal properties would be needed.

The opposed flow velocity is taken as the sum of the flame spread rate, forced flow rate, and

buoyant flow rate as

$$V_a = V_f + V_c + \sqrt{2 \, C^* \, (T_f / T_a - 1) \, \delta_f \, g \, \cos(\theta)}$$ (16)

C^* is an empirical dimensionless constant introduced for scaling the buoyant velocity. The above form

for the buoyant velocity was derived by assuming that a buoyant packet of fluid was exposed to an

exponentially rising gaseous temperature from the ambient to the flame zone[10]. Thus, the exponential

decay length, δ_f, defines the length scale in which the buoyant acceleration of the fluid packet occurs.

The effect of viscous resistance (or Prandtl number) and the flame foot geometry are assumed implicit

in the constant, C^*. The buoyant velocity may not correspond exactly to a measured value because it

is defined to be analogous to the Oseen forced-velocity profile.

Calibration of the model constants is made manageable by using already measured values, and

by organizing crucial experiments to systematically derive the constants. The given values of model

constants are: $\epsilon_s = 1$, $T_a = 300\,^\circ K$, $g = 980$ cm/s^2, and $Y_{fr} = 1$. The heat of combustion, ΔH_c,

and the heat of pyrolysis, L, are usually available from the cone calorimeter or other apparatus. The

fuel thermal parameters of ignition temperature, thermal thickness, and thermal inertia can be derived

from the piloted ignition data. There remain six empirical constants (ϕ, C_o, C_1, a, b, and C^*) which

must be fitted to the flame spread data for extreme environments. Section 3 describes the comparison

of model predictions with flame-spread experiments on papers/cards; Section 4 does the same for the

thick PMMA slabs.

3. COMPARISON WITH THIN FUEL EXPERIMENTAL DATA

Since all thin fuels for the experiments considered here are either papers or cards, all the model constants (except thermal thickness) are the same for all the data. Some constants for the thin fuels have been measured (e.g., $T_{ig} = 618\,^{\circ}K$, $\Delta H_c = 16737$ J/g, and $L = 1160$ J/g)[2-6]. The forced flow velocity and oxygen mass fraction parameters were varied in the experiments reported in Reference 2; however, there were no irradiance and negligible buoyant-flow velocity. Using a personal computer, the model prediction of the data as shown in Figure 1 correspond to the model constants:

$\rho_o C_{p_o} \delta_o = 0.007$ J/cm^{2}K (12% less than reported[2]),

$\phi = 2$,

$C_o = 0.019\,^{\circ}K(gs/cm^3)^{1/2}$,

$C_1 = 31.6\,^{\circ}K^2(gs/cm^3)^{1/2}$,

$a = 9.2\,^{\circ}K$, and

$b = 0.092$.

Further variation on these constants would have fit the data slightly better, but would have made it somewhat worse for the other data considered. Note that if Eqs. (12) and (15) had not been modified for finite kinetics and changing gas properties, the predicted flame spread rate would not have decreased with flow speed and would be much too high as a function of oxygen concentration. Had the data in Figure 1 been plotted on a linear scale rather than the log scale, we would observe that the conditions for infinite chemical kinetics can only be obtained at the lowest flow velocity. Likewise, flame extinction at high flow velocity is not obvious in the data on a linear scale because nowhere does the flame spread rate suddenly decrease with the flow velocity. Yet, this was the set of data used to define blowoff limits in Reference 6 (and also in this paper for a lack of better data).
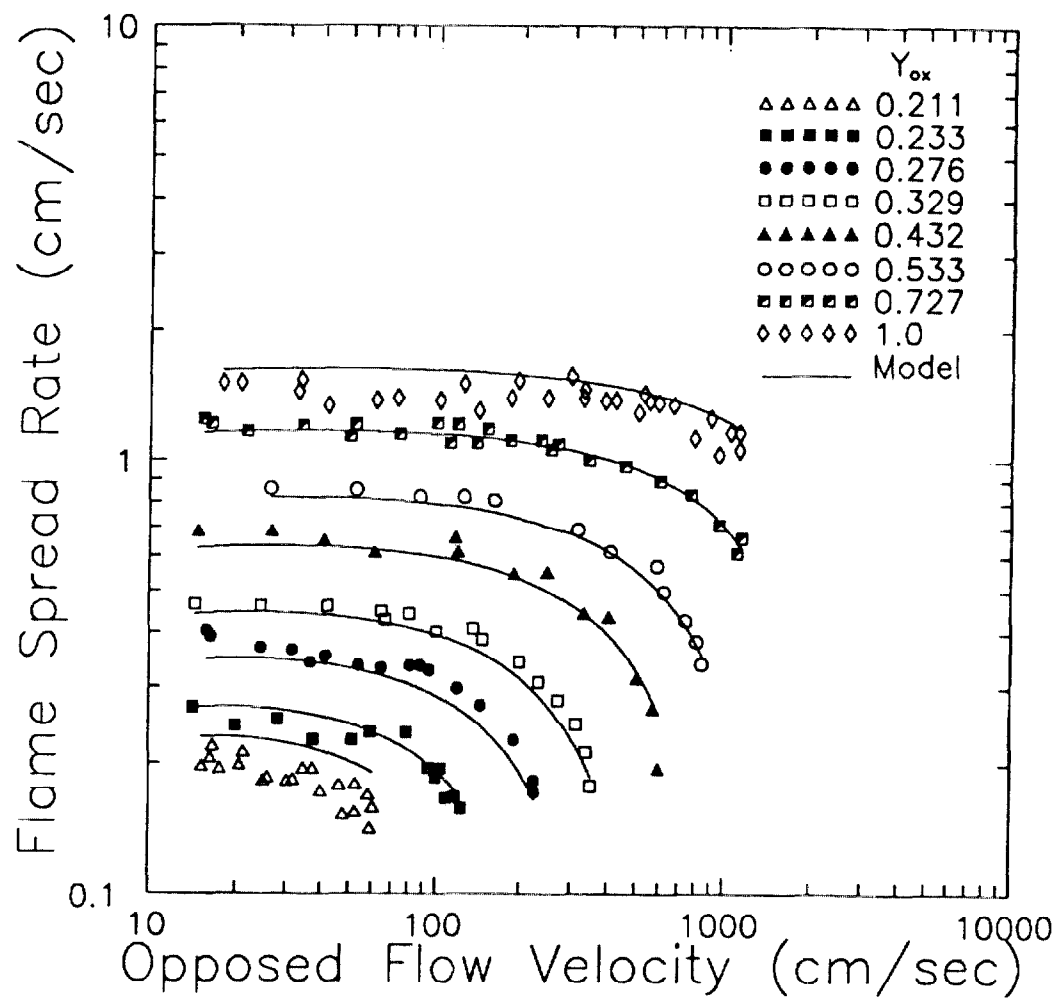
Figure B-1.   Model Predictions of the Flame Spread Rate Data from Reference 2 as a Function of Opposed Flow Velocity and Oxygen Mass Fraction for the Paper.

The tangential gravity, pressure, oxygen mass fraction, and fuel thermal thickness parameters were varied in the experiments reported in Reference 3. There were no forced flow or irradiance. The excellent prediction of the experimental data in Figure 2 required calibration of the induced flow constant, $C^* = 110$, while other constants are as listed above. The thermal thicknesses for the paper tape (0.0036 J/cm²K) and the index cards (0.0093 J/cm²K) were as reported[3]. These results demonstrate the unique and salient features of the flame spread model. The flame spread rate dependence on thermal thickness results from the single term in Eq. (1) ($\dot{q}_{r\theta}$ is zero in Eq. (2)). The flame spread rate dependence on pressure is the result of air density in Eq. (11). The dependency of the flame spread rate on oxygen mass fraction occurs only in the flame temperature equations, and the effects of gravitational acceleration are isolated through Eq. (16). The flame spread rate decreasing with gravity and increasing with pressure results from the unique incorporation of the Damköhler number into the flame temperature equation. In a normal 1-g air environment, the derived buoyant air speed (94 cm/s) and flame temperature (1450 °K) are both reasonable[13].

The importance of surface radiative fluxes through Eqs. (1), (2), and (14) is demonstrated with more data involving opposed buoyant flow (shown in Figures 3 through 6). The flame spread for on the top of paper (inclination angle between 0 and 90 degrees) and with three irradiance levels[4], compare very well with the model predictions in Figure 3 using the model constants already calibrated above. The thermal thickness (0.03 J/cm²K) was as reported[4]. Surface absorptance was set to 0.4 because the paper (α-cellulose sheet) was irradiated only on one side. The preheat temperature was essentially the same as the equilibrium temperature, except at high irradiances. The flame spread rate increases as the tangential gravity is reduced below unity down to a value of 0.005 g's. At this nearly horizontal surface, the flame spread rate peaks for the buoyant speed of around 18 cm/s. This is in agreement with the data in Reference 14, which are for low, forced, opposed-flow velocity in microgravity. The accelerated
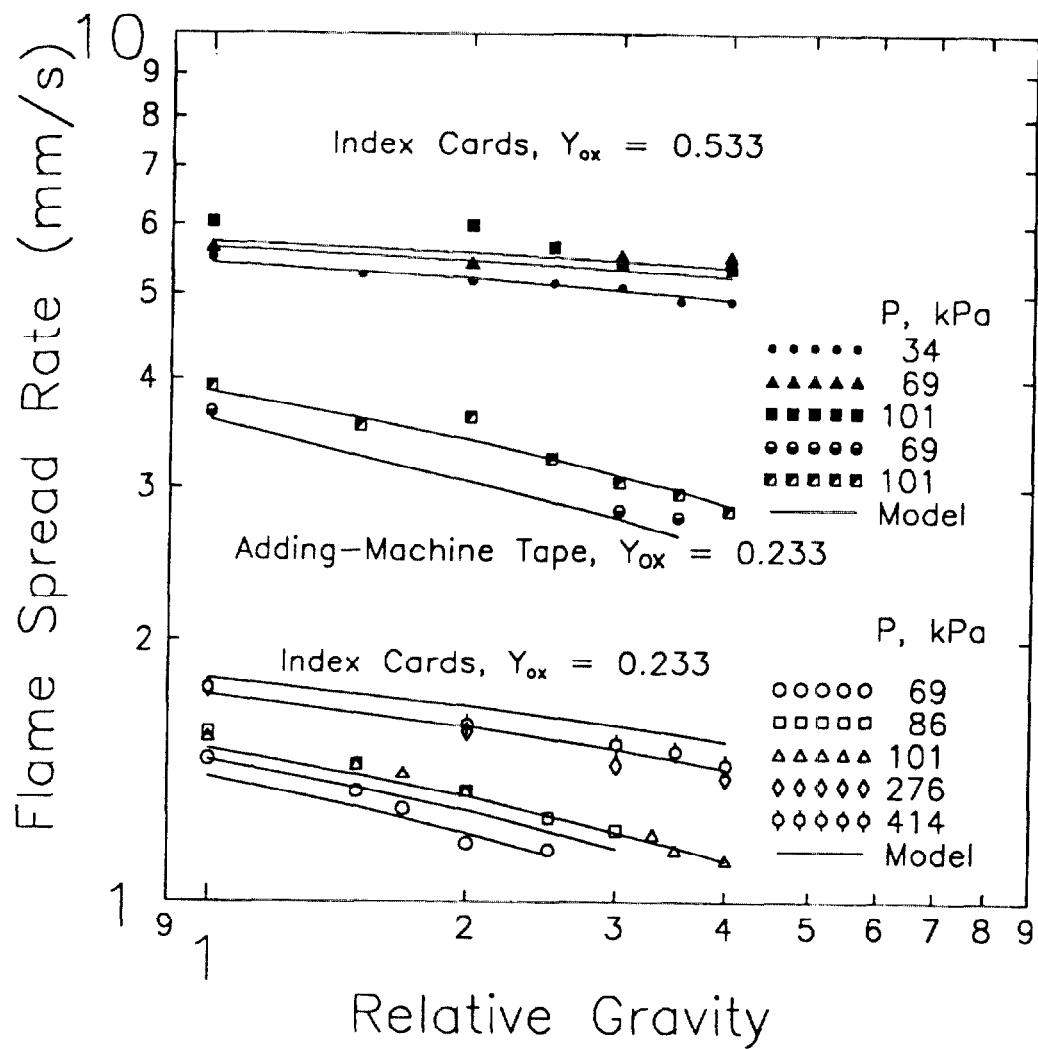
Figure B-2.   Model Predictions of the Flame Spread Rate Data from Reference 3 as a Function of Relative Gravity, Pressure, Oxygen Mass Fraction, and Thermal Thickness.
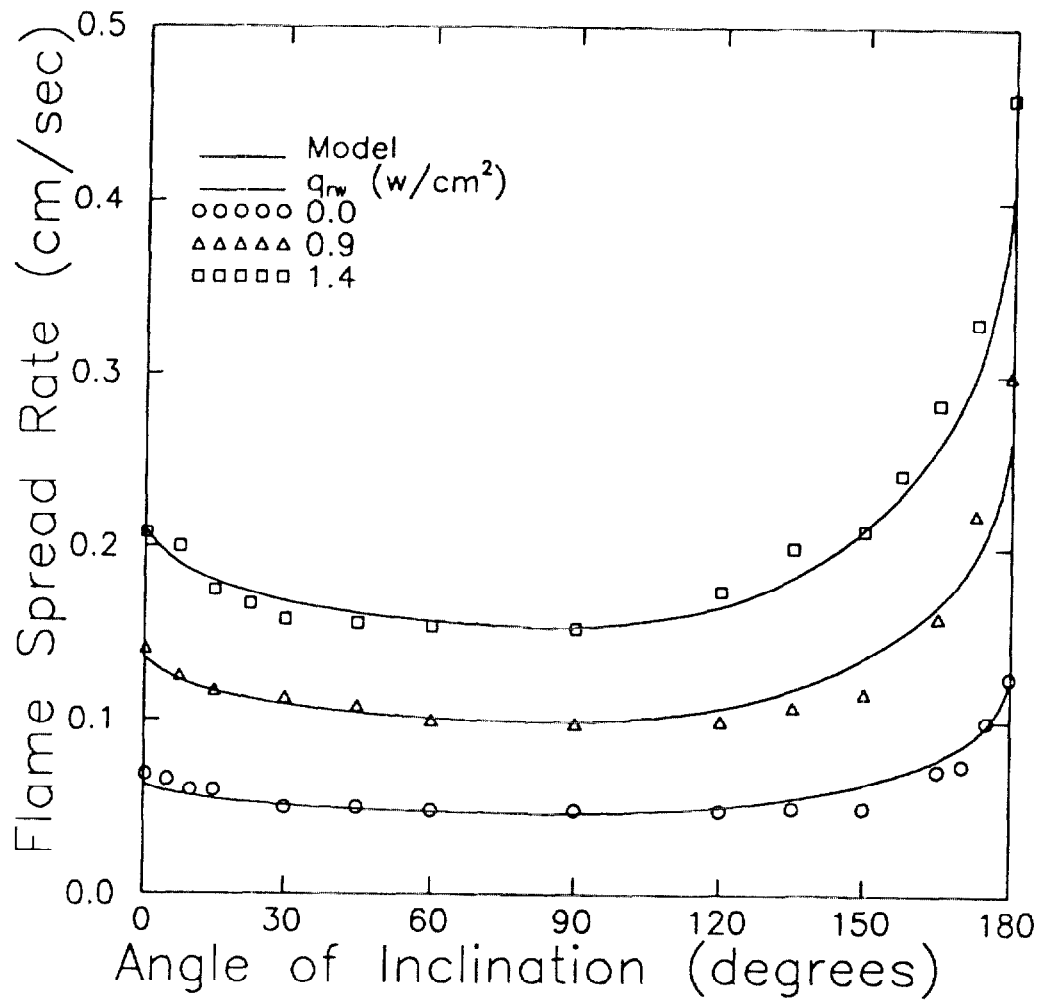
Figure B-3.   Model Predictions of the Downward Flame Spread Rate Data from Reference 4 as a Function of Inclination Angle and External Irradiances for the Paper Tape.
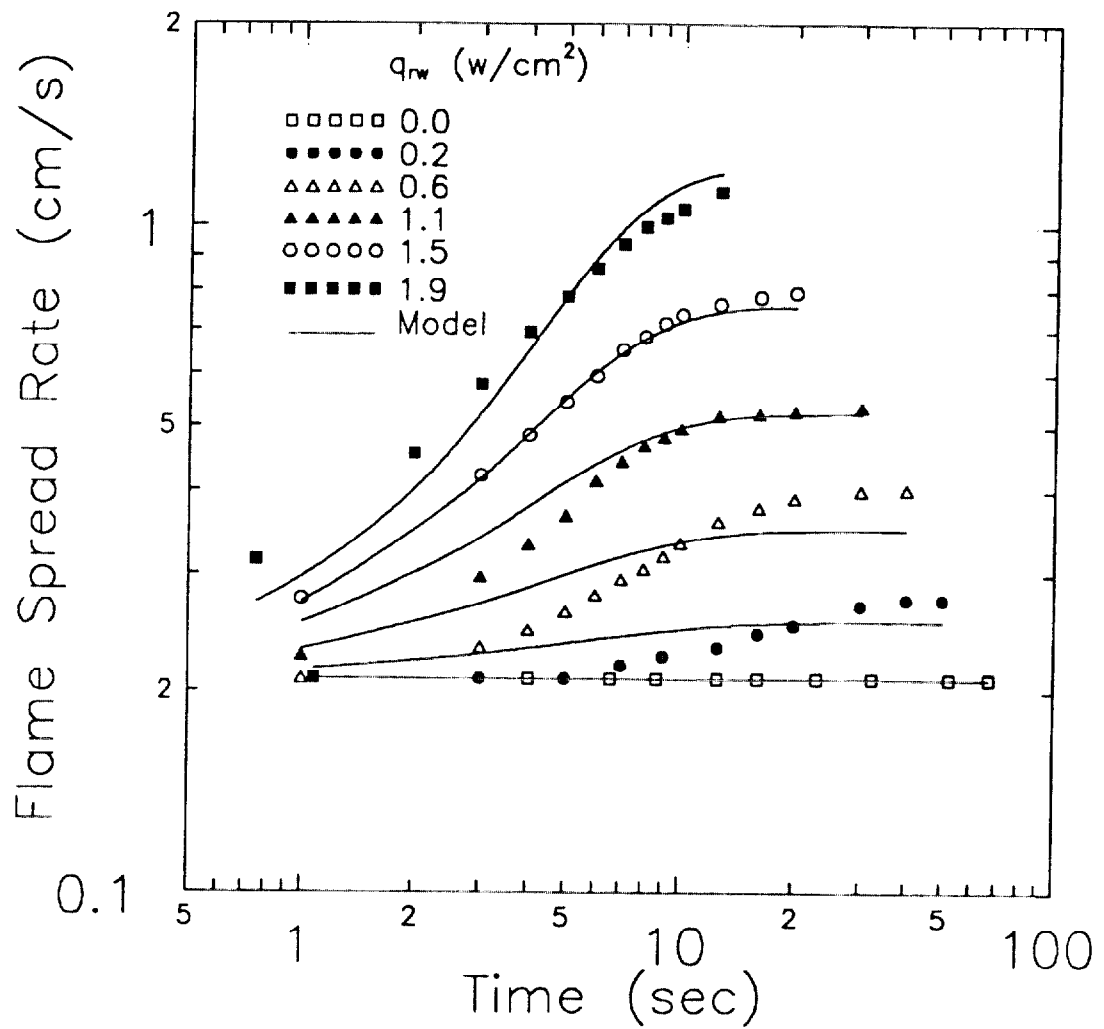
Figure B-4.   Model Predictions of the Downward Flame Spread Rate Data from Reference 5 as a Function of Time and Irradiances for the Paper.

Figure B-5.   Model Predictions of the Downward Flame Spread Rate Data from Reference 6 as a Function of Oxygen Concentration and Thermal Thickness at Normal Gravity Conditions.
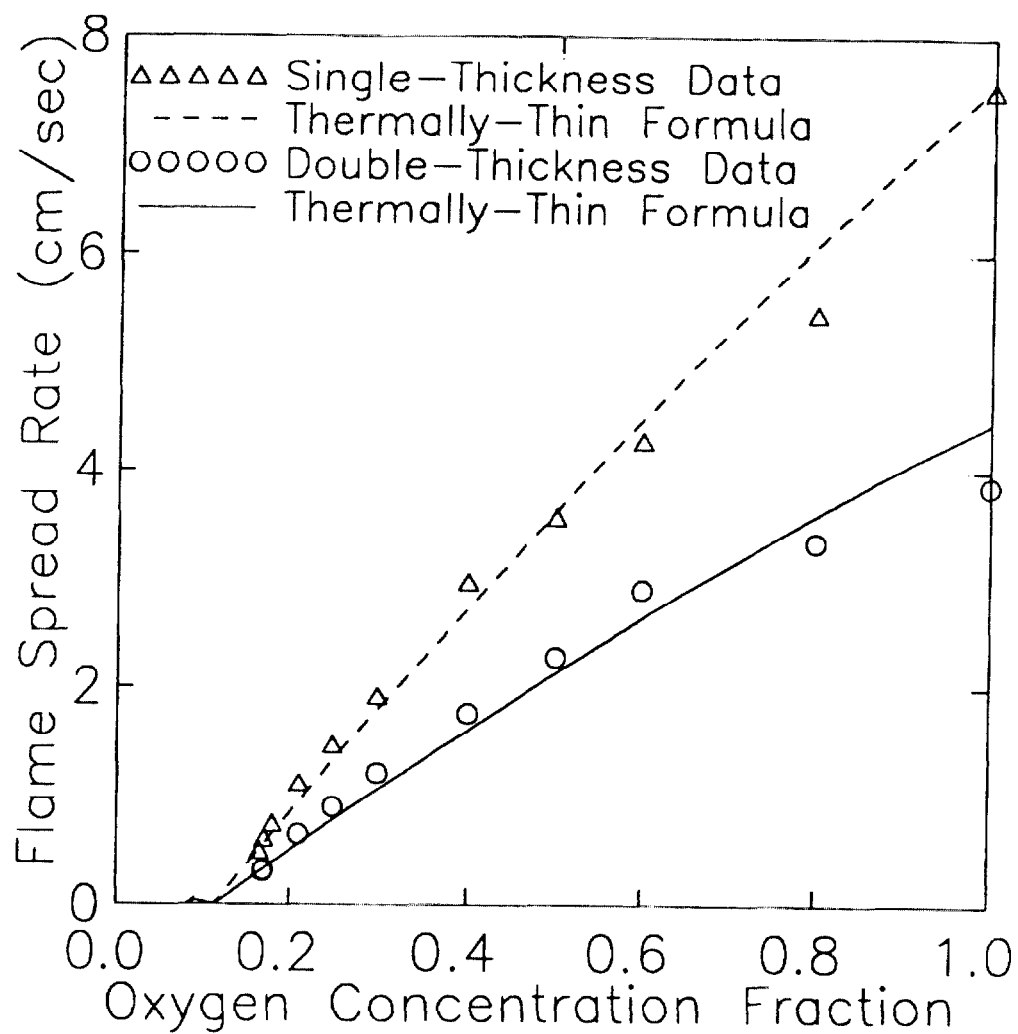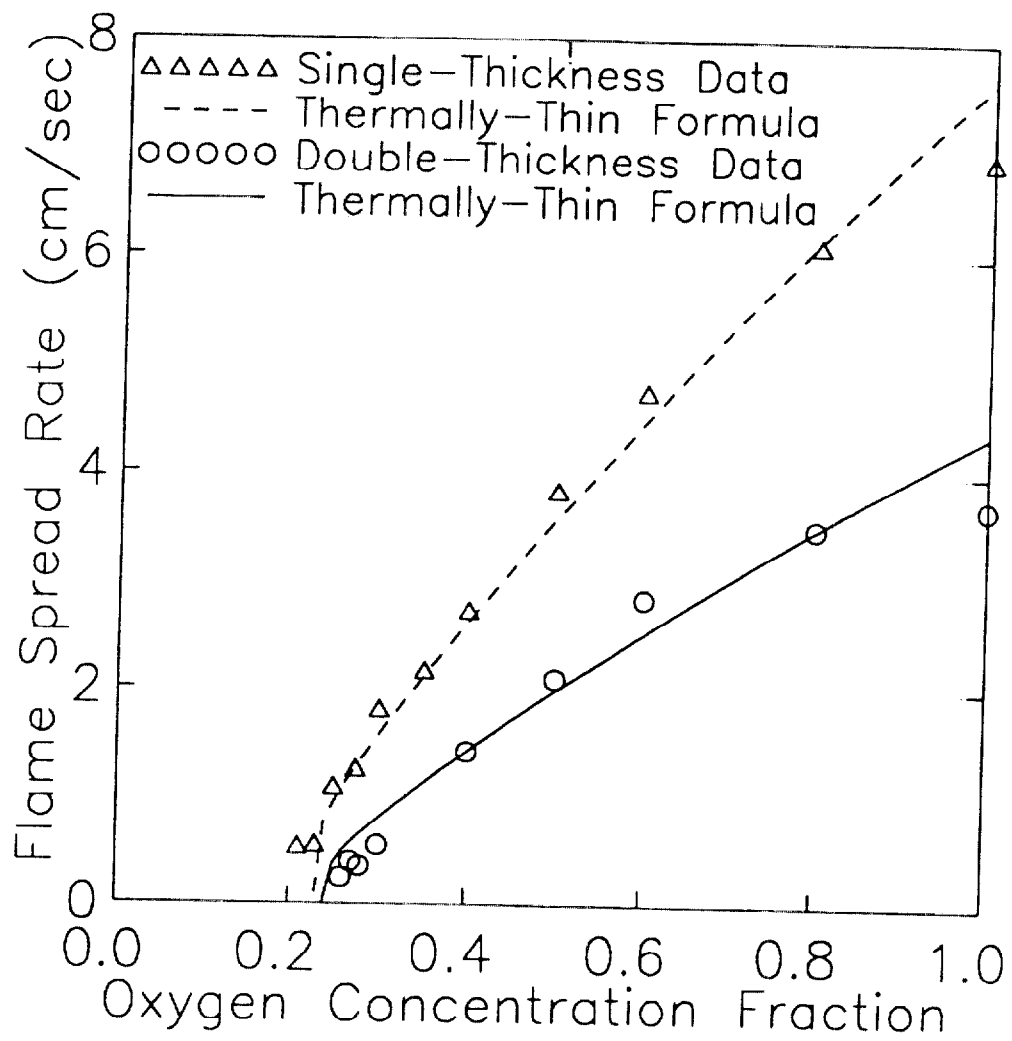
Figure B-6.   Model Predictions of the Opposed Flame Spread Rate Data from Reference 6 as a function of Oxygen Concentration and Thermal Thickness at Microgravity Conditions.

flame spread underneath the sheet was simulated by assuming the oxygen/fuel mass ratio approached the value of 1.185 as the inclination angle reached 180 degrees. This simulation was performed using the empirical equation,

$$\phi = \phi_{st} + \sqrt{\cos(\theta)} \, (\phi_{lean} - \phi_{st}) \tag{17}$$

The difference in flame spread behavior above and below the sheet is explained as follows. It was observed[4] that the curling of the ash behind the pyrolysis zone restricted the flow of combustion products from the flame front downstream. With this stratified flow of combustion products below the lower surface, mixing with the surrounding fresh air was poor. The pyrolyzed fuel vapors would accumulate beneath the lower surface and the flame would spread through the mixture of the accumulated fuel vapor and poorly entrained air. Therefore, we surmised that the flame front below the paper burns less lean as the surface becomes more horizontal. This was simulated with Eq. (17).

The different irradiant levels affect the flame spread rate versus time[5] as shown in Figure 4. With the model, the thermal thickness was calibrated as $\rho_o C_{p_o} \delta_o = 0.0067$ J/cm^{2}K; this fitted the data at zero irradiance. This is about 33 percent higher than that implied in Reference 5. The filter paper is known to absorb moisture; this can explain much of the higher filter density that results in a higher thermal thickness. The rest of the model constants were kept the same, including setting absorptivity at 0.4 because of irradiance on only one side. For a given irradiant level, the flame spread rate increases with time primarily because the preheat temperature increases with time in Eq. (2). The thermal radiation effects incorporated into Eqs. (7) and (14) had a negligible contribution to the prediction of the flame spread rates. The predicted flame spread rates for surfaces in equilibrium with the irradiances compare very well with the data, whereas the rising flame spread rates are not predicted as well. This could be the result of the approximated approach to deriving a practical thermal response function.

The calibrated thermal thicknesses for the single- and double- thickness papers

($\rho_o C_{p_o} \delta_o$ = 0.00143 & 0.00243 J/cm^{2}K) were 13 percent higher than given in Reference 6 in order to fit their normal gravity data. The excellent results shown in Figure 5 demonstrate the model's predictability. At high oxygen concentrations, the flame spread rate is dominated by the adiabatic flame temperature and the reference temperature (Eqs. (12) and (15)). At low oxygen concentrations, the effects of Damköhler number, surface radiative flux, and buoyant flow velocity become important enough to cause a nonlinear flame-spread rate trend to a flame blowoff at some finite oxygen concentration. The corresponding fit to the micro-gravity data[6] (as shown in Figure 6) required the relative gravity to be 3.5 micro-g's, while the other model constants are the same as in normal gravity. This means the buoyant flow rate is somewhat greater than the flame spread rate. The predicted flame temperature is around 1500 ^{o}K in air, which is reasonable. The predicted flame-foot size in air is 0.51 cm in microgravity, which is also about the flame standoff distance measured in Reference 6. Note that flame quenching occurs at higher oxygen concentrations than that of the normal gravity environment in Figure 5. Our explanation for the oscillatory flame spread rate typically observed near quenching is the oscillations in the environmental parameters which is amplified in the flame spread rate.

The implicit algebraic formulation for the flame spread rate depends on solid fuel's thermal thickness, oxygen concentration, forced/buoyant flow velocity, pressure, and surface radiative flux that simultaneously and successfully fitted the several published data. The flame extinction in various extreme conditions could also be predicted. Thus, in Figure 7, a flammability curve (derived in Attachment 1) is predicted and compared with the data.
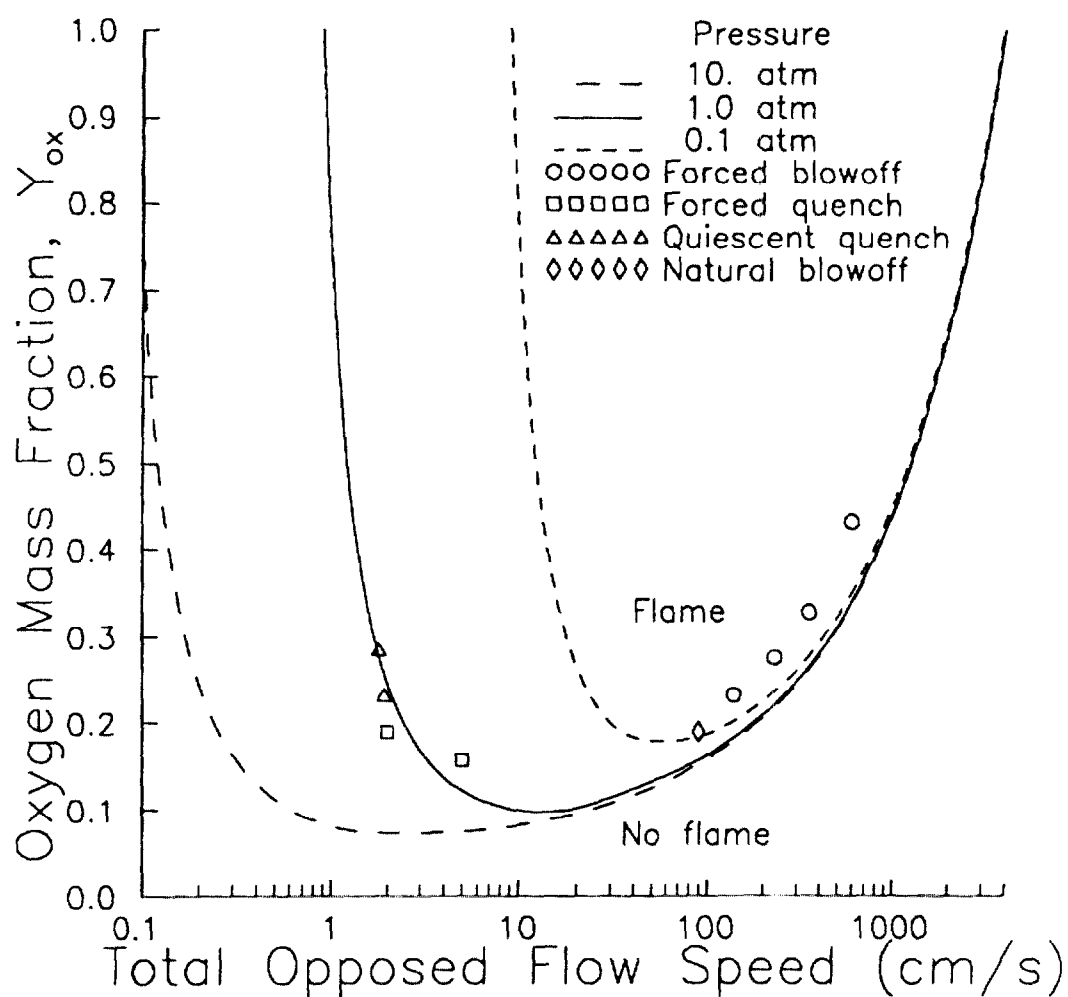
Figure B-7.   Model Predictions of the Flammability Curves and Comparison with Extinction
Data for Paper/Cards as a Function of Total Opposed Flow Speed and Pressure.

4. COMPARISON WITH THICK FUEL (PMMA) EXPERIMENTAL DATA

All solid fuels have some finite physical thickness, which seems to contradict the requirements of a semi-infinite medium for using the thermal inertia term. A common, practical approach of accounting for finite thickness is to define the transition between thermally thick and thermally thin behavior for the bulk material. Upon exposure to a surface heat flux, most solid fuels will initially respond in a thermally thick fashion. Standard texts on heat transfer (Reference 15 for example) show that at a given value of the Biot number, $Bi = h\delta/\lambda$, these materials will transition to a thermally thin behavior at a critical Fourier number, $Fo_c = \lambda t_c/(\rho C_p \delta^2)$. Since the typical Biot number is greater than 0.1 for the flame spread experiments with the PMMA, the critical Fourier number approaches unity.

4.1 Comparison with piloted ignition data for finitely thick PMMA

If the preheat time exceeds critical time, t_c, then instead of using Eq. (4) to calculate the preheat temperature, one can use the equation

$$T_e = T_a + \frac{\dot{q}_{re}}{h_{eq}} \left\{ 1 - \exp\left(\frac{-h_{eq} t_e}{\rho C_p \delta + \rho_o C_{p_o} \delta_o} \right) \right\} \tag{18}$$

The calculated preheat temperature could be chosen as a maximum of Eqs. (4) and (18) to maintain continuity of temperature values. This also avoids an explicit evaluation for the critical time as a criteria for transition. Note that at transition the first derivative of surface temperature with respect to time would be discontinuous. Indeed, an exact infinite series solution for the surface temperature of a heated homogeneous slab as a function of Biot and Fourier numbers can be found in a standard text on conductive heat transfer. With thermal thickness of the top layer set to zero, the infinite series solution will approach Eq. (3) at large thicknesses and Eq. (18) at small thicknesses. If the Biot number

is considered to be very small, then a very good approximation to the series solution is given by the equation:

$$\frac{h_{eq}(T_e - T_a)}{\dot{q}_{re}} = \left\{ \left(\frac{2}{\sqrt{\pi}} Bi_{eq} \sqrt{Fo} \right)^3 + \left(Bi_{eq} Fo \right)^3 \right\}^{\frac{1}{3}}$$ (19)

The first and second terms within the cubics on the equation's right side are also the first term in the Taylor expansion of Eqs. (4) and (18), respectively. The cubic smoothing of the same form as Eq. (19) could be applied directly to Eqs. (4) and (18). This would essentially achieve a smooth transition from thermally thick to thermally thin response. At the equilibrium limit, this smoothing procedure can result in a 26 percent overprediction. Regardless, the cubic smoothing procedure is demonstrated in Figure 8. This figure shows the fit for time to ignition versus irradiance data[16,17]. The corresponding PMMA thermal properties are

$T_{ig} = 650$ °K   (References 18 and 19),

$\rho C_p \lambda = 0.5$ (kW/m^2 °K)^{2}s,

$\lambda = 0.268$ (W/m°K)   (Reference 20),

$\delta = 1.28$ cm   (Reference 16).

In the literature, the surface ignition temperature of PMMA has been reported as low as 636°K and as high as 668°K. Recent measurements[18] provided values of 648 to 653°K for clear PMMA. For the Rohm and Haas black PMMA, Reference 19 reports a measured value of 653°K. The thermal inertia of PMMA can be as low as 0.33 and as high as 0.9 (kW/m^2 °K)^{2}s, depending on the choice of the elevated referenced temperature for the PMMA[20]. The most common value is 0.66, whereas our value of 0.5 (which fit the data in Figure 8) was also found to be the optimum value for the fit to the flame spread data. A closer examination of Figure 8 shows that the equilibrium conditions have not yet been reached at the ignition time of 1000 seconds. Transitioning from thermally thick to thin behavior began
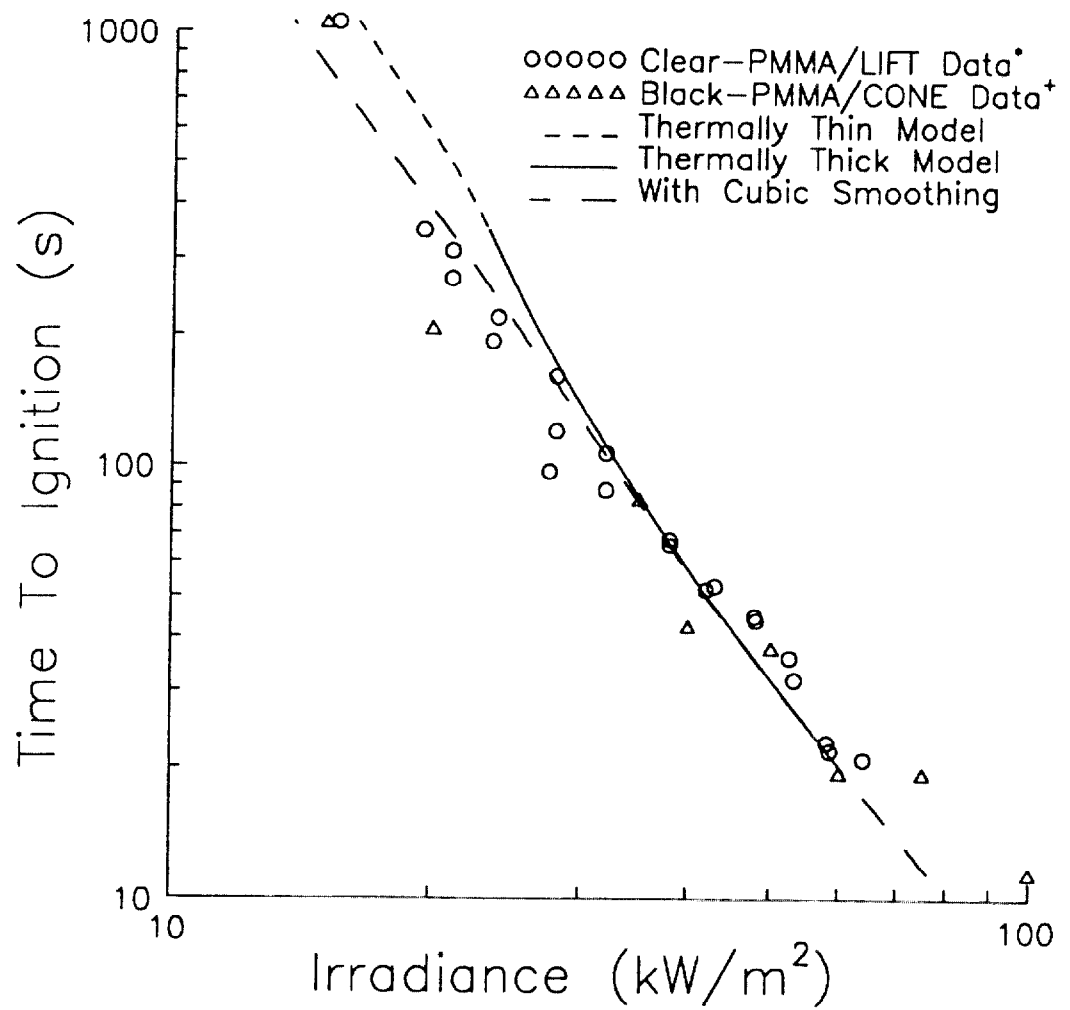
Figure B-8.   Model Predictions of the Time to Ignition Data from References 16 and 17 as a Function of Irradiance for the 1.28 cm thick PMMA.

at around the ignition time of 100 seconds. If the thermally thick formula only was used to fit the data, the ignition temperature would be too low, the thermal inertia would be too high, and the correlation coefficient would be poor. Subsequent analysis of the flame spread rate over a transient preheated surface would have also provided inconsistent results.

4.2   Comparison to the flame spread rate data for variably thick PMMA

The flame spread rate can also transition from a thermally thick to thin behavior. If the characteristic ignition time, $t_{ig} = \delta_f / V_f$, exceeds the critical time, then instead of Eq. (1) we have the thermally thin formula to calculate the flame spread rate

$$T_{ig} = T_e + \cfrac{\dot{q}_{cf}}{h_{ig} + \cfrac{V_f}{\delta_f}(\rho C_p \delta + \rho_o C_{p_o} \delta_o)} \tag{20}$$

The flame spread rate could be chosen as a maximum of the values calculated from Eqs. (1) and (20). Since the spread rate would abruptly change direction at the critical thickness, we examined the experimental data to verify this approximation. Reference 21 reported experimental results for downward flame spread rate over the different thicknesses of a PMMA slab. Their data (as plotted in Figure 9) show that the flame spread rate transition is rather gradual over the whole regime. Taking the power law formulation of Eq. (19) as a guide, the interpolation between Eq. (1) and Eq. (20) is given by

$$\frac{h_{ig}(T_{ig} - T_e)}{\dot{q}_{c_f}} = \left\{ 1 + \frac{1}{Bi_f(Fo_f^{n/2} + Fo_f^n)^{1/n}} + \frac{\rho_o C_{p_o} \delta_o}{\rho C_p \delta\ Bi_f\ Fo_f} \right\}^{-1} \tag{21}$$

where the Biot and Fourier numbers for flame spreading are,

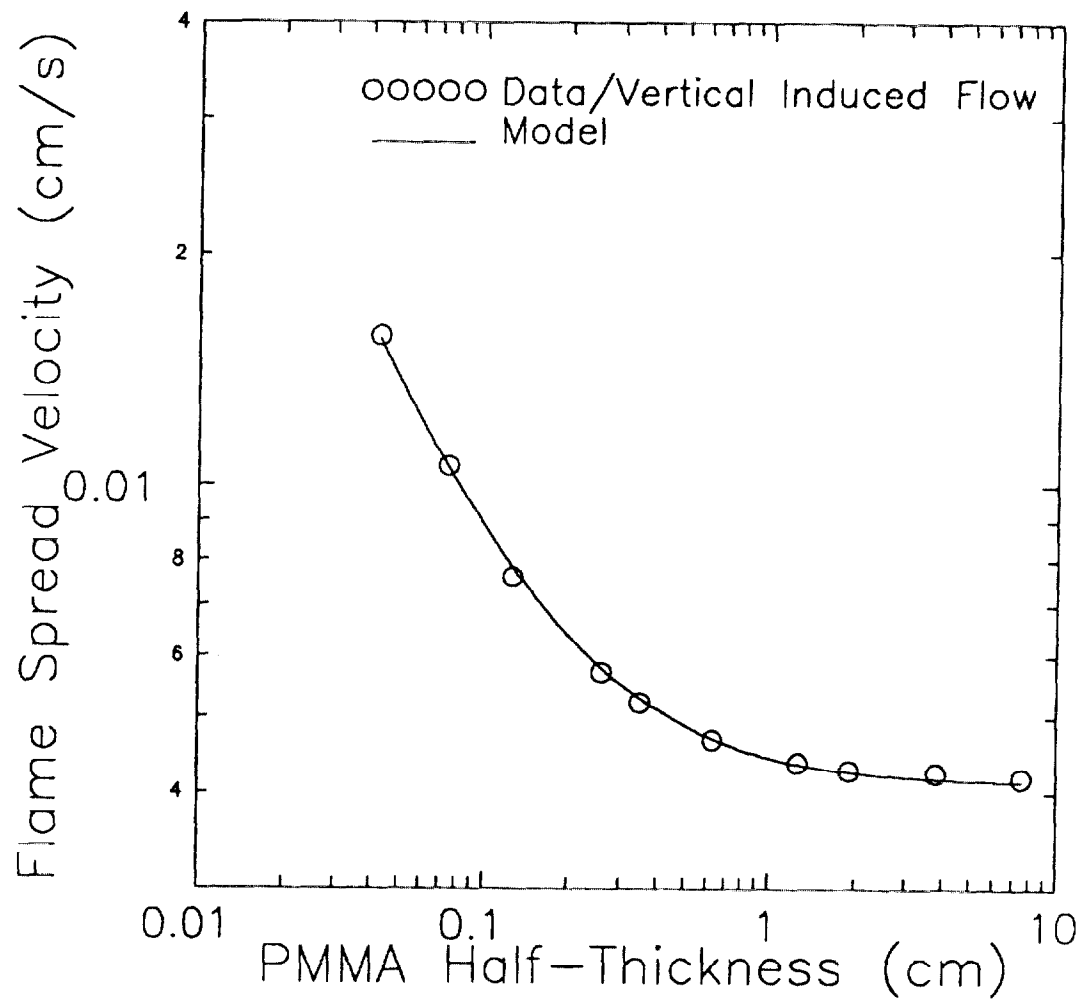$$Bi_f = h_{ig}\delta/\lambda \tag{22}$$

Figure B-9.   Model Predictions of Downward Flame Spread Rate Data from Reference 21 as a Function of the PMMA Half-Thickness.

$$Fo_f = \frac{(\lambda/\delta)}{\dfrac{V_f}{\delta_f}\rho C_p \delta} = \frac{(\lambda/\delta)^2}{\dfrac{V_f}{\delta_f}\rho C_p \lambda} \tag{23}$$

To fit the data in Figure 9, we set the top-layer thermal thickness to zero and rearrange Eq. (21) to obtain

$$V_f = V_{f_\infty}\left\{\frac{1}{2} + \sqrt{\frac{1}{4} + (\delta^*/\delta)^n}\right\}^{\frac{2}{n}} \tag{24}$$

where the minimum flame spread rate and transition length scale are related to some fundamental parameters as

$$V_{f_\infty} = \frac{\delta_f}{\rho C_p \lambda}\left(\frac{\dot{q}_f}{T_{ig} - T_e} - h_{ig}\right)^2 \tag{25}$$

$$\delta^* = \lambda\left(\frac{\dot{q}_f}{T_{ig} - T_e} - h_{ig}\right)^{-1} \tag{26}$$

If all the fundamental parameters in these two equations could be obtained independently from other experiments, only the power coefficient, n, need to be calibrated to fit Eq. (24) to the data. Determining the values for the fundamental parameters is difficult because the PMMA half-thicknesses in other experiments range from 0.13 to 1.9 cm, with most of them at around 0.5 cm[2,3,5,16,18,19]. Although these half-thicknesses are clearly greater than the critical value, the data shown in Figure 9 demonstrate the significant influence of the PMMA finite thickness on the flame spread rate. A closer examination of Eqs. (25) and (26) revealed that the values of all the parameters in these equations remain constant as long as the surface orientation and the environmental conditions do not change. Thus, to make further progress in analyzing the data, the variables V_{f_∞} and δ^* were also calibrated to fit Eq. (24)

to the data in Figure 9. The result is,

$$V_{f_-} = 0.00411 \ cm/s, \quad \delta^* = 0.106 \ cm, \quad n = 1.3$$

It is not surprising that the power coefficient is less than a theoretical value (3) because the surface heat-flux distribution is exponential rather than constant, and the Biot number is not small. The values for the minimum flame spread rate and transition length scale are quite reasonable (and are used to calibrate two of the six fundamental model constants). An examination of Eqs. (24) through (26) shows that variations in the structure of the laminar diffusion flame will have opposing effects on the flame spread rate dependency on the half-thicknesses. The implication is that the curve in Figure 9 is not unique because the minimum flame spread rate and the transition length scale are functions of changing environmental parameters.

4.3   Calibration of the model parameters for the PMMA diffusion flame

Reference 2 provides the pivotal flame spread experiments to initially calibrate the fundamental model constants for the PMMA flame. Some constants for the PMMA flame have been measured; i.e., $\Delta H_c = 25810$ J/g, and $L = 1591$ J/g$^{2-6}$. The parameters varied in the experiments were forced flow velocity and oxygen mass fraction. The buoyant flow velocity in the apparatus in the vertical orientation was significant at forced air velocities less than about 50 cm/s. The effect of external irradiances was not investigated. The corresponding flame spread rate data is shown in Figure 10 for the wide range of forced air flow and oxygen mass fraction. At low oxygen mass fractions, the flame spread rate remains level and then drops off at critical values of forced air flow. At high oxygen mass fractions, the flame spread rate will at least increase over a wider air velocity range, then drop off at higher levels of forced air flow. This behavior is hardly anticipated by the deRis flame spread theory, which predicts
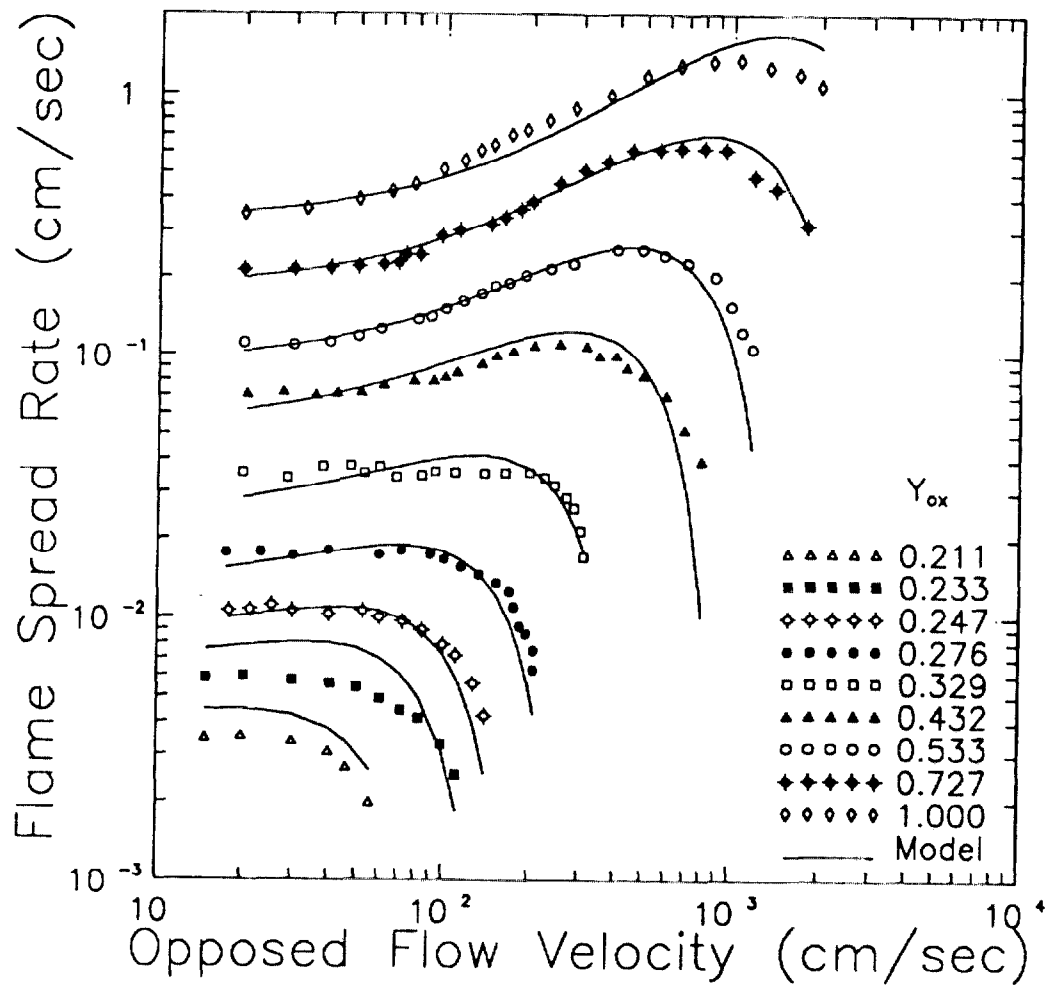
Figure B-10.   Model Predictions of Opposed Flame Spread Data from Reference 2 as a Function of Opposed Flow Velocity and Oxygen Mass Fraction for the Thick PMMA.

the flame spread rate to be proportional to the opposed flow velocity. Thus, researchers only applied the deRis theory to the high Damköhler number limit. When the detailed numerical models demonstrated the increasing role of the lean, premixed flame foot and the leakage of reactants through the flame sheet at higher flow velocities, the rational and analytical analyses were severely challenged.

The success of the current model with thin fuels indicates that similar modeling features also apply to the thick fuels. The strategy for calibrating the model constants, however, is more involved. The overall levels of the model predictions were adjusted with the model parameters ϕ, a, b, while the local variations were adjusted with the model parameters C^*, C_o, C_1. The values of the six model parameters need not be unique to obtain a good fit to the data. The sensitivity analysis showed that the constants, a and b, are only important at oxygen mass fractions at and above 0.432. The remaining four model constants were then calibrated to not only provide a good fit to the data in Figure 10, but to also provide consistencies with the measured flame temperatures and flow velocities, and to other flame spread experiments in a different environment. The resulting calibrated values for the flame structure are:

$C^* = 5.0$,

$\phi = 4.37$,

$C_o = 0.0 \ ^oK(gs/cm^3)^{1/2}$,

$C_1 = 41.1 \ ^oK^2(gs/cm^3)^{1/2}$,

$a = -1800 \ ^oK$, and

$b = 1.2$.

The model's prediction for the buoyant flow velocity at 22 cm/s in the air ($Y_{ox} = 0.233$) with a forced flow velocity of 15 cm/s compares favorably with the 30 cm/s reported in Reference 2. The

corresponding flame temperature was calculated to be 1309 °K; this seems reasonable. Since each model constant is closely associated with a physical mechanism, it is possible to anticipate the changes in certain constants as experimental data in other configurations are considered. The first obvious parameter to vary is the effective oxygen-to-fuel-mass ratio, since it was formulated to increase as the solid fuel tilted toward horizontal in the case of paper/card fuels. As the experimental configurations of lateral and horizontal flame spread are examined, the constant for the buoyant flow velocity is likely to vary.

The next challenge to the model predictability is the experimental data for measuring flame spread rates on PMMA for elevated gravities, pressures, and oxygen mass fractions[22]. The environmental conditions of forced flow and external thermal irradiances were not investigated. The apparatus is the same as in Reference 3, where it was used to measure the flame spread on the paper/cards in a tiltable chamber on a centerfuge. Figures 11 and 12 show that the flame spread rate increases with pressure and oxygen mass fraction. This flame spread behavior is anticipated by the deRis formula.

The flame spread rate as a function of elevated gravity changes from a negative slope at lower oxygen mass fractions to a positive slope at higher oxygen mass fractions. This behavior is not anticipated by the deRis formulae, but is anticipated by a reduction of flame temperature as a function of Damköhler number (see Eq. (13)). Indeed, the best fit to the data in Figures 11 and 12 has $C^* = 2.2$, while all other model constants for PMMA remained the same as before. With these model constants, the slope of flame spread rate as a function of relative gravity is predicted to be zero at $Y_{ox} \approx 0.23$ as compared to $Y_{ox} \approx 0.25$ observed in the data. In fact, taking the derivative of the flame spread rate with respect to relative gravity will also show that the zero-slope constraint does not

Figure B-11.   Model Predictions of Opposed Flame Spread Rate Data from Reference 22 as a Function of Relative Gravity, Oxygen Mass Fraction, and Pressure on the PMMA Slab.
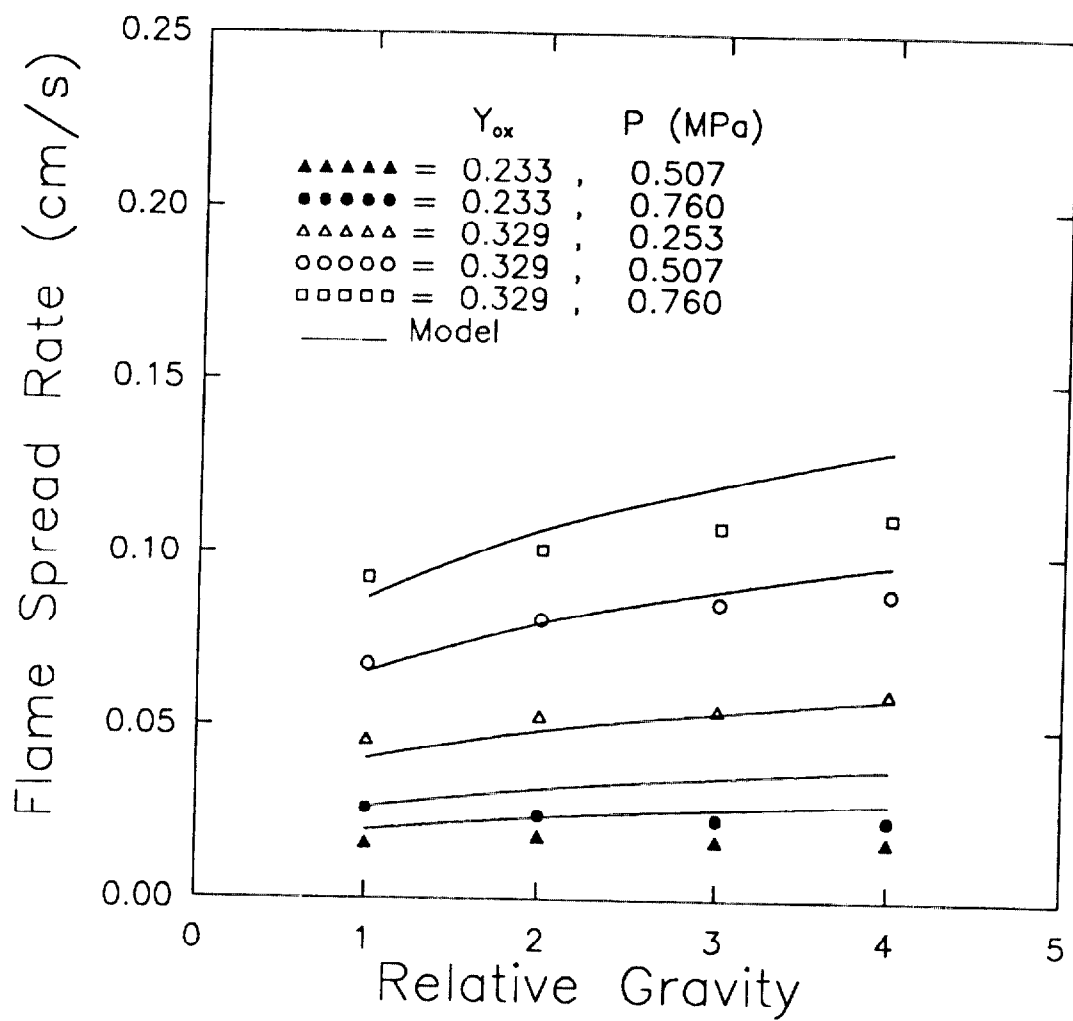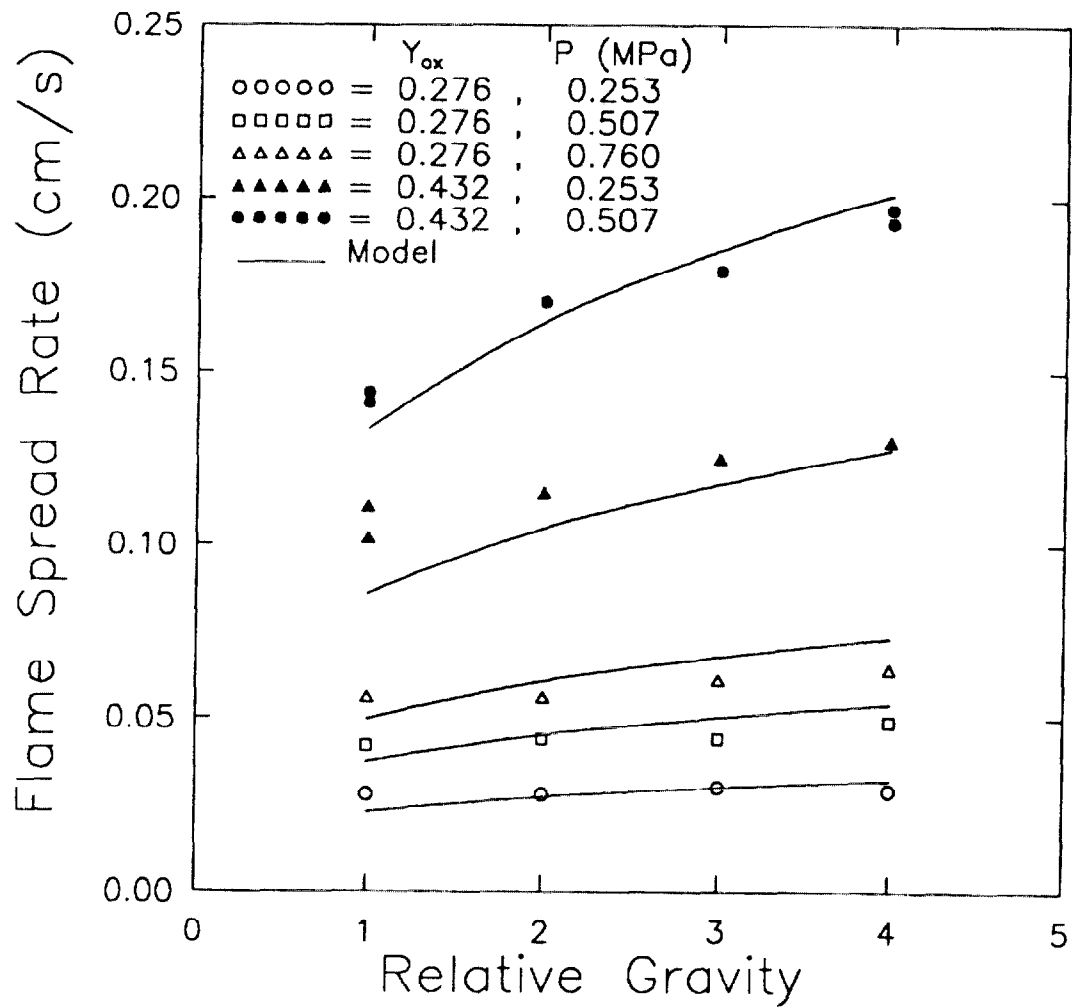
Figure B-12.   Model Predictions of Opposed Flame Spread Rate Data from Reference 22 as a Function of Relative Gravity, Oxygen Mass Fraction, and Pressure on the PMMA Slab.

depend on the fuel bulk properties, but has a small dependence on pressure. This prediction appears to agree with additional data presented in Reference 22. With these results, the salient features of the model have been demonstrated. That is, the environmental parameters of pressure, oxygen mass fraction, relative gravity, and fuel bulk properties are input into separate equations, which are in turn input to the flame temperature formula (Eq. (13)). The result is the capability to predict flame spread behavior at elevated conditions with only a recalibration of the buoyant flow constant.

The external irradiances, as an environmental condition, will enhance the flame spread rate over the PMMA sample. The data for downward flame spread[5] (as plotted in Figure 13) have the spread rate accelerating with time in response to different levels of external irradiances. The flame spread rate corresponding to zero irradiances was fitted by a recalibration ($C^* = 1.3$) while all other model constants for PMMA remain the same as above. The value for the buoyant flow constant is the lowest for all the experimental configurations considered. The chamber dimensions could influence the boundary layer structure of the flame and affect the thermal radiation field. It seems that closer the chamber wall is to the burning fuel, greater is the flame spread rate (which then effectively increases the buoyant flow constant). A quantitative assessment of this effect on the flame spread rate will require capabilities of the Furniture Fire Model[23] or similar models to calculate the thermal radiation field and transient heating of the chamber wall. Indeed, the fit to all data in Figure 13 required increasing the measured value of radiance from the test's flaming panel by 70 percent. Since the radiometer is focussed on the flaming panel, the thermal radiation from chamber walls to PMMA slab is not captured in the measurements. The PMMA slab is thick so that a good sized wall fire can develop to heat the chamber wall. In any case, Eqs. (3) and (18) with the cubic smoothing were effective in preheating the PMMA so that the flame spread rate accelerates as a function of time. Other experimental configurations which include external irradiance on the PMMA are considered later in this section.

Flame Spread Rate (cm/s)

q_{rw} (w/cm^2)
- □□□□□ 0.0
- ●●●●● 0.2
- △△△△△ 0.4
- ▲▲▲▲▲ 0.6
- ○○○○○ 0.8
- ■■■■■ 1.1
- ◇◇◇◇◇ 1.3
- ⬗⬗⬗⬗⬗ 1.5
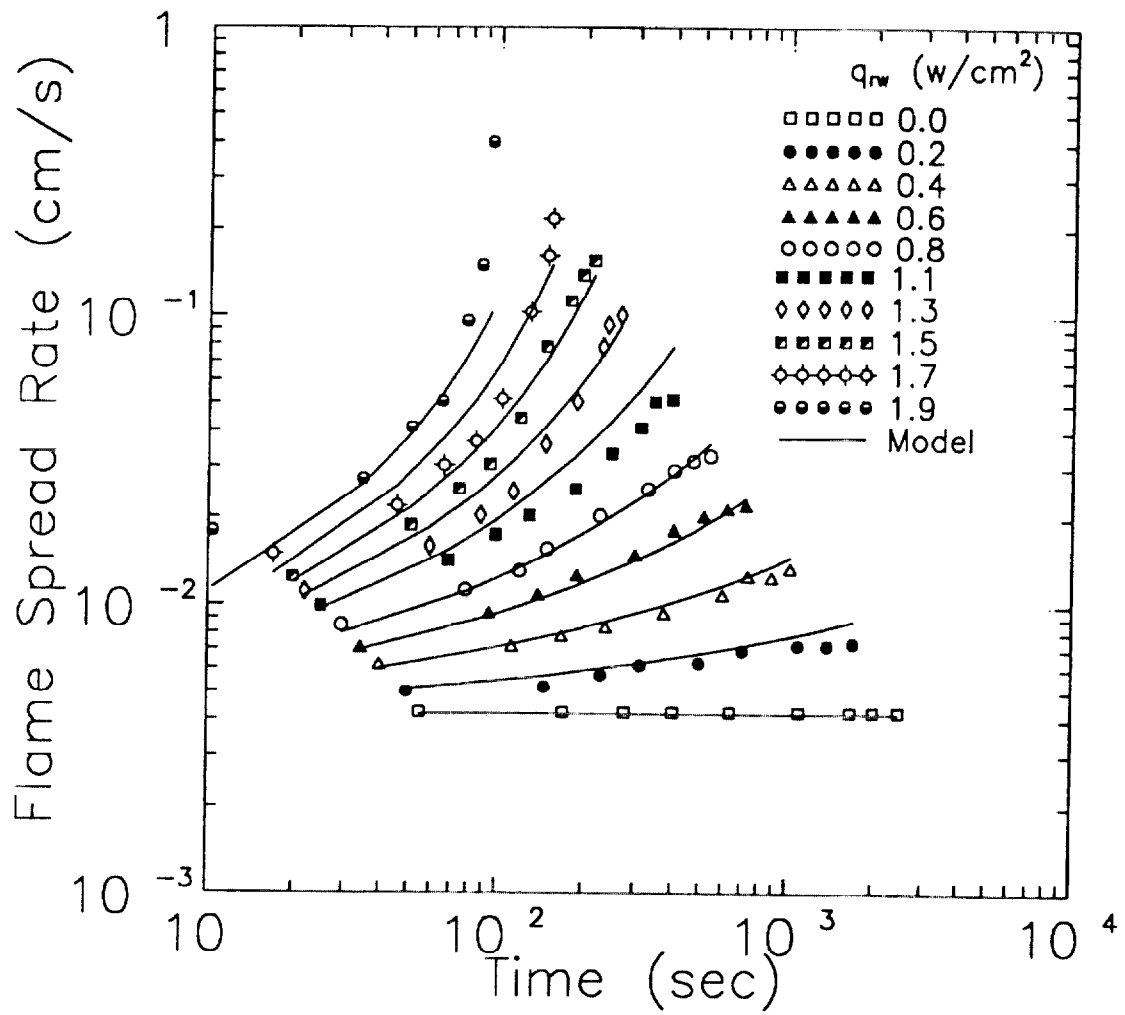- ◇◇◇◇◇ 1.7
- ●●●●● 1.9
- —— Model

Time (sec)

Figure B-13. Model Predictions of Downward Flame Spread Rate Data from Reference 5 as a Function of Time and Irradiance on the PMMA Slab.

Returning to the thickness variations of a vertically orientated PMMA slab, and to the experimental configuration of Reference 21, the fit to Figure 9 provided values of V_{f_∞} and δ^*. Since these fitting parameters are related to fundamental model constants through Eqs. (25) and (26), the result is to calibrate the buoyancy flow constant as $C^* = 1.3$, while all other model constants for PMMA remain the same as above. These are essentially the same constants used for the previous experimental configuration. The corresponding flame temperature and buoyant velocity are predicted as 1419 °K and 17.5 cm/s, respectively. This compares reasonably with the measured peak velocity at 22.5 cm/s. The corresponding net heat flux from the flame front to the vaporization front was predicted to be 9.9 W/cm^2. Ito and Kashiwagi[18] reported a normal heat flux of 7 W/cm^2 and a streamwise heat flux of 3.2 W/cm^2 (for a net sum of 10.2 W/cm^2) at the vaporization front of a vertical, 2.5-cm thick PMMA slab. They concluded that most of the heat flux from the flame to PMMA is through the gas phase; this is consistent with deRis theory of flame spread.

Reference 21 contains additional flame spread data for the inclined PMMA slab in a normal air environment. This data is shown in Figure 14. The increase in the flame spread rate as the slab became more inclined could not be explained with the current set of values for the model constants. The flame spread rate can be increased by either increasing C^* or decreasing ϕ as the inclination angle deviates from 90 degrees. Reference 18 contains detailed measurements of the flame heat flux distribution on the PMMA slab surface at different inclinations. This information can be used to determine the appropriate option to use to increase the flame spread rate. Basically, the peak heat flux decreases and its thermal length increases as the slab deviates from the vertical direction. This trend in the surface heat fluxes indicates that ϕ should decrease with inclination. The data was fitted by using Eq. (17) and setting $\phi_{st} = 2.9$. Note that the model extrapolates beyond the data for the inclination angles less than 30 degrees and greater than 150 degrees. This extrapolation will be in error at the transition of the wall
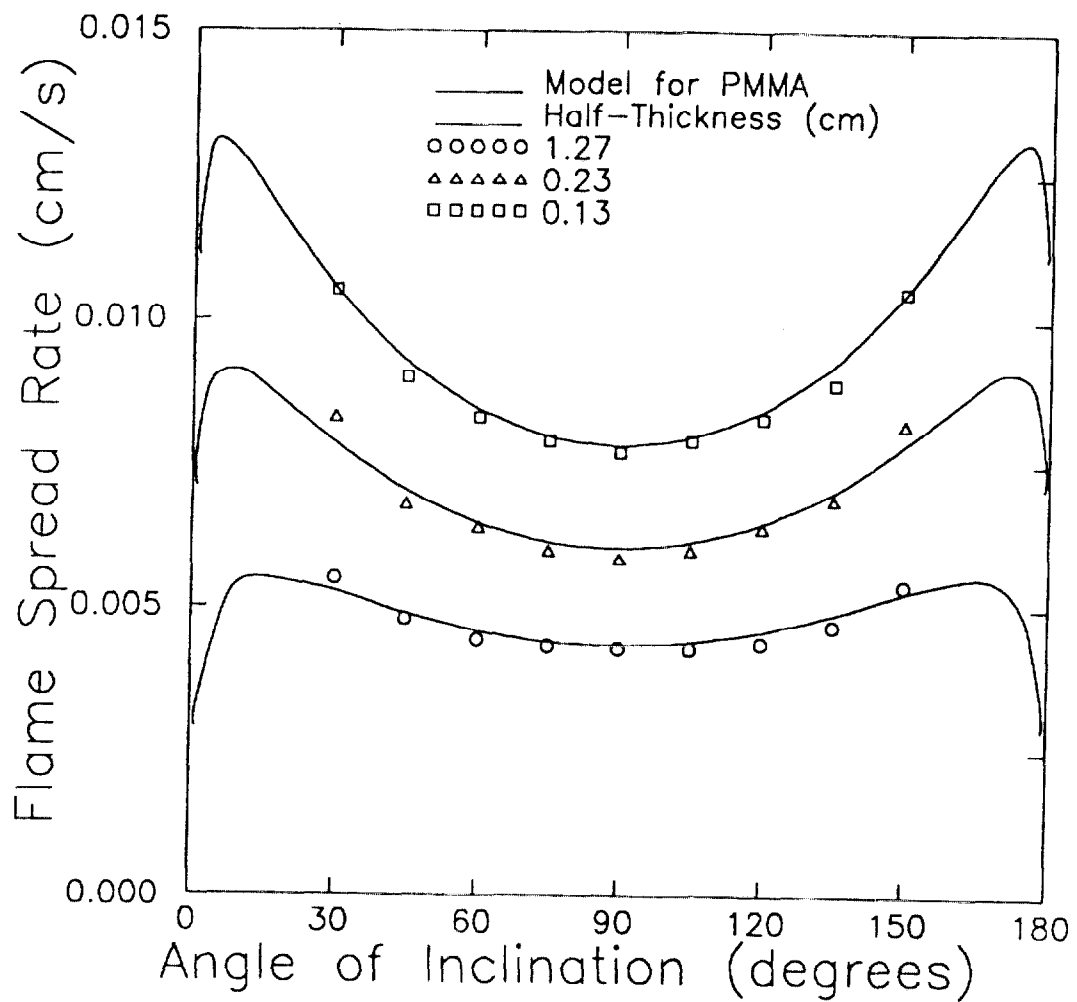
Figure B-14.   Model Predictions of Downward Flame Spread Rate Data from Reference 21 as a Function of Inclination Angle and PMMA Half-Thickness.

flame to a pool-like fire. The physical mechanism for the buoyant velocity becomes connected with the entrainment of flow into the flame.

As a crude approximation, consider the following. The streamline at the boundary layer thickness turns upward as the entrained flow is heated by the flame. The vertical component of the entrained flow increases in velocity in accordance with the vertical buoyancy. However, the total flow speed remain fairly constant along the streamline because it requires continuity of flow. When the streamline from the boundary layer thickness becomes nearly vertical, the total flow speed begins to increase. The vertical flow speed at this critical height should be about equal to the horizontal flow speed at the flame front. The critical height that would give a correct value for the horizontal induced flow speed is assumed proportional to the thermal length scale, δ_f, of the moving diffusion flame. This assumption brings us back to Eq. (16), where the cosine dependency is removed and the buoyancy flow constant C^* is given a new interpretation.

The data[19] for the horizontal flame spread as a function of time over a black PMMA slab is shown in Figure 15. For a narrow slab of 7 cm with a 4.9 kW/m^2 imposed irradiance, the irradiance from the fire plume is calculated[19] to contribute a very small percentage to the flame spread rate. Also, as long as the flame propagated to less than 10 cm for any width of the slab, the fire-plume irradiance was negligible. To predict the data, a personal computer program, LIFTFIT, was developed to calculate the elapsed time as a function of flame position by integrating the inverse of the flame spread rate. The effect of a constant irradiance to preheat the PMMA over a long time period was included. This program was coupled to a curve fitting subroutine[9] to automatically calibrate two of the model constants, ϕ and C^*. Their values are shown in Table 1, while all other model constants remain the same as before. The calculated flame temperature of 1456 °K is in close agreement with the value measured in Reference 19 (1460 °K). The calculated induced flow speed of 32.4 cm/s is in agreement with the often quoted
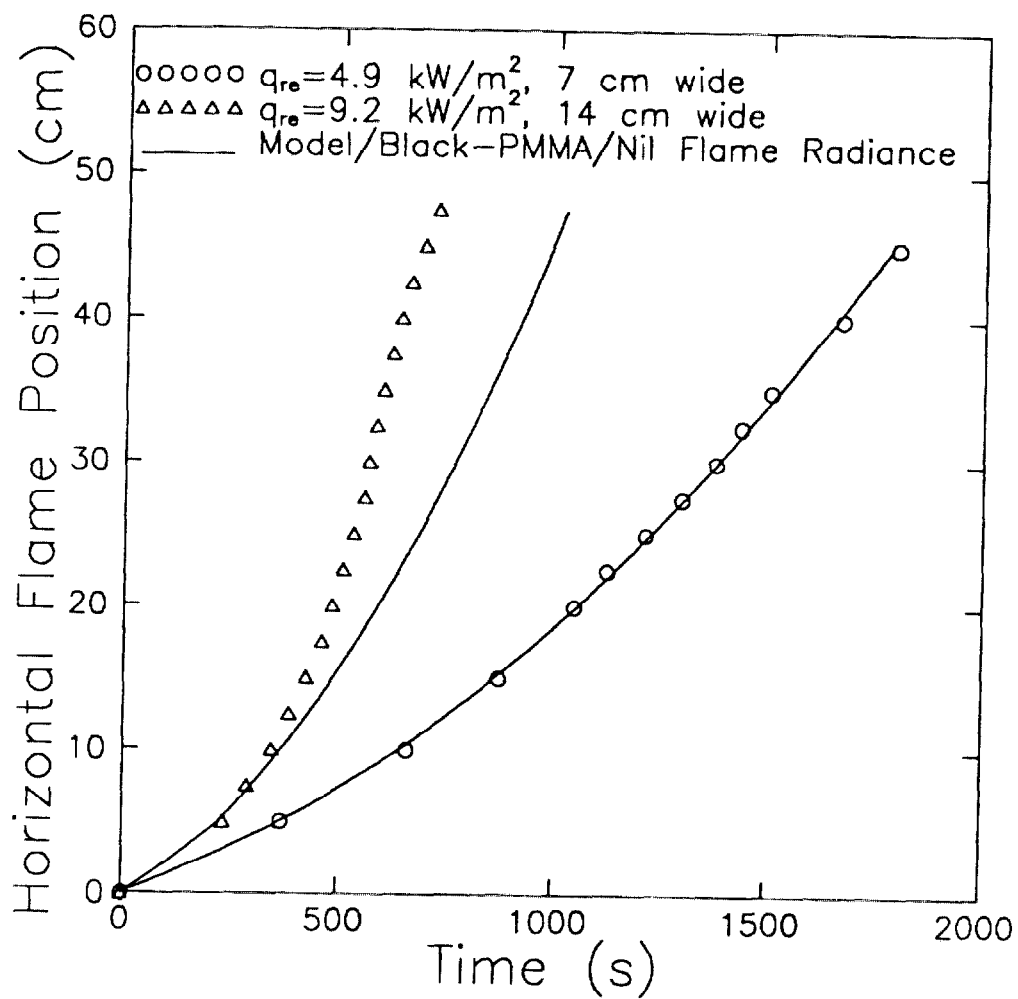
Figure B-15.   Model Predictions of Horizontal Flame Spread Data from Reference 19 as a
Function of Time and Irradiance on the Black-PMMA Slab.

TABLE B-1

Fitted Model Constants and Their Derived Parameters for Various

Flame-Spread Configurations in Normal Air Environments

Reference	Test Condition	Spread Direction	ϕ	C^*	T_f (°K)	V_g (cm/s)	q_f (w/cm²)	δ_f (mm)
2	PMMA/Air	Down	4.37	5.0	1309	22.3	18.5	0.15
5,11	Vertical	Down	4.37	1.3	1419	17.5	9.9	0.32
16	PMMA/D-16	Down	4.39	4.1	1441	31.3	9.7	0.29
16	PMMA/D-29	Down	4.42	3.95	1465	33.2	9.9	0.32
16	PMMA/L-2	Lateral	4.39	4.1	1442	31.5	9.7	0.3
NIST/LIFT	Black-PMMA	Lateral	4.39	4.1	1437	31.1	9.6	0.29
19	# 11 & 21	Horizontal /Topside	4.40	4.0	1456	32.4	9.8	0.31

value of 30 cm/s in the literature. The flame foot heat flux of 9.8 W/cm^2 is in some agreement with Reference 18, which reported on the normal flux of 7 W/cm^2 and the streamwise flux of 2 W/cm^2 at the vaporization front of the horizontal PMMA slab. These levels of agreement with the measured values verify the approximation of the physical mechanism for the induced flow speed. Disagreement of the model's prediction with the data is expected when the fire-plume irradiance becomes significant, as is apparent in Figure 15 for the 14-cm wide slab. The inclusion of the fire-plume irradiance calculation into the flame spread model is beyond the scope of this paper.

The last set of data[16] considered is the downward and lateral flame spread on the LIFT apparatus[24]. The curve fits to the data are shown in Figure 16 using the computer program, LIFTFIT. The calibrated model constants for each of the four flame-spread tests are given in Table 1. As is typical with the LIFT, the flame spreads rapidly at first, then gradually decreases as the flame front moves further away from the external irradiant source. The external irradiance distribution has been precalibrated along the lateral direction[24]. However, the downward irradiance distribution needed recalibration because the wall flame spreading downwards over a thick fuel will partially block the external radiant source. Perhaps the radiant source was tilted slightly to prevent impingement by the wall flame. A recalibration of the external irradiance distribution for the downward direction was not suggested in Reference 16. Our approximation for the downward direction is to decrease the spatial dimension of the irradiance distribution by 25 percent of the distances beyond 100 mm.

Since flame spreading can begin at any time, the transient preheating of the solid fuel by the external irradiances are calculated using the formulae in this paper. Because of the long preheating times, it was important to transition from a thermally thick to a thermally thin behavior, even for the 1.28-cm thick PMMA slab. This is demonstrated by the excellent fit to the lateral flame spread data in Figure 16.
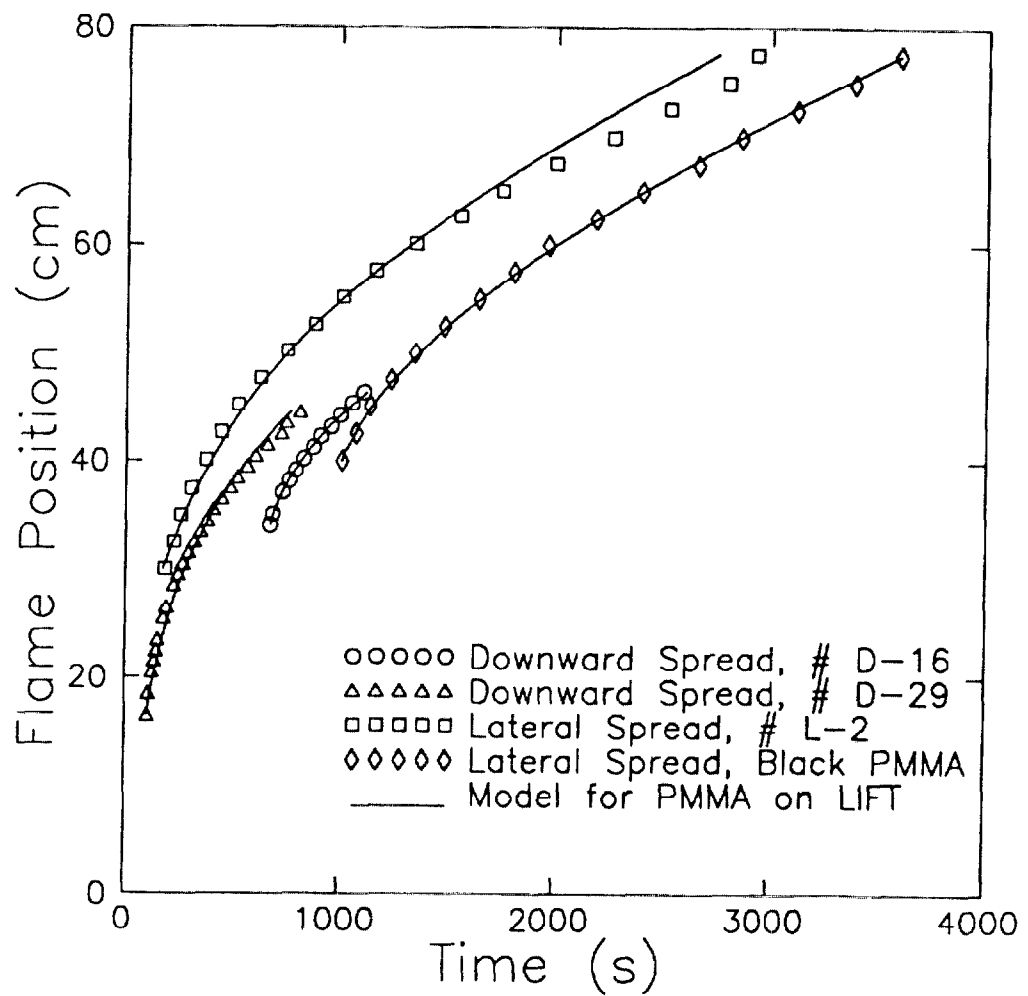
Figure B-16.   Model Predictions of Lateral and Downward Flame Spread Data from Reference 16 as a Function of Time on the LIFT.

A controversy exists on whether the lateral flame spread rate is dominated by the flame-sheet irradiance or by the conductive heat flux from the flame front. The results presented in Table 1 strongly support the dominance of the conductive heat flux on the lateral flame spread. The astounding fact in Table 1 is that the opposed flame spreading behaviors in the three primary directions have very similar values for the fitted model constants and derived model parameters. The physical mechanism for explaining the induced flow speed on the horizontal surfaces is also applicable to the lateral flame-spread geometry. The derived lateral flow speeds of 31.3 and 33.2 cm/s and the derived flame temperatures of 1441 and 1465°K are very reasonable values. As a final point, Sibulkin, et. al.[25], numerically demonstrated the Laminar bouyant diffusion flame over a vertical slab of PMMA is optically thin. That is, there were negligible effects on fuel pyrolysis rates due to flame irradiances. By inference, the effects of flame irradiance on the surface thermal response near the flame front is also negligible. With these results, the influence of the flame sheet irradiance on the lateral flame spread seems to be minuscule.

5.   CONCLUSION

A theory for the opposed-flow flame spread that could fit several experimental data in extreme environments was developed. The model fills a theoretical void between the power law correlations and the detailed numerical models. In fact, it was possible to have flame spreading predictions go as far as the flammability limits. An implicit algebraic formulation of the opposed-flow flame spread rate, as developed in this paper, was demonstrated to have the following features:

1.   A single formulation for the material thermal response was developed for paper, PMMA, or composites. The comparison of the thermal response model with the piloted ignition data provided reasonable calibrations of the thermal properties. These properties include thermal inertia, thermal

thickness, and surface ignition temperature. It was found that the transition from the thermally thick to thermally thin must be simulated for some ignition and flame spread situations, particularly for long exposure times or for low flame spread rates.

2.   The deRis formulation for the spread of laminar diffusion flame was extended to the extreme environments including: oxygen concentrations, diluenting gases, forced-flow velocities, relative gravities, pressures, imposed irradiances, surface radiative cooling, air temperatures, and surface orientations. In particular, the adiabatic flame temperature was reduced with the decrease in the Damköhler number and with the surface radiant cooling of the burning regions. The model predicted some unique flame spread rate dependencies not previously possible in other analytical flame-spread theories. The irradiance from the developing adjacent fire plume is not considered here, but is a subject for another paper.

3.   Only a few empirical, but physically tractable, constants were utilized. Each model constant could be identified with a physical mechanism. When fitted to the data, they also produced reasonable values of related parameters, such as the flame temperature and induced flow speed. Their values did not need to change from one experiment to the next, unless some specialized conditions of the experiment were identified.

4.   Since the flame spreading ceases discontinuously at the environmental limits of the formulation, it was possible to analytically construct the flammability curves for the paper/card and PMMA. Because of the discontinuity, most random variations in the environment conditions near the limits will result in the pulsations of the flame spread rate.

5.   The analysis of the lateral, horizontal, and downward flame spread over the PMMA slab showed some surprising results. Despite the differing experimental configurations, all the model constants had basically the same values. These results greatly simplify efforts to simulate a growing fire scenario on furnishings.

One deficiency with model validation is the absence of a certain class of data. An experimental investigation is needed in several areas. Direct observation of the flame spreading approaching extinction is needed to formulate further refinements to the flame temperature equation. Indeed, some kind of perturbation analysis applied to the deRis problem statement may reveal a more precise analytical form for the flame temperature equation. As the database on the effect of diluent gases on the opposed flame spread becomes available, the model should have gas properties modified to predict the data. The model predicts a flammability curve for the PMMA, which is not presented in this paper because of a lack of data in the low opposed-flow speed regime. A whole new collection of data which varies the environmental parameters for the lateral and horizontal opposed-flow flame spreading is needed. The cone calorimeter may be able to provide the ideal chamber for this flame spread study. Data is also needed for the composite materials, wood products, and plastics. A more thorough evaluation of the ignition and flame spread equations presented in this paper may reveal a systematic and economical approach to establishing the model constants from the bench-scale measurements. This would provide a major advancement in our ability to do full-scale fire simulations of newly developed materials.

The results provided in this paper have practical implications for the simulation of the opposed-flow fire spreading at any fire scale. Basically, the physical mechanism for the opposed-flow flame spread rate is the conductive heat flux from the flame front. The flame spreading should be solved as the integration of the flame spread rate because the heating lengths are on the order of a millimeter.

Meanwhile, the non-burning surfaces should be preheated with the irradiance from any source. A time dependent development of the irradiance, or even of the environmental parameters, will require the capabilities of FAST/FFM. The flame spread model presented in this paper can be directly incorporated into the furniture fire model to enhance its capability in fire scenarios involving oxygen vitiation, elevations of temperature and pressure in the lower gas layer, and of gas dilution. It seems feasible that we will eventually be able to use a personal computer to simulate fire scenarios in a submersible vehicle or a lunar colony base.

6. NOMENCLATURE

a Empirical constant in Eq. (15)

b Empirical constant in Eq. (15)

Bi Biot number

ΔH_c Heat of combustion (J/g)

C Empirical constants in Eqs. (13) and (16)

C_p Heat capacitance (J/g$^{\circ}$K)

g Gravitational acceleration (m/s^2)

Fo Fourier number

h Heat transfer coefficient (kW/$^{\circ}$Km^2)

L Heat of pyrolysis (J/g)

$\dot{q}$ Heat flux (kW/m^2)

t Time (s)

T Temperature ($^{\circ}$K)

V Velocity (m/s)

Y Mass fraction

δ Thermal physical dimension (m)

ε_s Surface emissivity

θ Inclination angle minus 90 degrees

λ Thermal conductivity (kW/^{o}Km)

ρ Density (g/m^3)

σ Stefan-Boltzmann constant (kW/^{o}K^{4}m^2)

ϕ Ratio of oxygen mass over fuel mass

Subscripts

a   Ambient environment

ad   Adiabatic condition

c   Convective

e   Preheat condition

eq   Equilibrium condition

f   Flame

fR   Fuel resevoir

ig   Ignition

o   Top thin layer

ox   Oxygen

re   External radiant condition

ref   Referenced condition

st   Less lean or stoichiometric condition

Acknowledgements

Attachment 1
Derivation of the Flammability Curve

Establishing limits for flame spreading becomes simple once the equations of the flame spread model are rearranged and a condition is applied. As a first step, Eqs. (10) through (14) are combined and rearranged to solve for the flame temperature as a function of the flame thermal length with the result,

$$T_f = T_{ig} - \frac{B}{2} + \sqrt{\frac{B^2}{4} - C} \tag{27}$$

where,

$$B = R/\delta_f - Q\,\delta_f - T \tag{28}$$

$$C = Q\,S\,\delta_f - Q\,R \tag{29}$$

$$Q = \frac{\varepsilon_s \sigma\,(T_{ig}^4 - T_a^4) - \dot{q}_{re}}{\sqrt{2}\,\lambda_a} \tag{30}$$

$$R = \left(C_o + \frac{C_1}{T_{f_{ad}} - T_{ig}}\right)\sqrt{\frac{4\,\lambda_a}{Y_{ox_a}C_{p_a}\rho_a^2}} \tag{31}$$

$$S = \frac{T_a - T_{ig} + \dfrac{Y_{ox_a}\,\Delta H_c}{\phi\,C_{pa}}}{1 + \dfrac{Y_{ox_a}}{\phi\,Y_{fR}}} \tag{32}$$

$$T = T_{f_{ad}} - T_{ig} \qquad\qquad (33)$$

For constant environmental conditions, Eqs. (30) through (33) result in constant parameters for use in Eqs. (28) and (29). Thus, the opposed flow velocity can be arbitrarily chosen to determine the flame thermal length from Eq. (11). This length value is substituted into Eqs. (28) and (29), which are subsequently used to determine the flame temperature from Eq. (27). The values for the flame temperature and flame thermal length can then be substituted into Eqs. (7), (9), and (10) to obtain values of the parameters in Eq. (1) to solve for the flame spread rate. The plot of the flame spread rate as a function of opposed-flow speed (or of the flame thermal length) is shaped like a hill with steep sides. Setting $V_f = 0$, in an attempt to define the flammability limits, actually results in a nil solution. Instead, there exists an instability point at a low flame spread rate where the derivative of the flame spread rate with respect to the flame thermal length is infinite at both limits. Since the derivative of Eq. (1) also involves taking the derivative of Eq. (27) with respect to the flame thermal length, we find that the infinite derivative value occurs at the condition,

$$B^2/4 - C = 0 \qquad\qquad (34)$$

An examination of Eqs. (28) and (29) shows that the left side term of Eq. (34) is a fourth degree polynomial of δ_f. The inner two roots of Eq. (34) define the lower and upper extinction branches of the flammability curve shown in Figure 7. It is emphasized that the flammability curve is not unique, because the environmental conditions represented in Eqs. (30) through (33) can vary significantly.

Appendix C

Scaling of Cone Calorimeter Data

Figures 3-6 from "Technical Reference and User's Guide for FAST/FFM (Version 3)" were redrawn using the PC based program for scaling the heat and mass release rate data from the cone calorimeter. These reproduced images are shown in the following pages as Figures C.1-C.8.
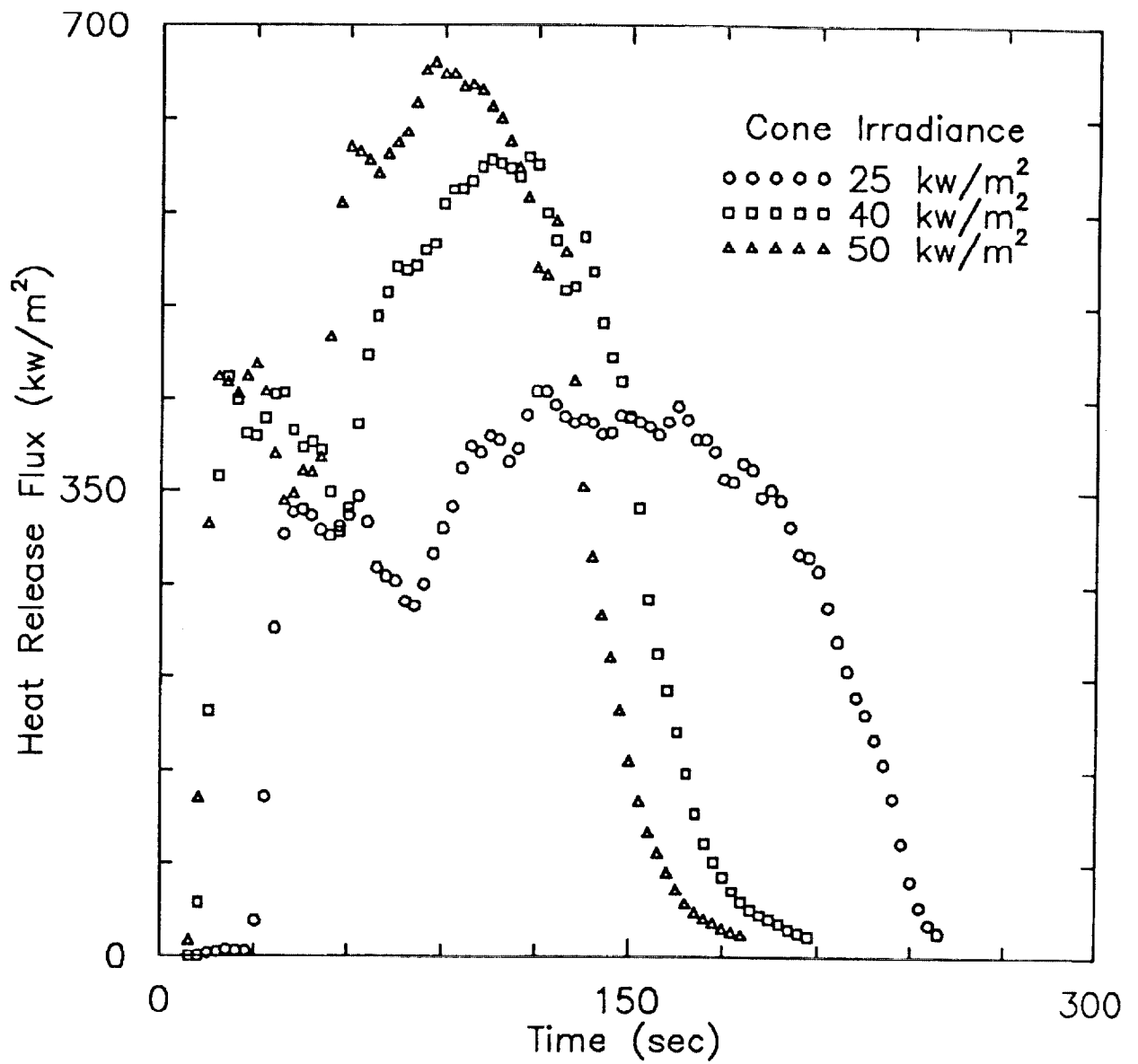
Figure C.1. Original Data of Heat Release Flux Versus Time for LO Fabric/FR PU Foam Material.
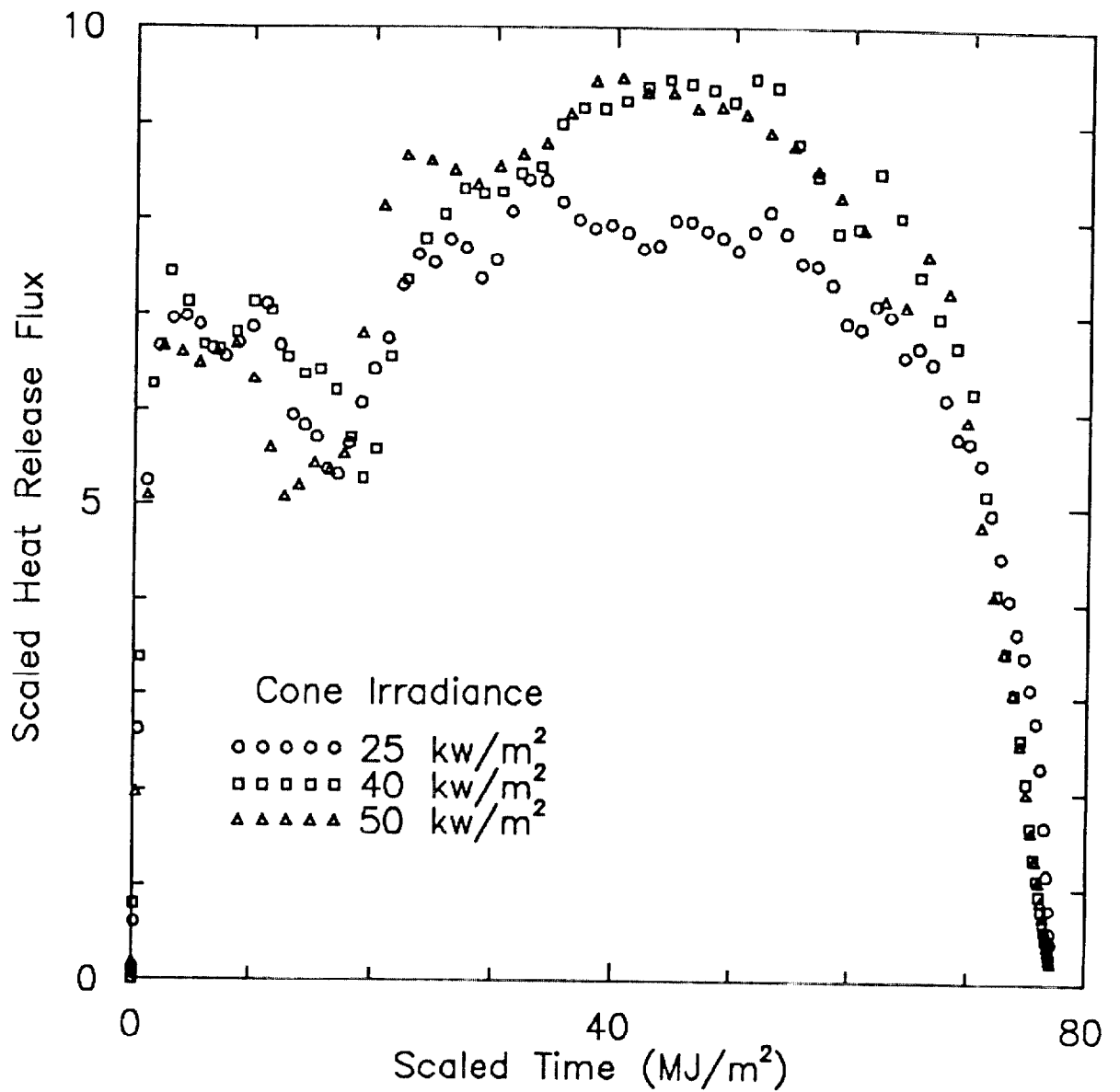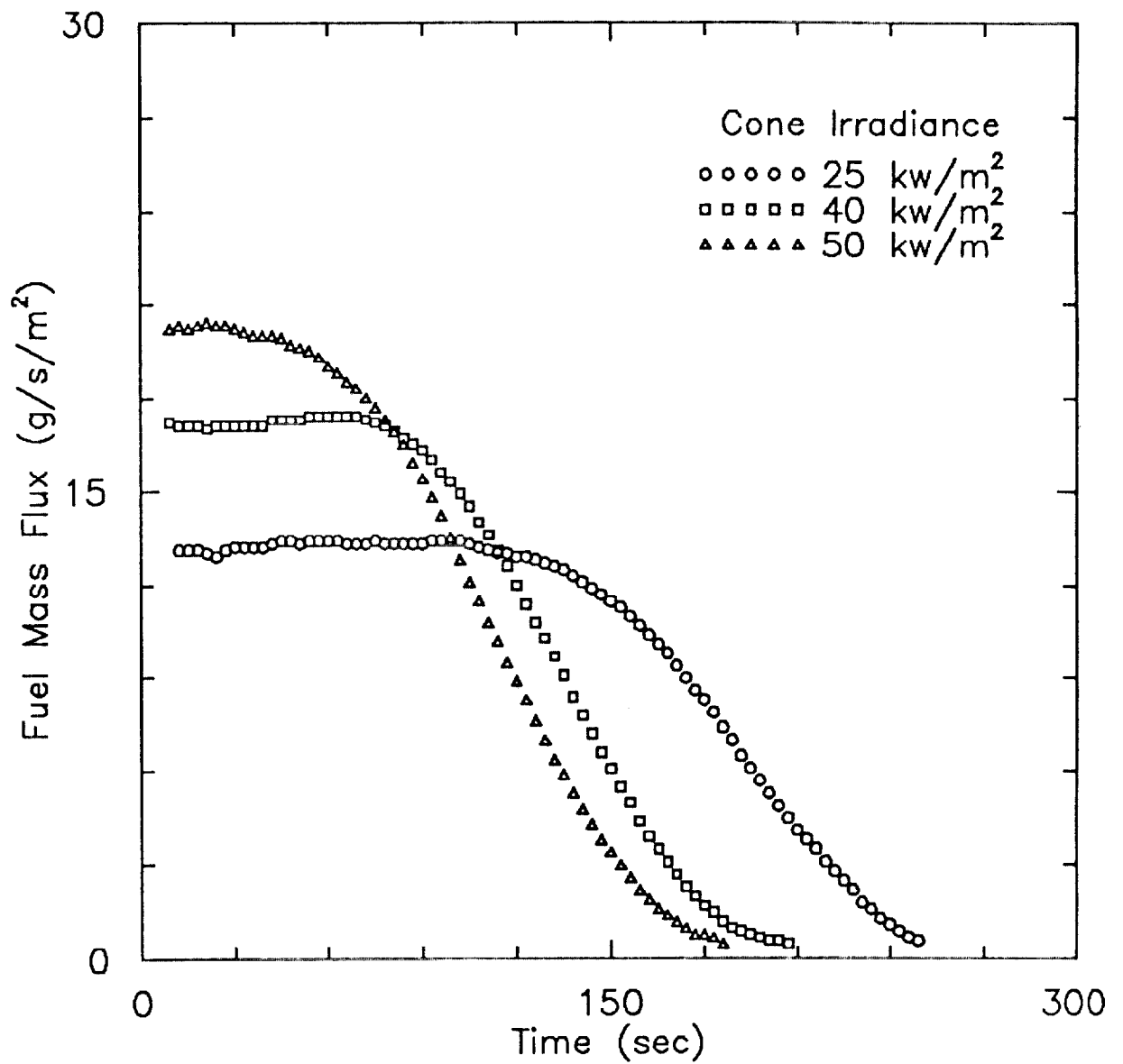
Figure C.2.   Correspond Scaled Heat Release Flux Versus Scaled Time for
LO Fabric/FR PU Foam Material.

Figure C.3.   Original Data of Fuel Release Flux Versus Time for LO Fabric/FR PU
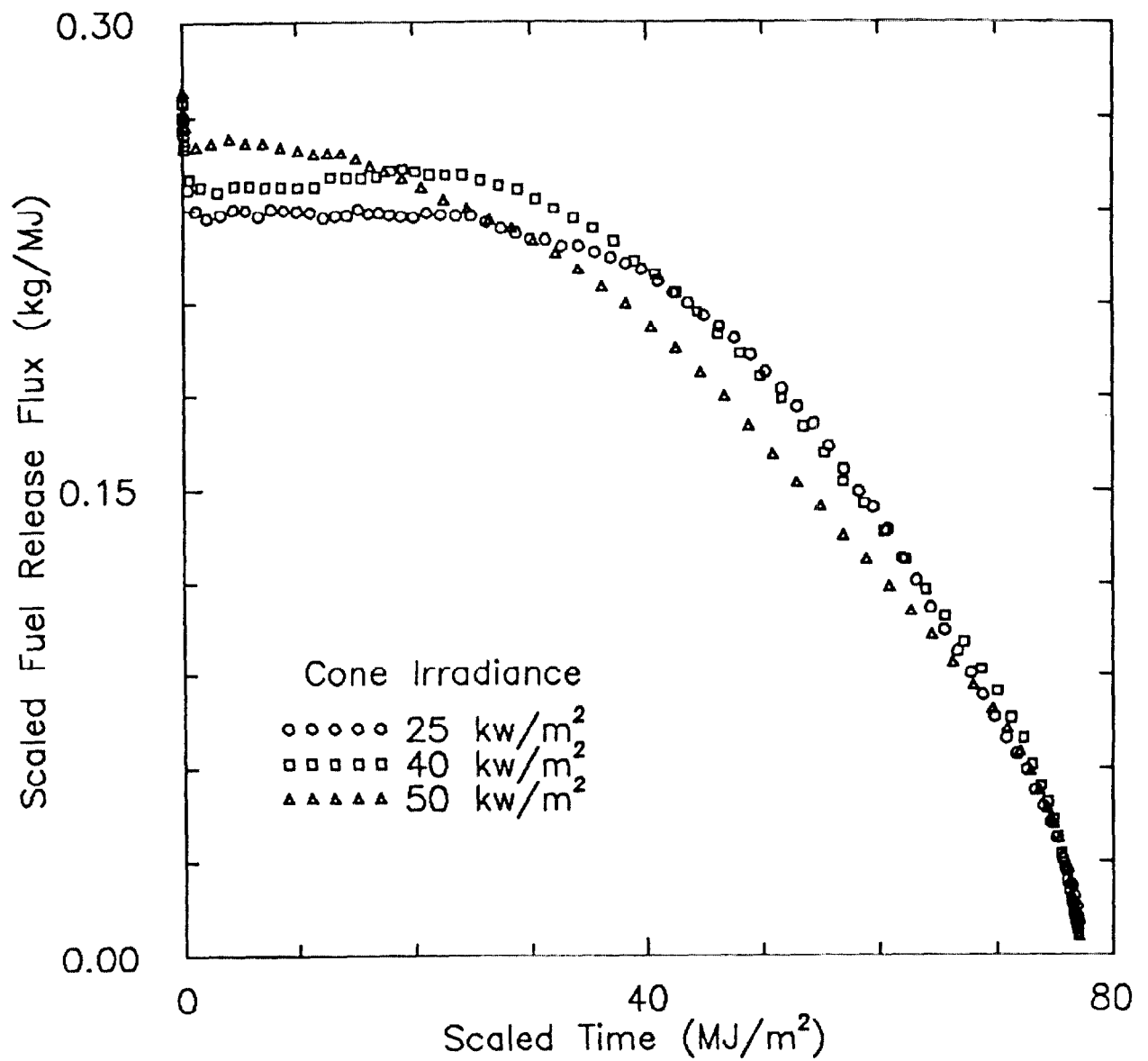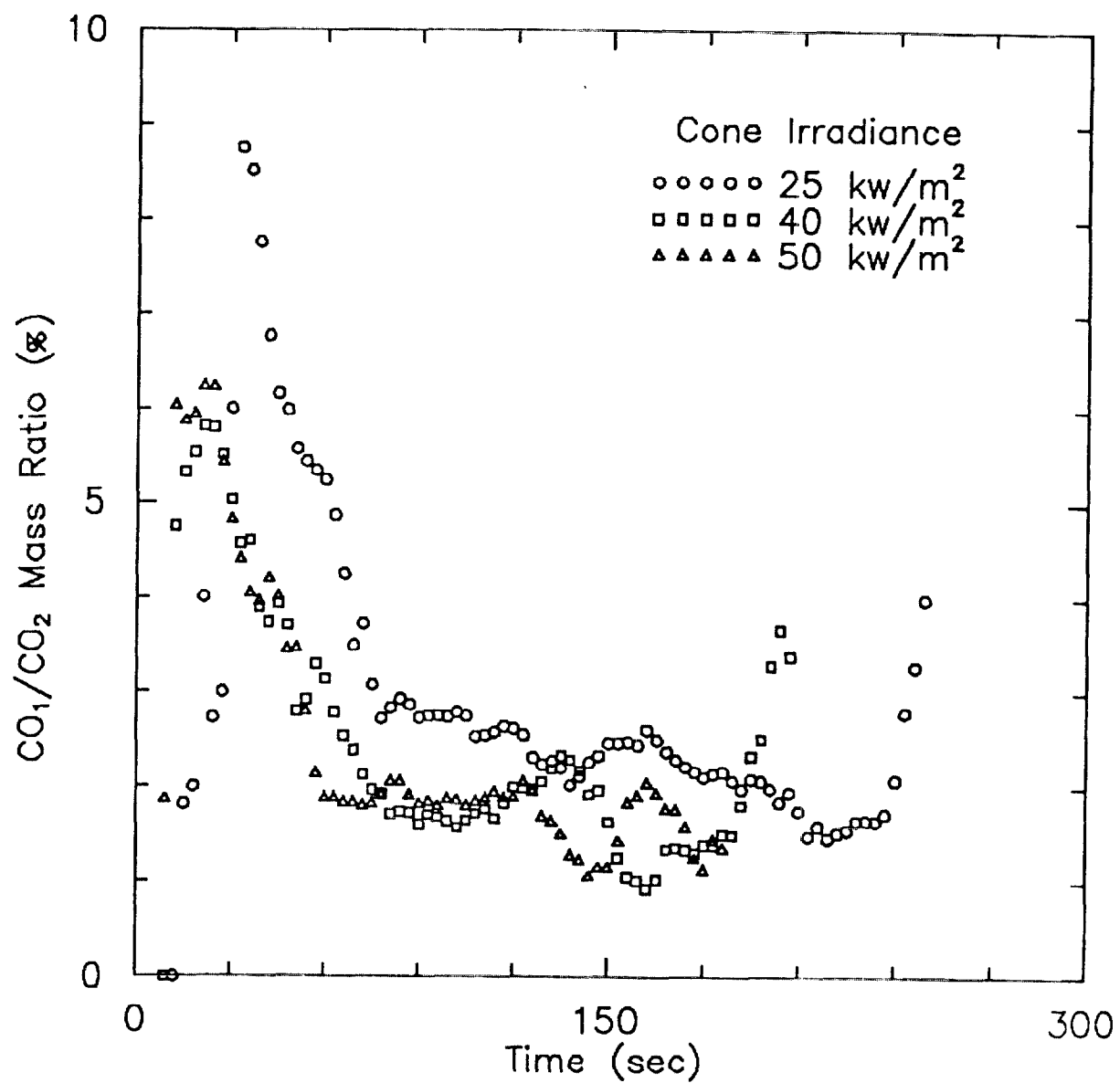Foam Material.

Figure C.4.   Correspond Scaled Fuel Release Flux Versus Scaled Time for LO
Fabric/FR PU Foam Material.

Figure C.5.   Original Data of Co to Co_2 Mass Ratio Versus Time for LO Fabric/FR PU Foam Material.
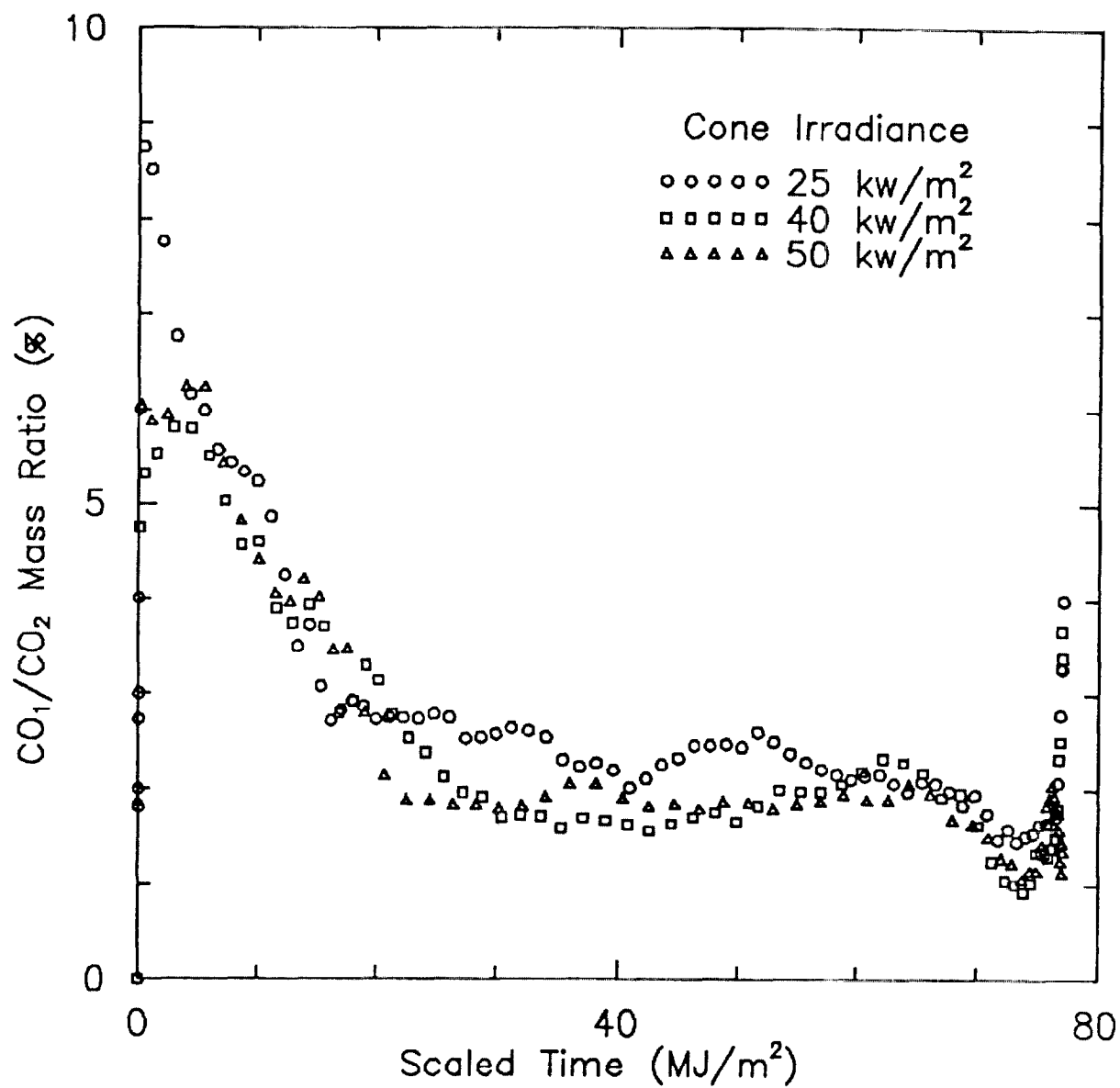
Figure C.6.   Processed Data of CO to CO_2 Mass Ratio Versus Scaled Time for LO Fabric/FR PU Foam Material.
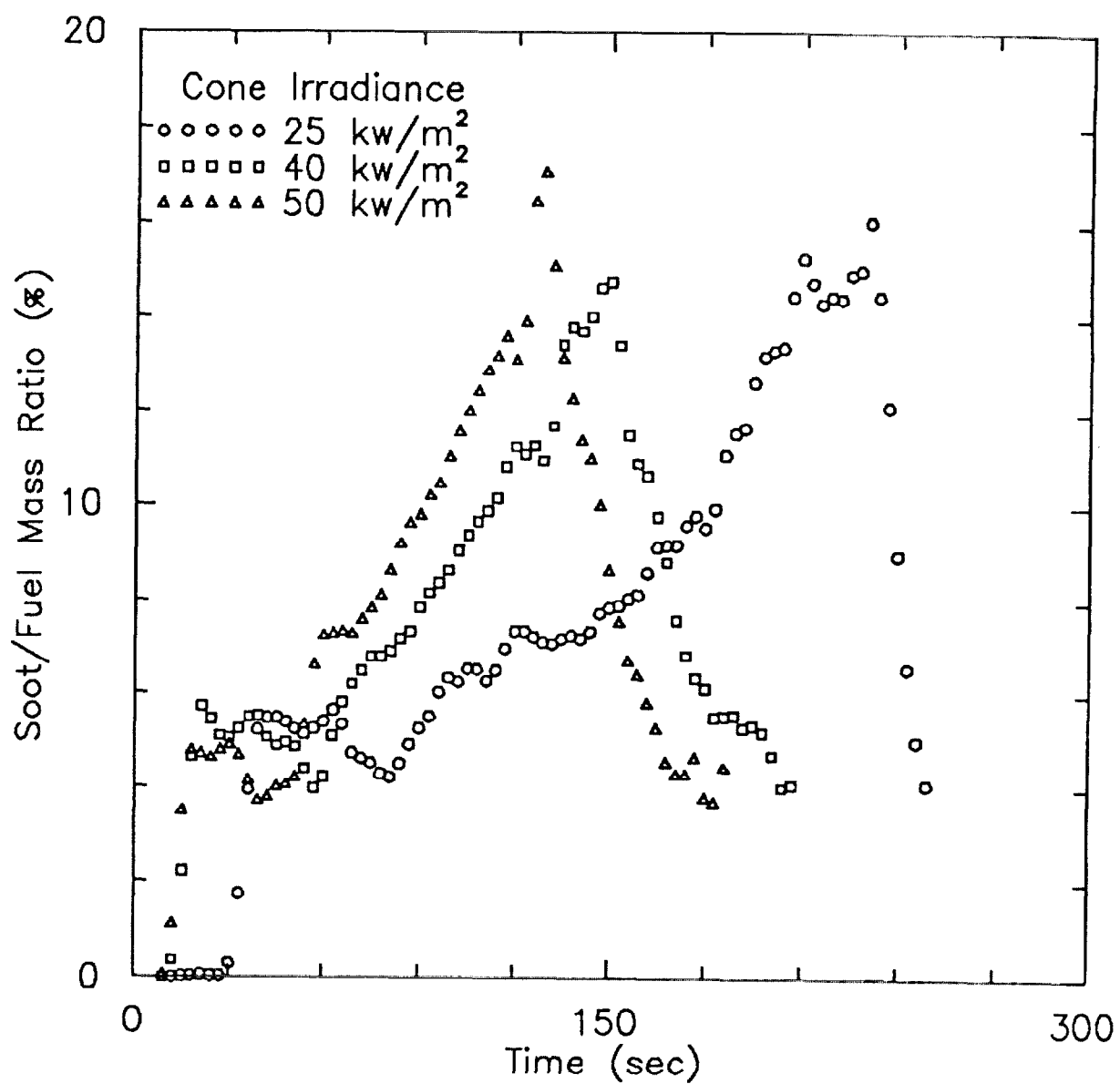
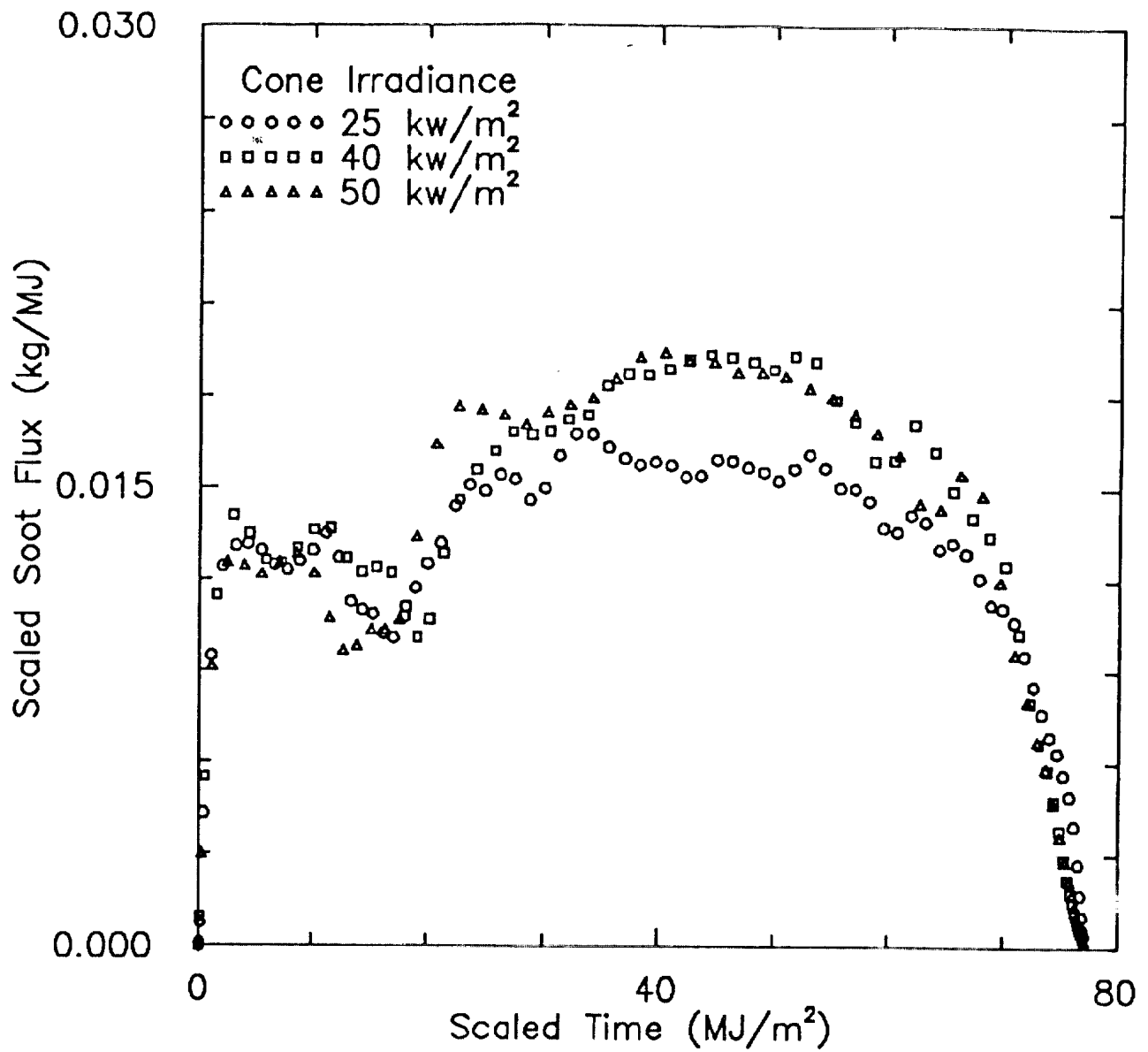Figure C.7.   Calculated Soot to Fuel Mass Ratio Versus Time for LO Fabric/FR PU Foam Material.

Figure C.8.   Calculated Scaled Soot Mass Flux Versus Scaled Time for LO Fabric/FR PU Foam Material.

NIST-114A	U.S. DEPARTMENT OF COMMERCE	1. PUBLICATION OR REPORT NUMBER
(REV. 3-90)	NATIONAL INSTITUTE OF STANDARDS AND TECHNOLOGY	NIST-GCR-92-601
		2. PERFORMING ORGANIZATION REPORT NUMBER
	BIBLIOGRAPHIC DATA SHEET	3. PUBLICATION DATE
		January 1992

4. TITLE AND SUBTITLE

Modifications to Furniture Fire Model for Hazard System

5. AUTHOR(S)

Mark A. Dietenberger

6. PERFORMING ORGANIZATION (IF JOINT OR OTHER THAN NIST, SEE INSTRUCTIONS)	7. CONTRACT/GRANT NUMBER
University of Dayton	NIST Grant No. 60NANBOD1051
Research Institute	8. TYPE OF REPORT AND PERIOD COVERED
Dayton, OH 45469	Final Report October 1991

9. SPONSORING ORGANIZATION NAME AND COMPLETE ADDRESS (STREET, CITY, STATE, ZIP)

U.S. Department of Commerce
National Institute of Standards
   and Technology
Gaithersburg, MD 20899

10. SUPPLEMENTARY NOTES

11. ABSTRACT (A 200-WORD OR LESS FACTUAL SUMMARY OF MOST SIGNIFICANT INFORMATION. IF DOCUMENT INCLUDES A SIGNIFICANT BIBLIOGRAPHY OR LITERATURE SURVEY, MENTION IT HERE.)

This final technical report describes the work accomplished during the period from 31 July 1990 through 31 July 1991 by the University of Dayton Research Institute under grant # 60NANBOD1051 for the National Institute of Standards and Technology.

Modifications to the furniture fire model for inclusion in the HAZARD system required three major tasks: (1) comparison of the FAST/FFM predictions with several full-scale burns measured in the furniture calorimeter, (2) development of an algorithm for personal computers to calibrate ignition and flame spread parameters, and (3) conversion of FF to a Flame Spread Model (FSM) for a single panel. The code was implemented on the PC for use with CFAST. The application problems are compartmentation, structural fire resistance, ignitibility of a secondary combustible item and room flashover studies.

12. KEY WORDS (6 TO 12 ENTRIES; ALPHABETICAL ORDER; CAPITALIZE ONLY PROPER NAMES; AND SEPARATE KEY WORDS BY SEMICOLONS)

algorithms; cushions; fire models; fire retardant materials; fire spread; foam (materials); ignition; upholstered furniture

13. AVAILABILITY	14. NUMBER OF PRINTED PAGES
X UNLIMITED	126
FOR OFFICIAL DISTRIBUTION. DO NOT RELEASE TO NATIONAL TECHNICAL INFORMATION SERVICE (NTIS).	
ORDER FROM SUPERINTENDENT OF DOCUMENTS, U.S. GOVERNMENT PRINTING OFFICE, WASHINGTON, DC 20402.	15. PRICE
X ORDER FROM NATIONAL TECHNICAL INFORMATION SERVICE (NTIS), SPRINGFIELD, VA 22161.	A07

ELECTRONIC FORM